Millimeter-Wave Quasi-Optical Planar Circuits and Power Combining

Final Report

by

Kai Chang

January 15, 1996

U. S. Army Research Office

Contract No. DAAL03-92-G-0326

Department of Electrical Engineering

Texas A & M University

College Station, Texas 77843-3128

APPROVED FOR PUBLIC RELEASE;

DISTRIBUTION UNLIMITED

Millimeter-Wave Quasi-Optical Planar Circuits and Power Combining

Final Report

by

Kai Chang

January 15, 1996

U. S. Army Research Office

Contract No. DAAL03-92-G-0326

Department of Electrical Engineering

Texas A & M University

College Station, Texas 77843-3128

SF 298 MASTER COPY KEEP THIS COPY FOR REPRODUCTION PURPOSES

REPORT DOCUMENTATION PAGE

Form Approved
OMB NO. 0704-0188

1. AGENCY USE ONLY *(Leave blank)*	2. REPORT DATE	3. REPORT TYPE AND DATES COVERED
	January 15, 1996	Final 1 Aug 92 - 30 Nov 95

4. TITLE AND SUBTITLE

Millimeter-Wave Quasi-Optical Planar Circuits and Power Combining

5. FUNDING NUMBERS

DAAL03-92-G-0326

6. AUTHOR(S)

Kai Chang

7. PERFORMING ORGANIZATION NAMES(S) AND ADDRESS(ES)

Department of Electrical Engineering
Texas A&M University
College Station, Texas 77843-3128

8. PERFORMING ORGANIZATION REPORT NUMBER

9. SPONSORING / MONITORING AGENCY NAME(S) AND ADDRESS(ES)

U.S. Army Research Office
P.O. Box 12211
Research Triangle Park, NC 27709-2211

10. SPONSORING / MONITORING AGENCY REPORT NUMBER

ARO 29325.29-EL

11. SUPPLEMENTARY NOTES

The views, opinions and/or findings contained in this report are those of the author(s) and should not be construed as an official Department of the Army position, policy or decision, unless so designated by other documentation.

12a. DISTRIBUTION / AVAILABILITY STATEMENT

Approved for public release; distribution unlimited.

12 b. DISTRIBUTION CODE

13. ABSTRACT *(Maximum 200 words)*

This report summarizes the research activities carried out in the Electromagnetics and Microwave Laboratory, Department of Electrical Engineering, Texas A&M University. The project was sponsored by the U.S. Army Research Office under contract No. DAAL03-92-G-0326. The topics of investigation included integrated and active antenna elements, spatial power combining and beam steering, quasi-optical components, novel uniplanar slotline and coplanar waveguide circuits, and other circuit developments and analyses. This final report for the period from August 1, 1992 through November 30, 1995 lists all the publications, which describe the supported research, along with the names of students who received the M.S. and Ph.D. degrees and contributed to the research.

14. SUBJECT TERMS	15. NUMBER IF PAGES
Quasi-Optical Techniques, Microwaves, Millimeter-Waves, Power Combining, Active Antennas, Uniplanar Circuits, Beam Steering	81
	16. PRICE CODE

17. SECURITY CLASSIFICATION OR REPORT	18. SECURITY CLASSIFICATION OF THIS PAGE	19. SECURITY CLASSIFICATION OF ABSTRACT	20. LIMITATION OF ABSTRACT
UNCLASSIFIED	UNCLASSIFIED	UNCLASSIFIED	UL

FOREWORD

This report summarizes the research activities carried out in the Electromagnetics and Microwave Laboratory, Department of Electrical Engineering, Texas A & M University. The project was sponsored by the U.S. Army Research Office under contract No. DAAL03-92-G-0326. The period of performance was from August 1,1992 through November 30, 1995. The topics of investigation included integrated and active antenna elements, spatial power combining and beam steering, quasi-optical components, novel uniplanar slotline and coplanar waveguide circuits, and other circuit developments and analyses. The research has resulted in the publication of 2 books, 1 book chapter and 49 papers.

Table of Contents

1. Introduction and Problems Studied

For the past decade, microwave/millimeter-wave activities have been accelerating for both civil and military applications including wireless communications, radar, sensors, seekers, navigation, remote sensing, electronic warfare and space technology. These applications have created the urgent need for low cost, high performance solid-state integrated systems using planar integrated circuit technology. These integrated systems normally consist of high power transmitters, low noise receivers, antennas, and control devices. To lower the losses and cost, quasi-optical technique is attractive for millimeter-wave frequencies. In many applications, frequency agility is required, and electronic tunability of the system is desirable. The output power from a single active solid-state device is limited by fundamental thermal and impedance problems. To meet the high power requirements for many applications, it is necessary to combine many devices to achieve high power output.

Combining power from many active devices is a difficult task at millimeter-wave frequencies due to the moding and size problems [1]. The maximum number of devices that can be combined in a conventional resonant or hybrid-coupled power combiner decreases as the operating frequency is increased. To overcome these problems, spatial and quasi-optical power combining techniques have been proposed to combine power in free space at high frequencies [2]. In these combiners, the active device is integrated with a radiating element to form an active element. Many of these active elements are then combined in free space or in an open resonator. For efficient power combining, all source elements must be coherent in phase and frequency. Injection-locking through open resonator, space, or mutual coupling can be used to achieve the coherency. Many novel active antenna elements and spatial power combiners have been demonstrated in this project.

Conventional phased-arrays incorporate oscillators, amplifiers, phase shifters, beam-forming distribution networks and antennas to transmit an electronically steerable beam. The system is complex, expensive, lossy and bulky. The phase shifters and distribution networks are difficult to fabricate at millimeter-wave frequencies with good performance. Consequently, the use of phased arrays is limited to a few sophisticated, expensive military

and space systems. To overcome these problems, a low cost approach for steering an antenna beam was demonstrated by controlling the bias to each antenna element.

In addition to application in active antenna elements and power combiners, quasi-optical techniques can be used for filters, amplifiers, receivers, detectors or imaging arrays, power conversion arrays, etc. The techniques are especially attractive for millimeter-wave frequencies due to the advantages of low cost, large size and good performance. Several quasi-optical components were developed with excellence performance under this project.

Along with the research of the quasi-optical components and spatial power combining techniques, work was also carried out on the novel planar slotline and coplanar waveguide circuit developments. The slotline and coplanar waveguide have the center conductor and ground planes on the same side of the substrate. They are truly uniplanar microwave integrated circuits that have the advantage of easy implementation of solid-state devices.

Although most of our experimental work was concentrated at microwave frequencies, the circuits and analyses developed can be applied to millimeter-waves. The problems studied and major accomplishments made are summarized below:

1. A novel dual-FET active patch antenna element was developed with an advantage of low cross-polarization. The elements were used to demonstrate a 2 × 2 array power combiner with an equivalent isotropic radiated power of 2.99 W at X-band.
2. An FET oscillator integrated with a notch antenna has been demonstrated. The active antennas were used to create both E-plane and H-plane linear arrays as well as a 2-D array. A 3 × 3 quasi-optical combiner was also developed.
3. A linear tapered slot antenna integrated directly with an FET amplifier was demonstrated. Compared with a passive antenna, the active antenna has an extra gain of 7 dB at 9.2 GHz. Similar results have also been achieved for an integrated active slot dipole antenna amplifier.
4. A new active slotline ring antenna using an FET was invented. A simple transmission line method was used to predict the resonant frequency.
5. Active inverted stripline circular patch antennas integrated with Gunn devices and FETs were developed for spatial power combining. A 2 × 2 array was demonstrated with over 89% combining efficiency. Beam steering of 40 degrees

was obtained by varying bias voltage to the individual antenna elements of the array.

6. An analysis was developed for a weak coupling two-dimensional active antenna array. A novel circular patch active antenna element was developed and used for building two-dimensional arrays. The active antennas and arrays have low cross-polarization.
7. Inverted stripline antennas were integrated with various solid-state devices such as Gunn, FET, PIN, and varactor devices for oscillating, amplification, switching, tuning and modulation functions. These integrated antennas provide a low-cost approach for commercial applications.
8. An FET transistor and a Schottky barrier diode have been integrated within an inverted stripline patch antenna for transceiver applications. A 5.5 dB isotropic mixer conversion loss was achieved at 6 GHz. A two-way communication link was demonstrated.
9. A new type of active antenna appropriate for coupled Gunn oscillator driven spatial power combining arrays was developed. The active antenna uses a ring stabilized oscillator coupled to a slot antenna.
10. The modes and their stability of a symmetric two-element spatial combining array were addressed theoretically. It was shown that two stable operation modes, one is in-phase and the other is 180 degrees out-of-phase. Experiments verified the theory.
11 Quasi-optical frequency selective surfaces for spatial filtering applications were used to reduce the second harmonic radiation of rectenna elements. The devices are important in the application of microwave power transmission.
12. Slot-fed higher order mode Fabry-Perot filters were demonstrated for both X-and Ka-bands. The filters have unloaded Q values which range from 1000 to 7000 with insertion losses of less than 1 dB.
13. A quasi-optical dual polarized circular patch rectifying antenna was developed using a circular patch antenna integrated with a detector diode. The rectenna has over 48% conversion efficiency at 2.45 GHz.

14 A new uniplanar hybrid ring coupler was developed for broadband operation. The circuit exhibits a bandwidth of one octave from 2 to 4 GHz with ± 0.25 dB power dividing balance and ± 1 degree phase balance.

15. A broadband uniplanar branch-line coupler using a coupled rectangular slotline ring was developed. Experimental results show that the new coupler has over 20 dB isolation over a bandwidth of more than 40% centered at 3 GHz with ± 1 dB power dividing balance.

16. Eight new coplanar waveguide (CPW) to slotline transitions using uniform and nonuniform CPWs or slotlines were investigated. The best configuration is a pair of transitions using CPW shorts and slotline radial stubs with a 1 dB insertion loss bandwidth of more than 5.2 : 1. Measured results agree with calculation.

17. Novel slotline and CPW ring resonators were introduced and integrated with varactor diodes to create electronically tunable uniplanar ring resonators. Experimental results agree very well with the theory.

18. A new type of slotline dual-mode filter has been developed with a bandwidth of 12.3% and a stopband attenuation of more than 30 dB centered at 3.5 GHz.

19. Wideband transition from conductor-backed coplanar waveguide to modified coplanar stripline was devised using multiple substrate. The transition was used to feed a dipole antenna and a broadband spiral antenna.

20. A new reverse-phase CPW hybrid-ring coupler and a uniplanar CPW magic-T have been developed. Experimental results showed that the hybrid-ring coupler has a 60% bandwidth centered at 3 GHz and the magic-T has a bandwidth of one octave from 2 to 4 GHz with 0.4 dB amplitude imbalance and 3.5 degrees phase imbalance.

21. The Gunn domain effects in the output conductance of the high frequency small-signal GaAs MESFET has been modeled. A time-delay element was included in the model.

22. A simple divide-by de-embedding method was developed for transmission coefficient measurements of microwave devices with non-coaxial terminals. The error analysis shows good results.

23. A low loss, wide bandwidth interconnect between two microstrip lines was devised. The interconnect uses a narrow rectangular slot aperture in the common ground plane of two microwave lines.

2. Integrated and Active Antennas

In an integrated antenna, a solid-state device is directly integrated with the planar antenna. The antenna is called active antenna if the solid-state device is an active device (oscillator or amplifier). In some cases, more than one solid-state devices can be used to perform multiple functions. To accomplish high output power levels for many system requirements, many active antennas can be aligned to form a spatial or quasi-optical power combiner. Under this project, many novel integrated and active antenna configurations have been developed using inverted stripline patch, notch, slotline ring, microstrip ring, and coupled circular patch.

2.1. Antennas Integrated with Oscillators

Figure 1 shows various active antenna elements developed under this project. Figure 1 (a) and (b) show the integration of an inverted stripline circular patch antenna integrated with a Gunn devices [3] and an FET [4], respectively. The configuration avoids drilling through the substrate to insert the devices. The inverted substrate serves as a radome for protection and hermetic sealing. The active antenna and housing can be fabricated in modular form for reduced cost and easy replaceability of devices. The antenna exhibits a much cleaner spectrum and lower cross-polarization than any other active antennas.

The dual FET patch antenna shown in Figure 1(c) uses two FETs that symmetrically load a spit patch antenna [5]. The configuration of the devices decreases H-plane cross-polarization dramatically. The coupled circular patch antenna integrated with an FET is shown in Figure 1(d) [6]. The gaps between the source and drain and between the source and the gate form a feedback circuit to make the device unstable. The patches serve both as a resonator in the feedback loop for the FET oscillator and as a radiating element.

Figure 1(e) shows a layout of the FET active notch antenna [7] designed for 7 GHz operation. The feedback from the drain to gate is provided by the slotline labeled 1 in Figure 1(e). Changing the length and width of this line alters the amount of feedback and

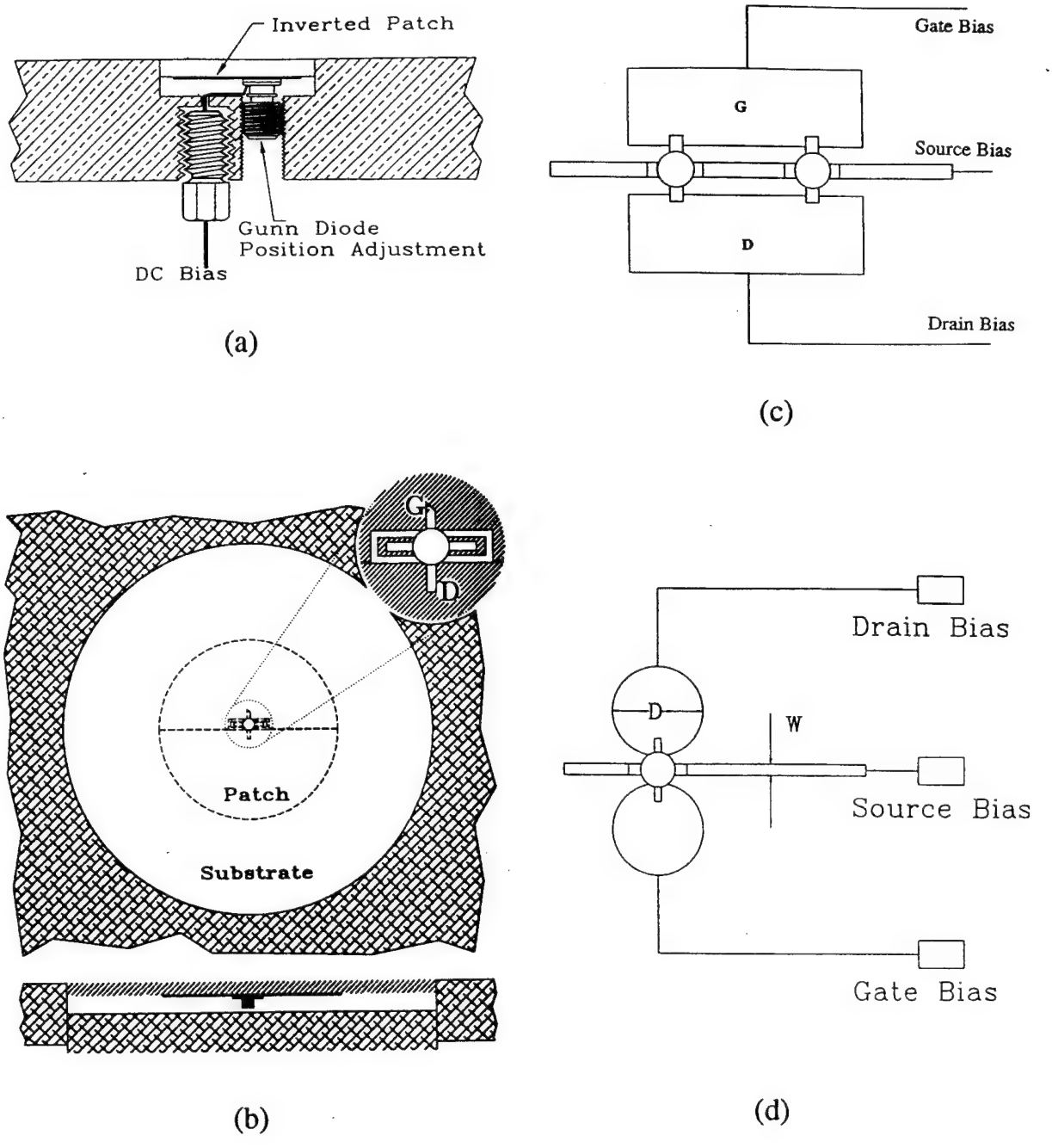

Figure 1. Various active antennas integrated with oscillators developed under this project: (a) inverted stripline patch antenna integrated with Gunn devices, (b) inverted stripline patch antennas integrated with FET, (c) dual-FET patch antenna, (d) coupled circular patch antenna with FET, (e) FET notch antenna, (f) slotline ring antenna with FET, and (g) FET microstrip ring coupled slot antenna.

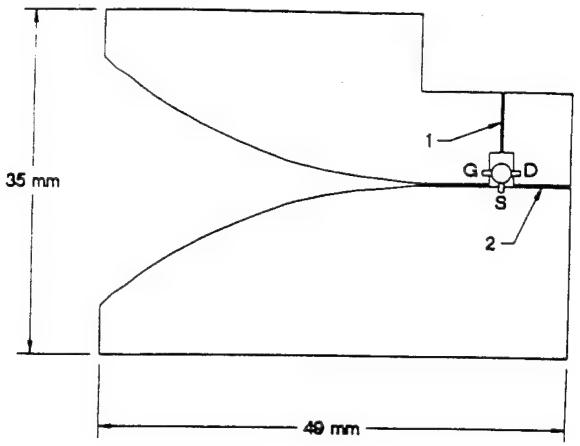

(e)

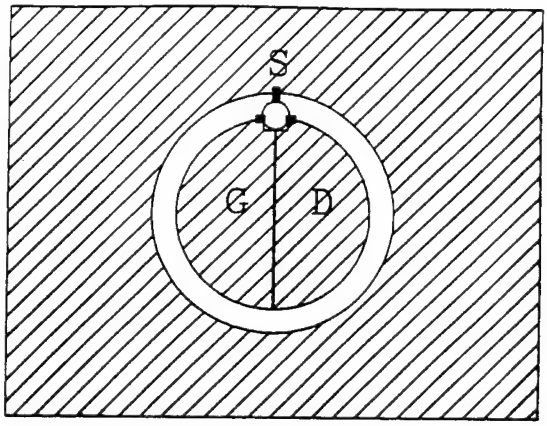

(f)

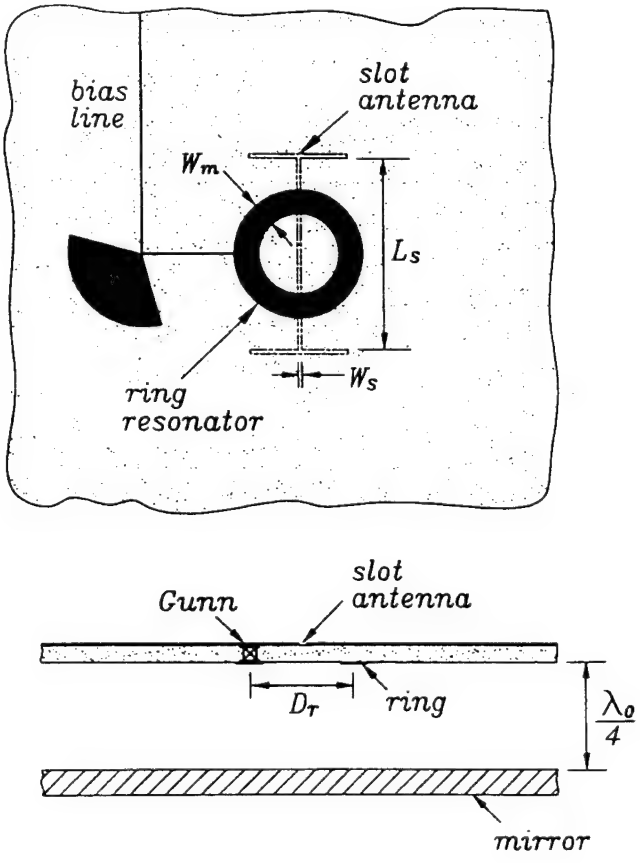

(g)

Figure 1. (continued)

can be used to control the oscillation frequency. The oscillation frequency was varied from 5 to 8 GHz using this technique. Circuit modeling was developed to accurately predict the oscillation frequency [8]. This active antenna has the advantage of broad bandwidth.

A slotline ring antenna integrated with an FET device is shown in Figure 1(f) [9]. A simple transmission line method was used to predict the resonant frequency of the active antenna with good agreement. Finally, Figure 1(g) shows a new active antenna using a ring-stabilized Gunn oscillator coupled to a slot antenna [10]. A circular microstrip ring is used as the resonant element, while a slot on the substrate ground plane is employed as the radiating element. The bias circuits and Gunn devices are hidden behind the metallization. This active antenna has advantages of low spurious radiation, low cross polarization, good heat sinking, and ease of integration.

2.2. Antennas Integrated with Amplifiers

An FET amplifier can be directly integrated with an antenna element. Figure 2 shows a linear tapered slot antenna integrated directly with an FET amplifier [11]. The antenna has high gain over a wide band with low cross-polarization. Compared with a passive antenna, the active antenna has an extra gain of 7 dB at 9.2 GHz. The inclusion of the FET amplifier did not significantly increase the cross-polarization.

An active slot dipole antenna amplifier was also demonstrated [12]. The circuit configuration is shown in Figure 3. It consists a CPW feed line with the FET amplifier integrated. The center strip conductor of the CPW extends across the slot line at a right angle. This arrangement provides an extra 7 dB antenna gain due to the amplifier.

2.3. Antennas Integrated with PIN and Varactor Diodes

Integrated antennas can reduce size, weight, and cost of many microwave systems by incorporating component functions directly at the antenna terminals. Antennas can be integrated with PIN and varactor diodes to provide switching, modulation, and tuning functions. Figure 4 shows the integration of PIN or varactor diodes with an inverted stripline circular patch antenna [13]. Since the electric field is a maximum at the radiating edges of the antenna, PIN and varactor diodes will have the most effect at these positions. Using PIN diodes, experiments show that an input VSWR can be switched from 1.01 to

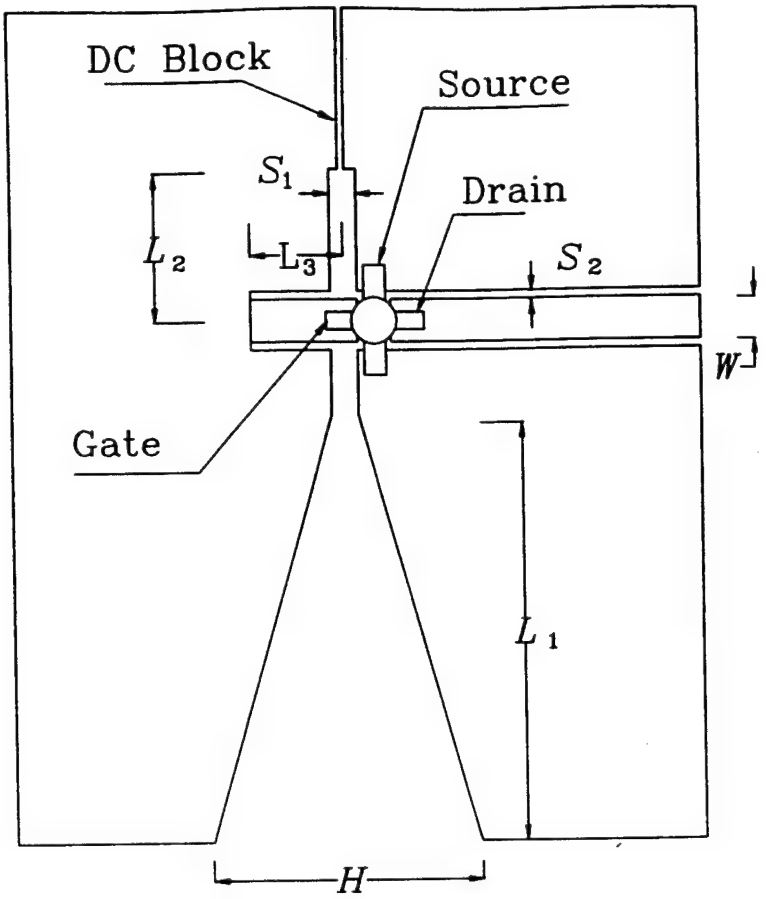

Figure 2. Circuit configuration of a CPW cross-fed linear tapered slot antenna amplifier.

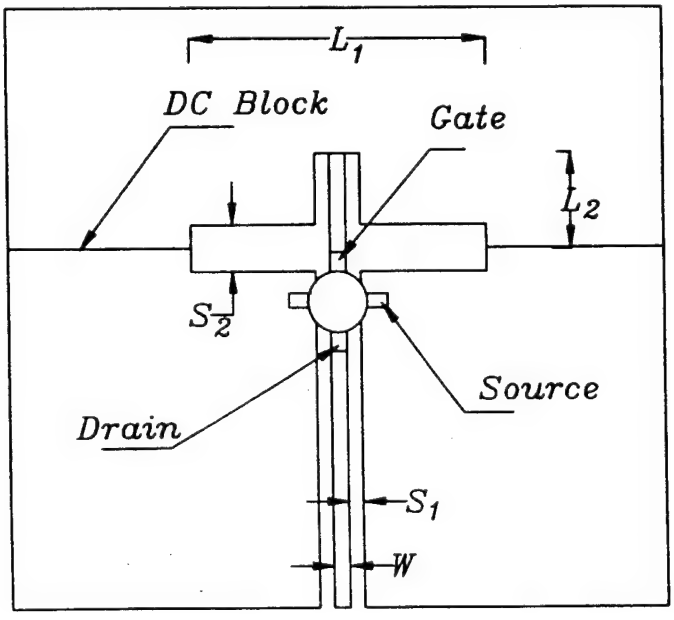

Figure 3. Circuit configuration of a CPW cross-fed slot dipole antenna amplifier.

22.87. Using varactor diodes, the antenna can be tuned over 31% bandwidth centered at 3.4 GHz with an input VSWR of less than 2. This circuit should have many applications in channelized receiver systems.

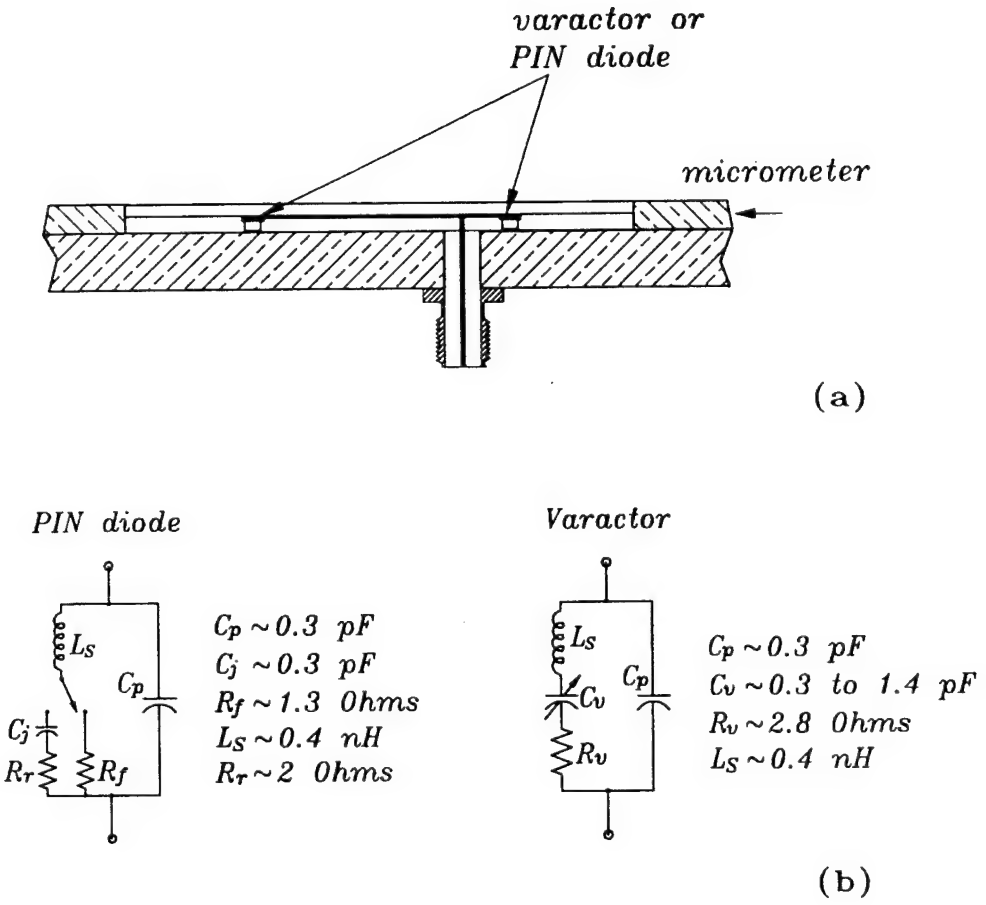

Figure 4. (a) Inverted stripline patch antennas integrated with PIN and varactor diodes, (b) equivalent circuit of PIN and varactor diodes.

2.4. Integrated Active Transceiver Antenna

For many system applications, a transceiver is needed to transmit and receive the signals using the same antenna. As shown in Figure 5, an FET transistor and a Schottky barrier mixer diode have been integrated within an inverted patch antenna for transceiver applications [14]. The FET oscillator acts as a transmitter and it also couples a portion of the power to the mixer as a local oscillator. The optimal position for placing the mixer diode on the patch is determined through analysis and experiments. The mixer diode

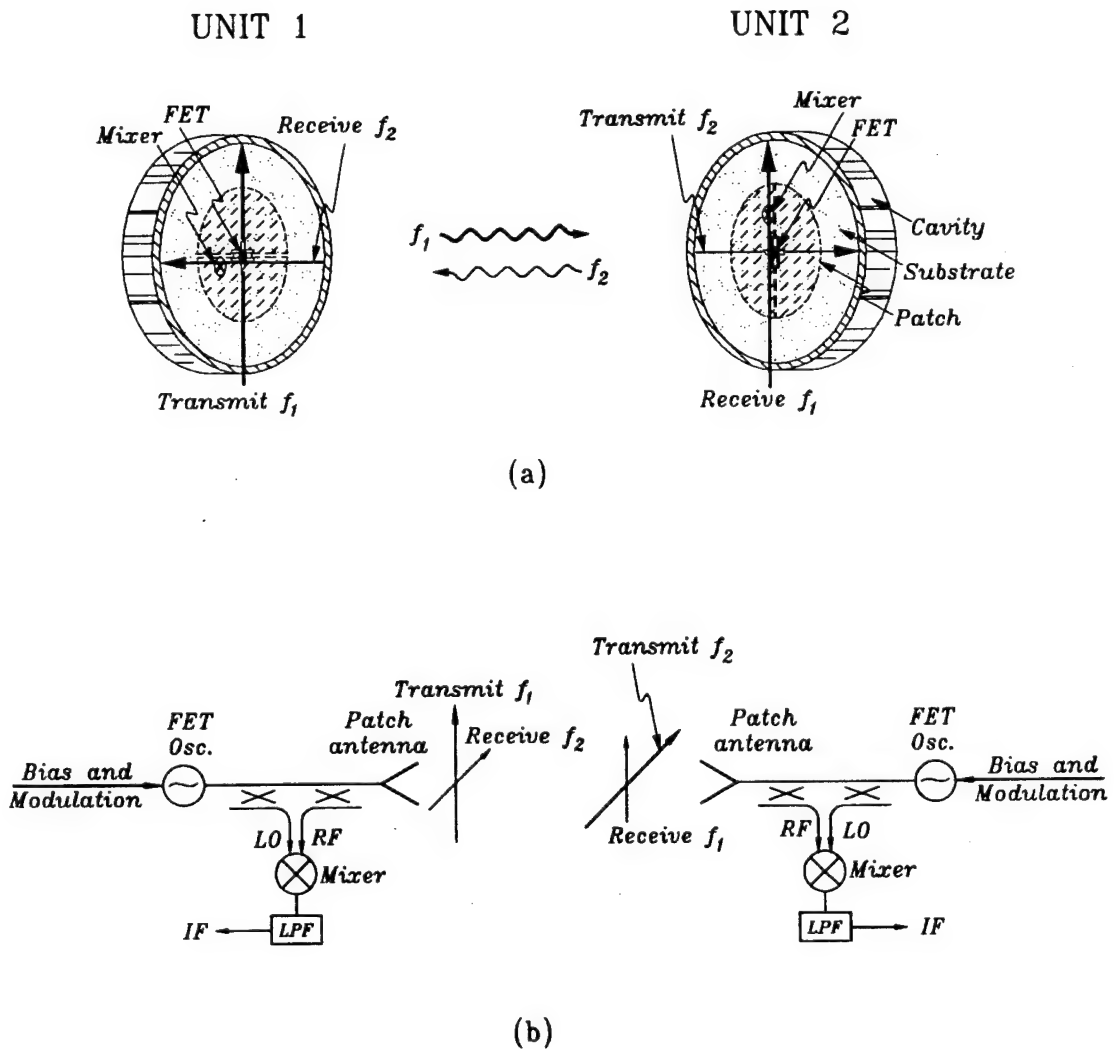

Figure 5. Active integrated antenna transceivers for two-way communication system (a) configuration, (b) block diagram.

receives a portion of the oscillator power that mixes with an incoming RF signal. Preliminary results exhibit a 5.5 dB isotropic conversion loss at 6 GHz for an IF frequency of 200 MHz with the FET serving as both the transmitter and the local oscillator at 5.8 GHz. Very good antenna patterns were obtained. This structure can be used for many applications such as wireless communications, sensors and radar systems. A two way communication system using these transceivers was demonstrated.

3. Spatial Power Combining and Beam Steering

The spatial power combiner utilizes the correct phase relationship of many radiating elements to combine power in free space. For efficient combining, all source elements must be coherent in phase and frequency. Progressive phase shift can be introduced by varying the bias voltages to the elements. This could be a very useful, low cost method of beam steering without the use of traditional phase shifters. Various spatial power combiners have been developed using dual FET patch, FET notch, FET coupled circular patch, and Gunn inverted stripline patch antennas. Beam steering of 40 degrees was demonstrated. Analyses were carried out to study the phase relation, modes, and mode stability of a weak coupling two-dimensional active antenna array and a symmetric two-element coupled oscillator array.

3.1. Analysis of a Weak Coupling Two-Dimensional Active Antenna Array

Making an active array to work requires injection locking. Injection locking synchronizes a free running oscillator to a weak injection signal at a frequency close to the operating frequency of the oscillator. An analysis based on Adler's equations that introducing a coupling coefficient for multiple devices were derived for a weak coupling two-dimensional active array [6]. It was found that for a weakly coupled coherent power combiner, the phase relation must be $n\pi$ for any spacing between the elements. An optimal element spacing can be obtained for any array to produce the lowest side lobes.

3.2. Analysis of Modes and Their Stability

Most analyses on active antenna arrays were based on overly simplified models which failed to yield a complete, consistent and persuasive explanation to the modes and their

stability. Under this project, a unified theory was derived by extending Kurokawa's theory on the stability of oscillator [15]. It was found that the two modes (one is in-phase, the other 180 degrees out-of-phase) are just two natural solutions of the circuit equations. In most cases, either the in-phase mode or the 180 degrees out-of-phase mode can be easily obtained by varying the inter-element spacing or bias voltages. Experiments were carried out to verify these findings.

3.3. Spatial Power Combiners

Various spatial power combiners have been demonstrated with good combining efficiencies using the active antenna elements described in Section 2.1. Figure 6(a) shows an eight-element array [6] using FET coupled circular patch antenna elements. Equivalent isotropic radiated power levels of 3.8 W was obtained at 9 GHz. Similar combiners were also demonstrated using 1×4 and 2×2 arrays.

Figure 6(b) shows a four-element power combiner consisting of four dual FET active patch elements [5]. An analysis was carried out to show that the phase difference between two neighboring elements should be equal to multiples of 180 degrees. The right phase relation was achieved by reversely connecting the FETs. An equivalent isotropic radiated power of 2.99 W was achieved at 8.94 GHz with combining efficiency of 85%. The radiation patterns are very good with cross-polarization below 20 dB in E and H planes.

Eight X-band active inverted stripline antennas were built and tested for the square and diamond array as shown in Figure 6(c). The square array exhibits a 89 percent combining efficiency and the diamond array 86 percent efficiency [3]. The arrays can be bias tuned over a 50 MHz bandwidth.

The new FET notch active antenna elements were used to create both E-plane and H-plane linear arrays as well as a 2-D array. Figure 6(d) shows the results of a four-element H-plane linear array [7]. The combining efficiency is over 93% for this array. A 2×2 array and 3×3 array were also built with good combining efficiencies [7, 8].

3.4. Beam Steering without Conventional Phase Shifters

Active antenna operating frequency depends on the circuit and applied bias voltage. Single-output DC power supplies are usually used to operate an entire array to reduce the

overall cost. However, a variable voltage can be used to change individual active antenna operating frequencies. The difference between self-oscillating frequencies of active antennas produces a phase-shift in the injection-locked power combiner. The phase-shift can be used to electronically steer the beam of the active antenna power combiner [3, 16]. The beam steering angle is directly proportional to the difference in self-oscillating frequencies which depends on the applied DC bias voltage.

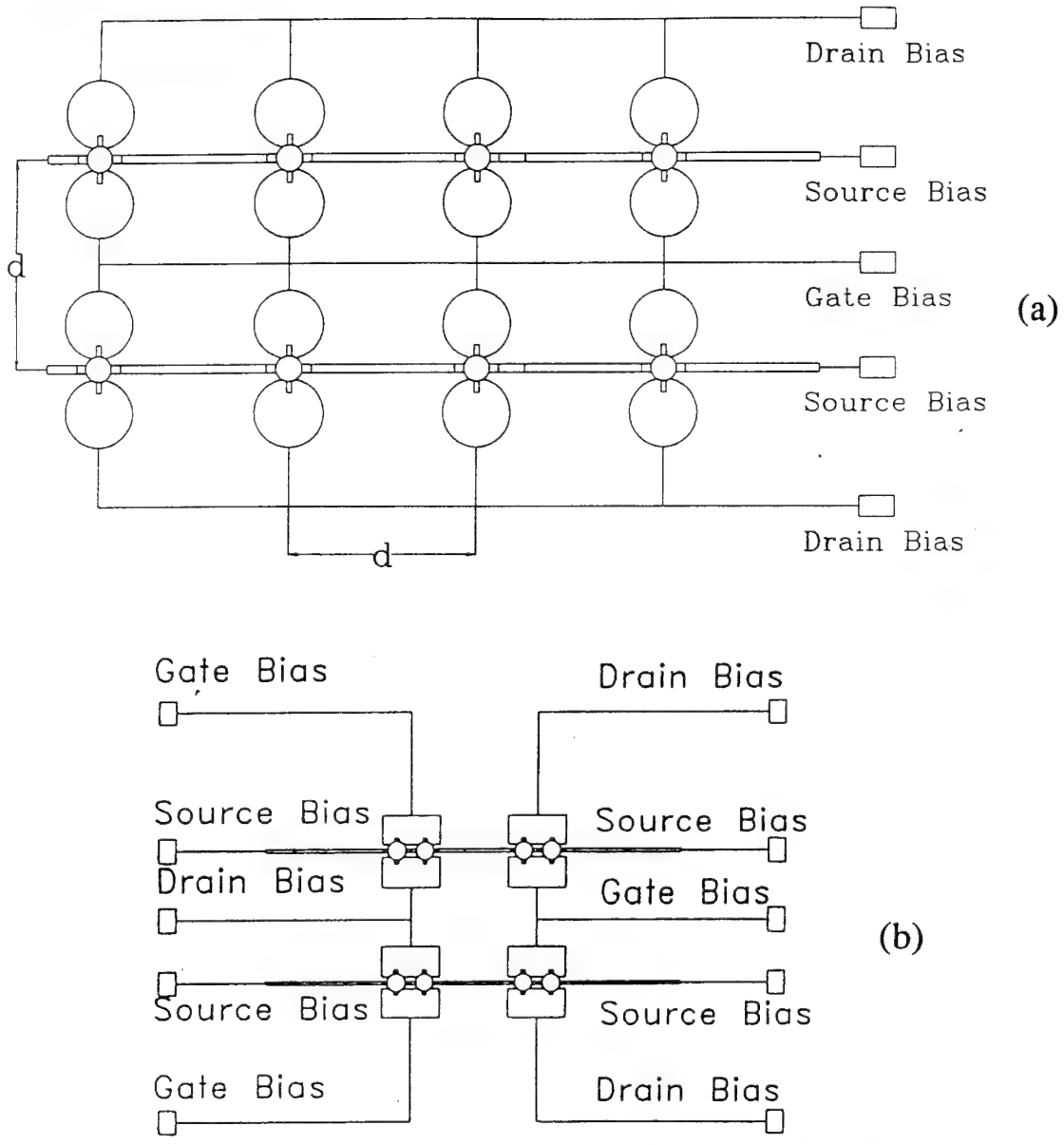

Figure 6. Various spatial power combiners developed under this project: (a) FET coupled circular patch power combiner, (b) dual FET patch power combiner.

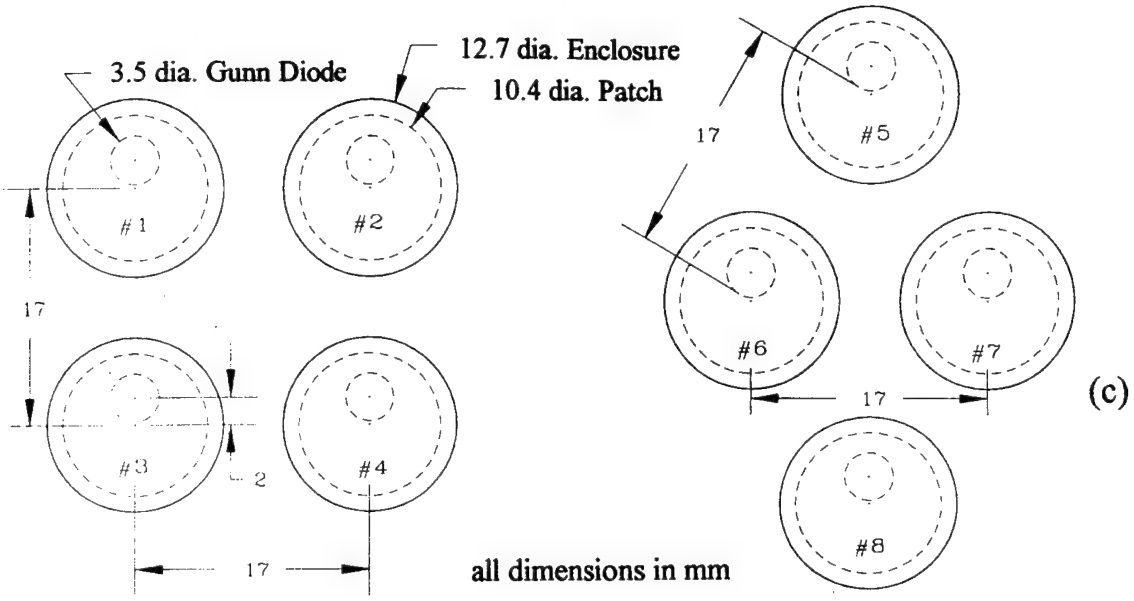

(c)

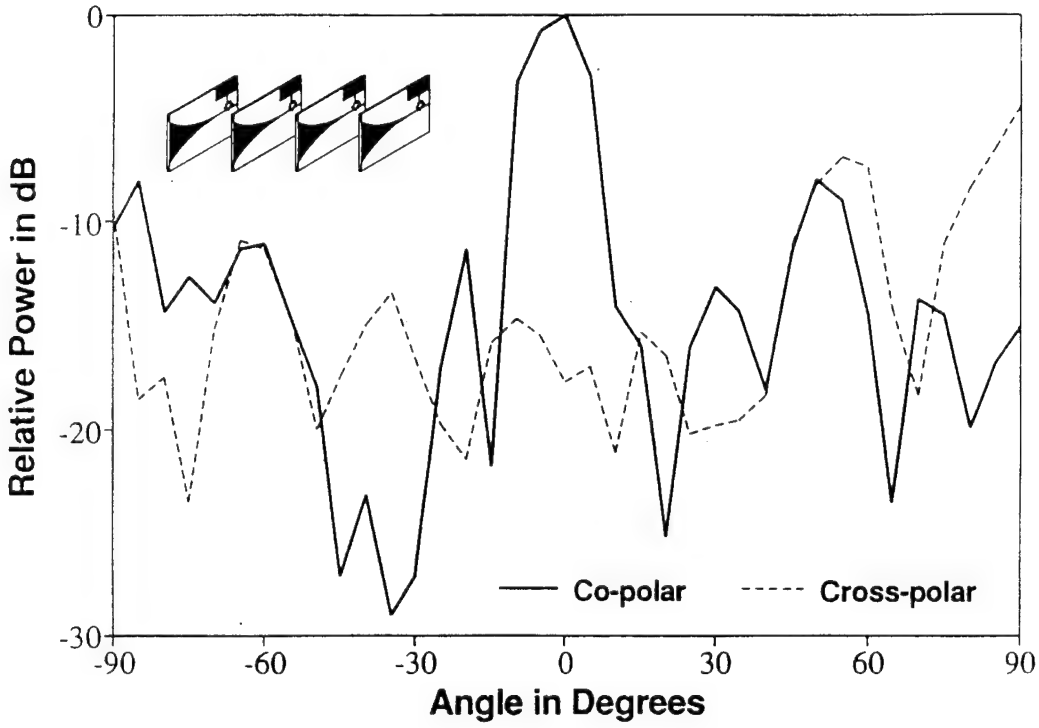

(d)

Figure 6. (continued) (c) Gunn inverted stripline patch power combiner, and (d) FET notch antenna power combiner.

In experiments, a H-plane beam steering of 40 degrees has been demonstrated using four inverted stripline active antenna elements. The results are shown in Figure 7.

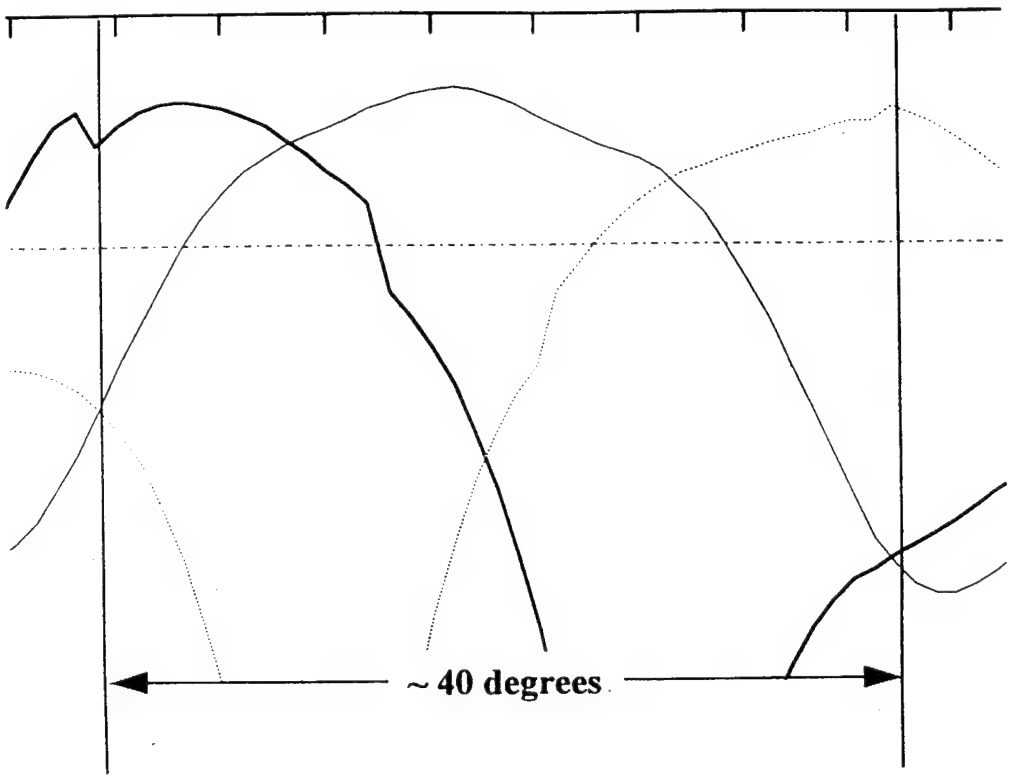

Figure 7. Beam steering results for a four-element H-plane combining array.

4. Quasi-Optical Components

At millimeter-wave and submillimeter-wave frequencies, the quasi-optical components have many advantages of low cost, low losses, high performance, and ease of fabrication. Under this project, a quasi-optical low loss Fabry-Perot filter and a dual polarized circular patch rectenna were developed.

4.1. Low Loss Fabry-Perot Bandpass Filter

Low loss bandpass filters consisting of Fabry-Perot resonators excited by slots which couple to higher order resonator modes were developed. The key to low loss is the efficient coupling using a waveguide opening covered by a thin half- wavelength resonant slot. This coupling method can also be applied to Fabry-Perot diplexers, power combiners and antennas.

Figure 8 shows the filter configuration [17]. For close reflector spacing, the slots efficiently couple power from rectangular waveguide to the TEM_{400} and TEM_{300} modes of the resonator. At Ka-band the filters have insertion losses of less than 1 dB in general and less than 0.5 dB in some cases. The slot width is 0.1 mm and slot length 7.1 mm. The unloaded Q values of the filters range from 1500 to 3000. The filters are mechanically tunable over a 25% bandwidth from 27 to 36 GHz. The filters should have many applications at millimeter-wave and submillimeter-wave frequencies where conventional filters have higher losses and lower values of Q.

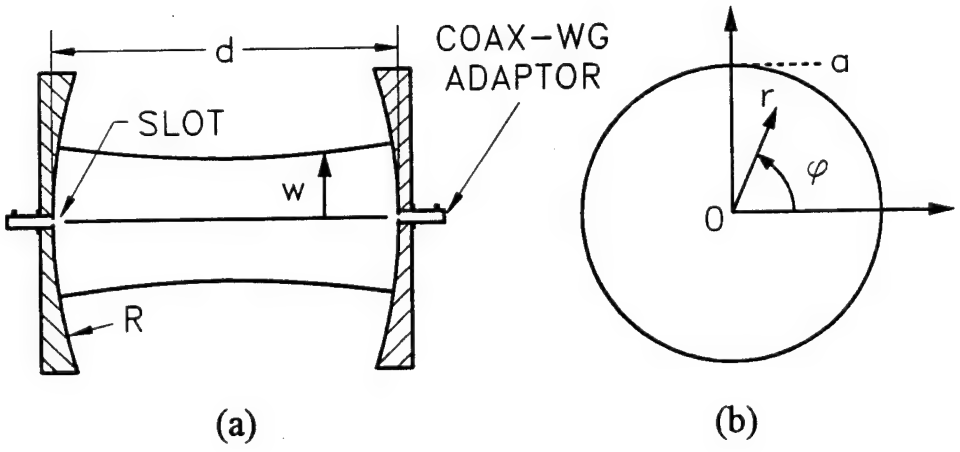

Figure 8. (a) Concave-concave Fabry-Perot resonator fed by waveguides through slots, (b) the transverse coordinate system. The reflectors have radii of curvature R, radii a, and are separated by an axial distance d. W is the beam radius.

4.2. Dual Polarized Circular Patch Rectifying Antenna

A rectifying antenna (rectenna) is a receiving antenna attached to a rectifying circuit that efficiently converts microwave power into useful DC power. It is basically a high efficiency quasi-optical detector operating in a large-signal condition. A rectenna is a fundamental component in microwave power transmission systems. Past rectenna design have primarily used a horizontal dipole over a reflecting plane as the antenna. The dipole rectenna has the disadvantage of linear polarization, bulkiness, and harmonic radiation. The use of dual polarized circular patch rectenna as shown in Figure 9 could overcome these problems [18]. A prototype 2.45 GHz rectenna was developed to convert microwave energy to DC power. Dual polarization is achieved by two orthogonal microstrip feed line. Rectification is achieved by GaAs Schottky-barrier diodes located on each feed line. A 48% conversion efficiency from microwave power to DC power was achieved. The design was based on a nonlinear circuit analysis.

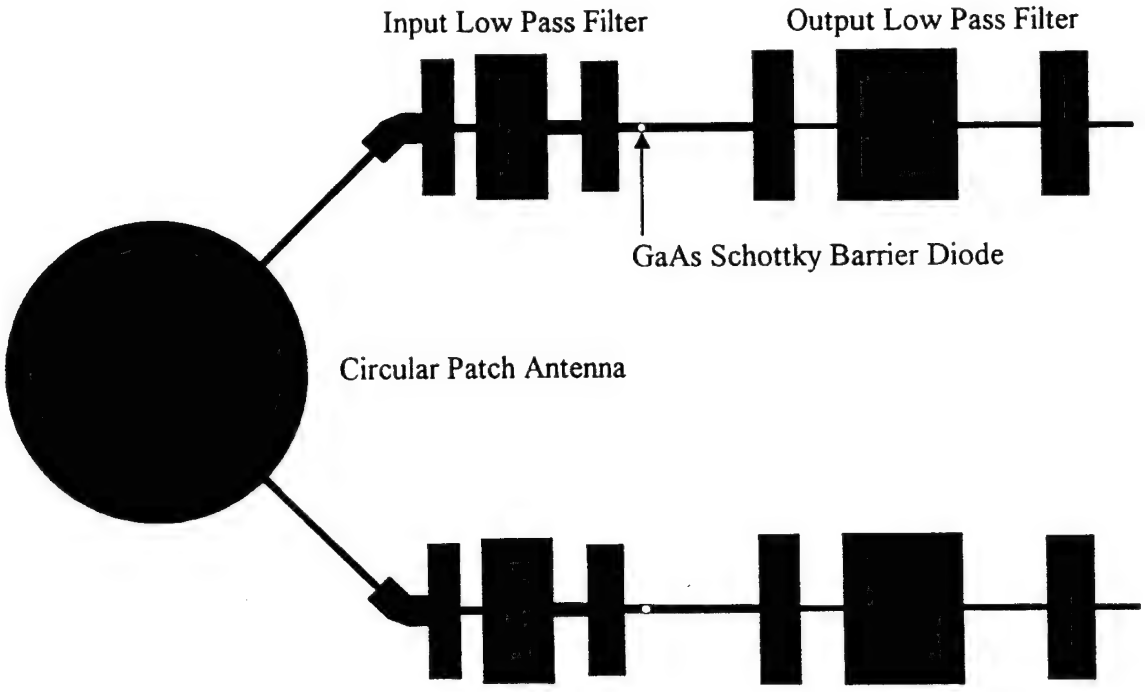

Figure 9. Dual polarized circular patch rectifying antenna circuit layout.

5. Novel Uniplanar Slotline and Coplanar Waveguide Circuits and Components

In recent years slotline and coplanar waveguide (CPW) have emerged as an alternative to microstrip in microwave and millimeter-wave integrated circuits. The fact that the center conductor and ground planes are on the same side of the substrate allows series and shunt connections of passive and active solid-state devices. Use of CPW also avoids the need for via holes to connect the center conductor to ground which should help to reduce processing complexity and to increase yield in monolithic implementations.

Using the combination of slotline and coplanar waveguides, many novel components such as hybrid ring couplers, magic-Ts, branch-line couplers, and transitions have been developed with broadband characteristics. Ring resonators and dual-mode filters using slotline or CPW have also been demonstrated.

5.1. Broadband Coplanar Waveguide to Slotline Transitions

Coplanar waveguide and slotline are the fundamental transmission lines useful in MIC and MMIC. To fully utilize the advantages of uniplanar structures the transition between CPW and slotline is necessary. Extensive study and modeling have been carried out to investigate various transition configurations. Eight different CPW to slotline transitions as shown in Figure 10 have been evaluated experimentally and theoretically [19-22]. The transition shown in Figure 10(g) gives the best performance with a 5.2 : 1 bandwidth of less than 1 dB insertion loss from 1.1 to 5.7 GHz. Other transitions have a bandwidth ranging from 1.6 : 1 to 4.1 : 1.

5.2. Hybrid-Ring Couplers, Branch-Line Couplers, and Magic-Ts

Novel uniplanar 180° and 90° hybrids suitable for MIC and MMIC applications have been developed. Figure 11 shows the 180° crossover hybrid-ring coupler and the 90° branch-line directional coupler [20]. The crossover hybrid-ring coupler uses a slotline T-junction as a phase inverter. The coupler has a bandwidth of more than one octave with ±0.4 dB power dividing balance and ± 1° phase balance. The branch-line coupler uses a coupled rectangular slotline ring as the coupling region. The coupler has over 20 dB isolation over a bandwidth of more than 40% with ± 1 dB power dividing balance.

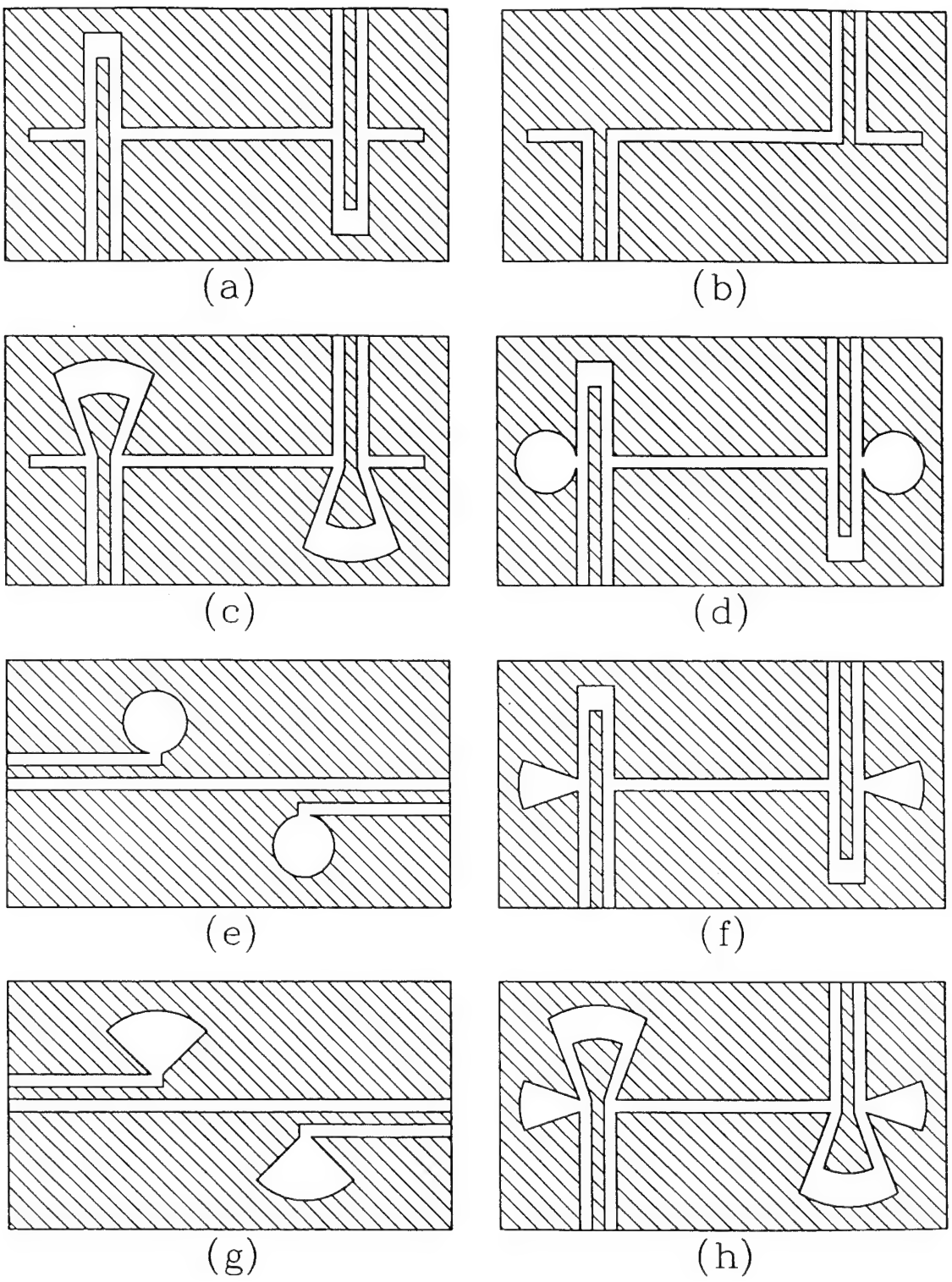

Figure 10. Eight different CPW to slotline transition configurations.

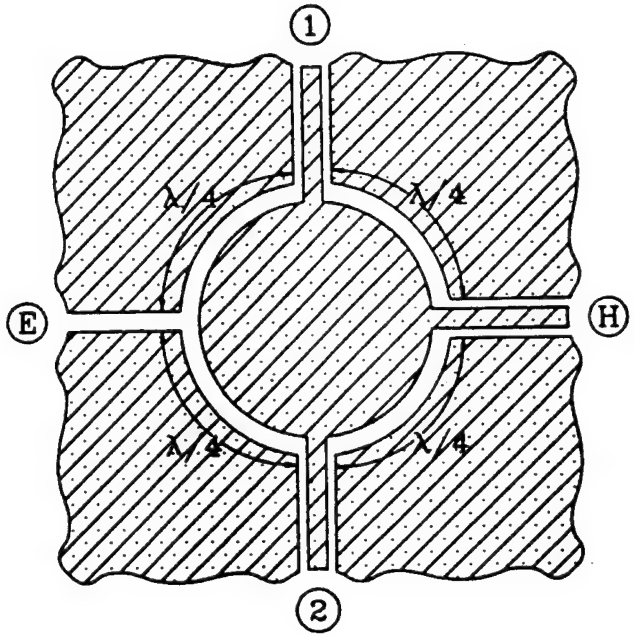

(a)

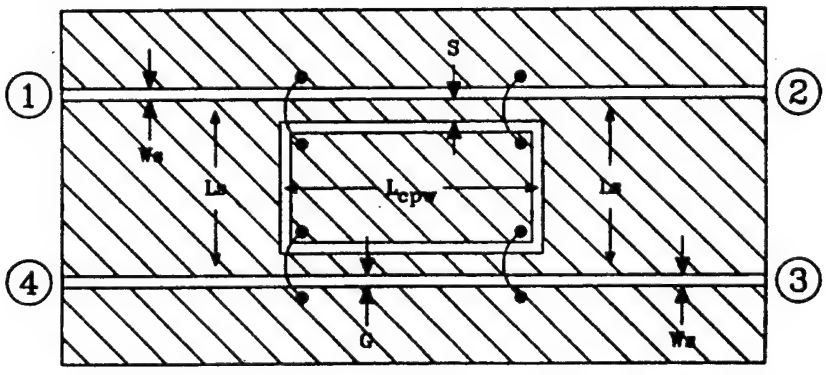

(b)

Figure 11. (a) Uniplanar crossover hybrid ring coupler,
(b) uniplanar branch line coupler.

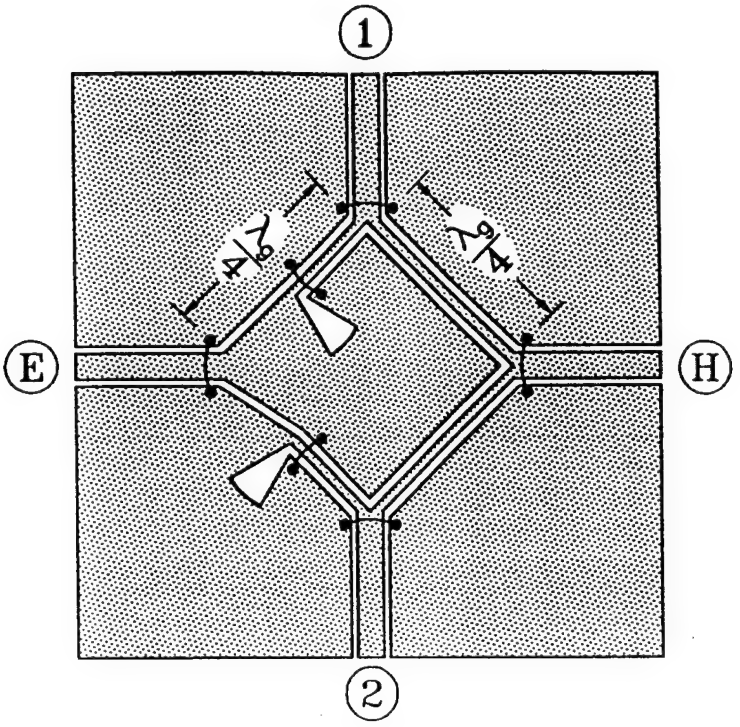

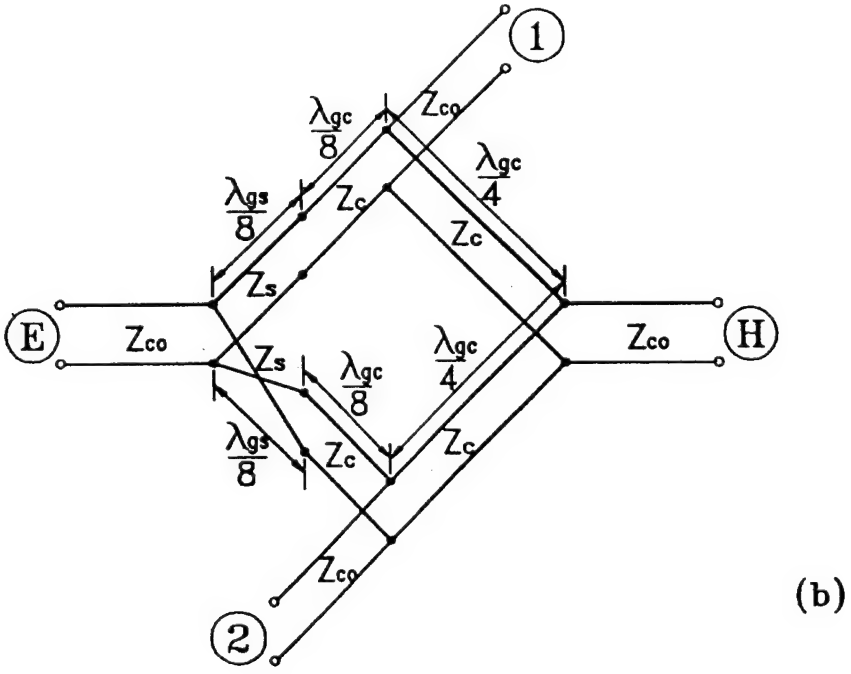

Figure 12. The uniplanar magic-T (a) circuit configuration, (b) equivalent circuit model.

Figure 12 shows a new uniplanar magic-T and its equivalent circuit [22]. Magic-Ts are fundamental components for many microwave circuits such as power combiners and dividers, balanced mixers, and frequency discriminators. The new magic-T consists of a 180° reverse-phase CPW-slotline tee junction and three CPW tee junctions. The 180° reverse phase CPW-slotline tee junction is used as a phase inverter. Ports E and H correspond to the E and H arm of the conventional waveguide magic-T, respectively. Ports 1 and 2 are the power dividing balanced arms. Experimental results show that the magic-T has a bandwidth of one octave from 2 to 4 GHz with 0.4 dB amplitude imbalance and 3.5° phase imbalance. The circuit provides good amplitude and phase characteristic over a broad bandwidth due to the phase change of the circuit being independent of frequency.

5.3. Uniplanar Ring Resonators and Dual Mode Filters

Various slotline and CPW ring resonators have been demonstrated under this project [23, 24]. Figure 13 shows the circuit configuration of a slotline ring resonator with different coupling schemes [23]. Figure 14(a) shows a varactor tunable slotline ring and Figure 14(b) shows a varactor tunable coplanar waveguide ring [24]. More than 22%

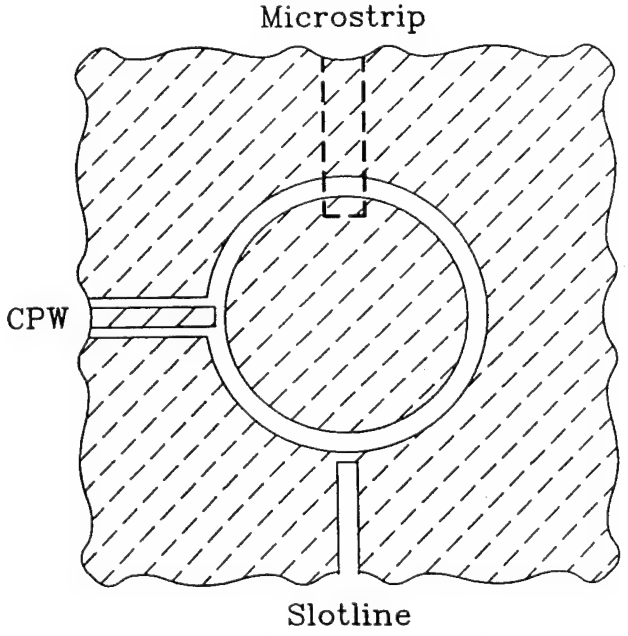

Figure 13. Circuit configuration of slotline ring resonator with different coupling schemes.

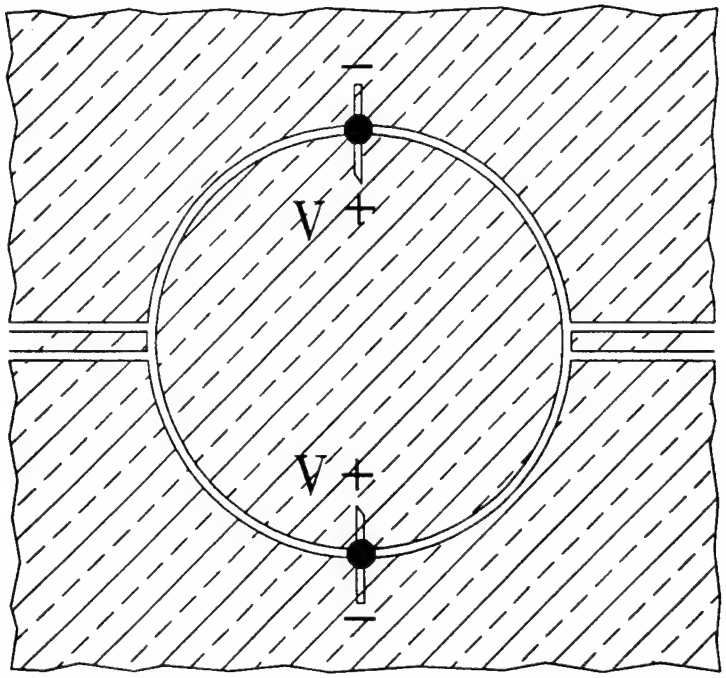

(a)

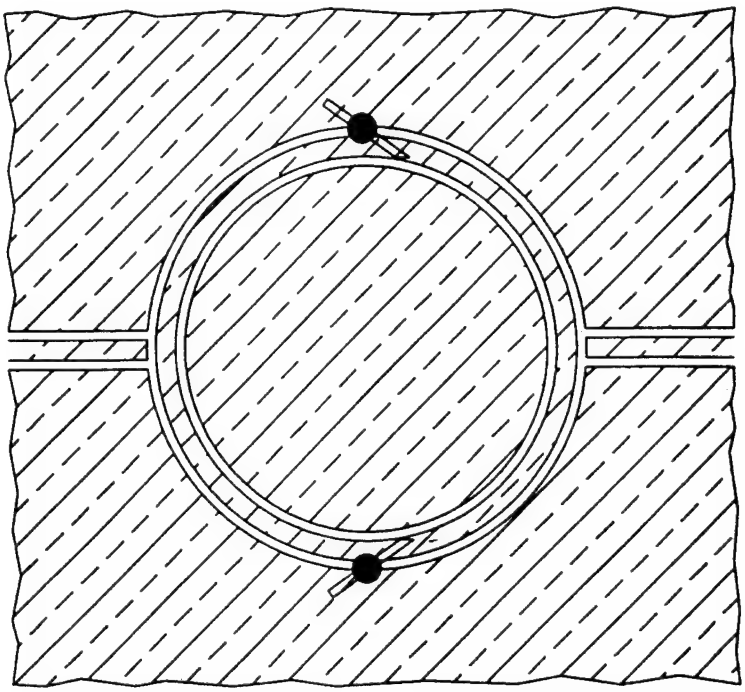

(b)

Figure 14. (a) Varactor-tunable slotline ring, (b) varactor-tunable coplanar waveguide ring.

tuning bandwidth has been achieved for both circuits. The frequency responses of these circuits agree very well with those calculated using distributed transmission line model.

Using the slotline ring with perturbation symmetrically located at 45° or 135°, the dual modes can be excited [23]. Figure 15 shows a slotline dual mode filter configuration.

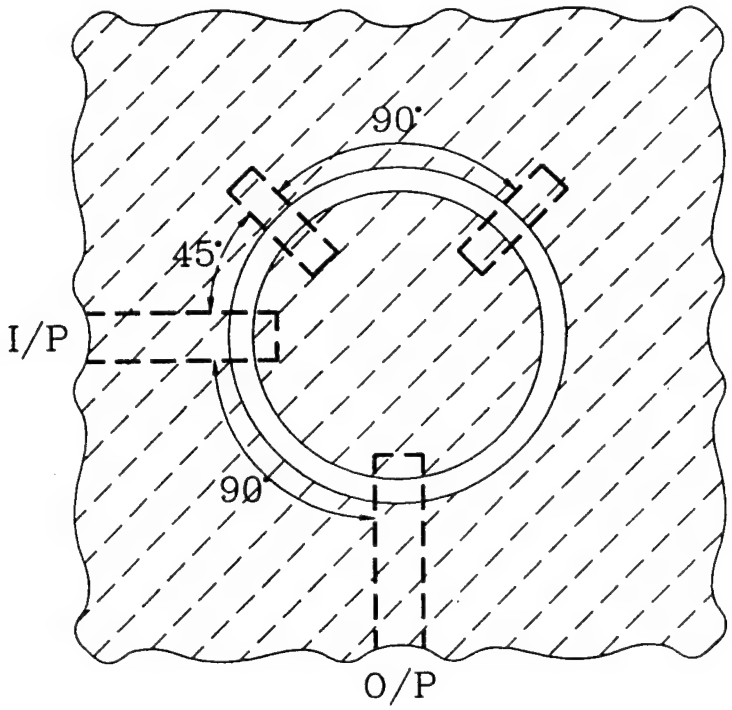

Figure 15. The slotline dual-mode filter configuration.

The dual mode filter is very compact and operates with mode number n=3. It has a bandwidth of 12.3% and a stopband attenuation of more than 30 dB. The performance of the slotline dual mode filter is shown in Figure 16.

5.4. Coplanar Waveguide Fed Dipole Antenna

A broadband balun has been developed to feed a dipole antenna. The balun is a wideband transition from CPW to CPS accomplished by using a hollow, circular patch as shown in Figure 17 [25]. The two back-to-back transitions exhibit an insertion loss of less than 1 dB from DC to 4.8 GHz and a return loss of greater than 12 dB [26]. The antenna can be designed to operate at dual frequencies [27].

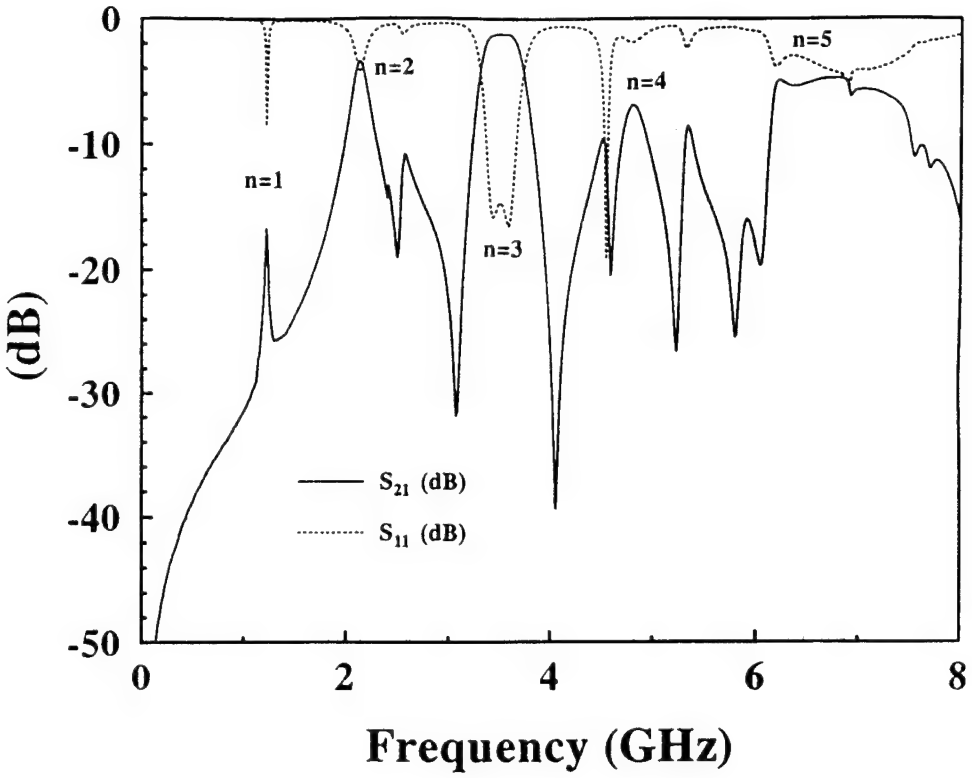

Figure 16. The performance of the slotline ring dual-mode filter.

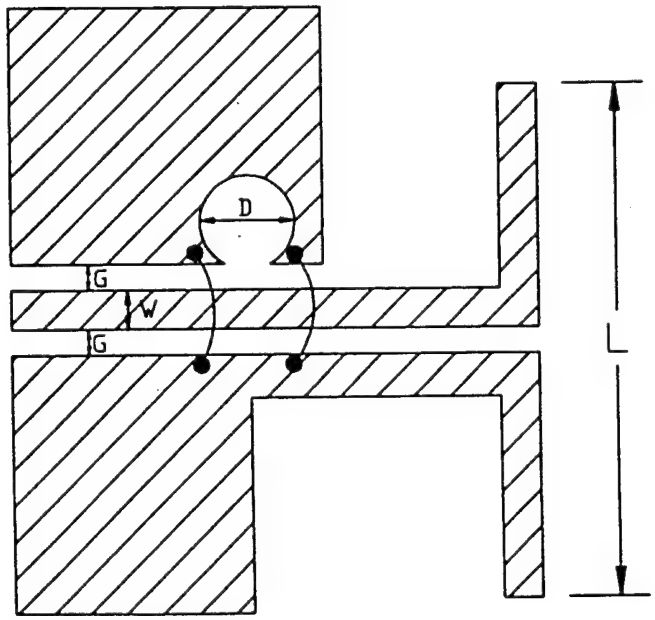

Figure 17. Circuit configuration for CPW-fed CPS dipole.

6. Other Circuits and Modeling

In addition to the research in active antennas, spatial power combining and beam steering, quasi-optical components, and uniplanar slotline and coplanar waveguide circuits and components, work was carried out in the modeling of FET, the development of low-loss wideband interconnects, and the development of simple de-embedding measurements techniques. This section will give a brief description of theses accomplishments.

6.1. Modeling of Gunn Domain Effects in MESFETs

The validity of the standard small-signal GaAs MESFET is questionable when it was applied to the fitting of measured data above 15 GHz. A time-delay element associated with the output conductance has been included in the equivalent circuit to model the Gunn domain effects [28]. From experimental data collected to 36 GHz, these effects primarily contribute to decrease of the output conductance with increasing frequency. The inclusion of the Gunn effects improves the small-signal model significantly at high frequencies.

6.2. Broadband Interconnects for Microstrip Lines

An analysis was developed for an interconnect based on a narrow rectangular slot on the common ground plane of two microstrip lines [29]. Figure 18 shows the circuit configuration. The analysis was based on a moment method procedure applied to several integral equations that were formulated by Green's functions of the grounded dielectric slabs and unknown electric and magnetic currents. Low insertion loss over an octave bandwidth was achieved for this interconnect. The theoretical results agree very well with measurements.

Using the aperture coupling, a new planar multilayer quadrature coupler was developed. Figure 19 shows the 3-D view of the coupler [30]. The new multilayer coupler consists of two virtually-terminated narrow slots in a common ground plane. Experimental results are in fairly good agreement with the theory.

6.3. A Simple De-Embedding Measurement Technique

The characterization of Scattering parameters of microwave devices is a fundamental problem in microwave measurements. The S-parameters of a device under test (DUT) with coaxial connectors can be measured directly by using automatic network analyzer.

Measurements on devices with noncoaxial terminals require suitable transitions and interface fixtures between the DUT and the measurement system. The interface fixtures and calibration components are difficult to build with a high degree of accuracy, especially at the higher frequencies. To overcome this problem, a simple divide-by de-embedding method was devised for transmission coefficient measurements of microwave devices with noncoaxial terminals [31]. The measurement error of this method were analyzed and the error equations were derived to provide a criterion for evaluating and estimating the measurement errors of the method. The method has been successfully used to measure many devices and components.

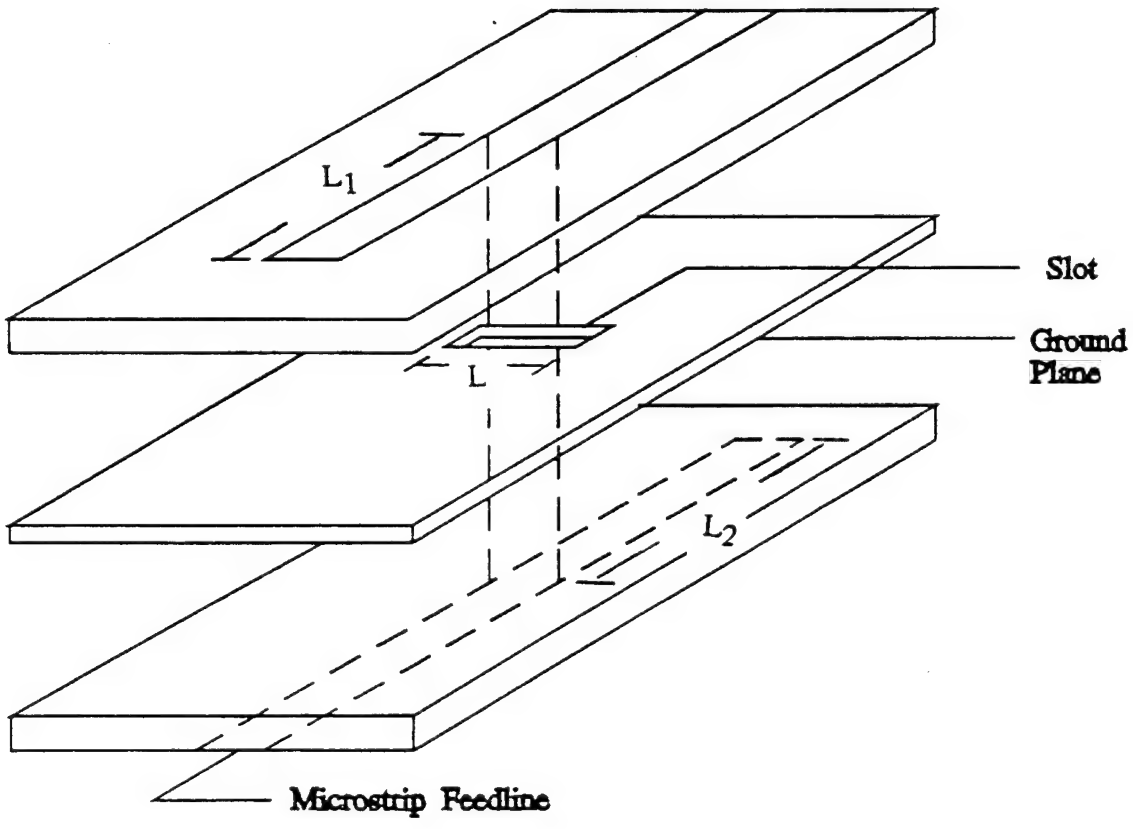

Figure 18. Slot-coupled double layer microstrip line configuration.

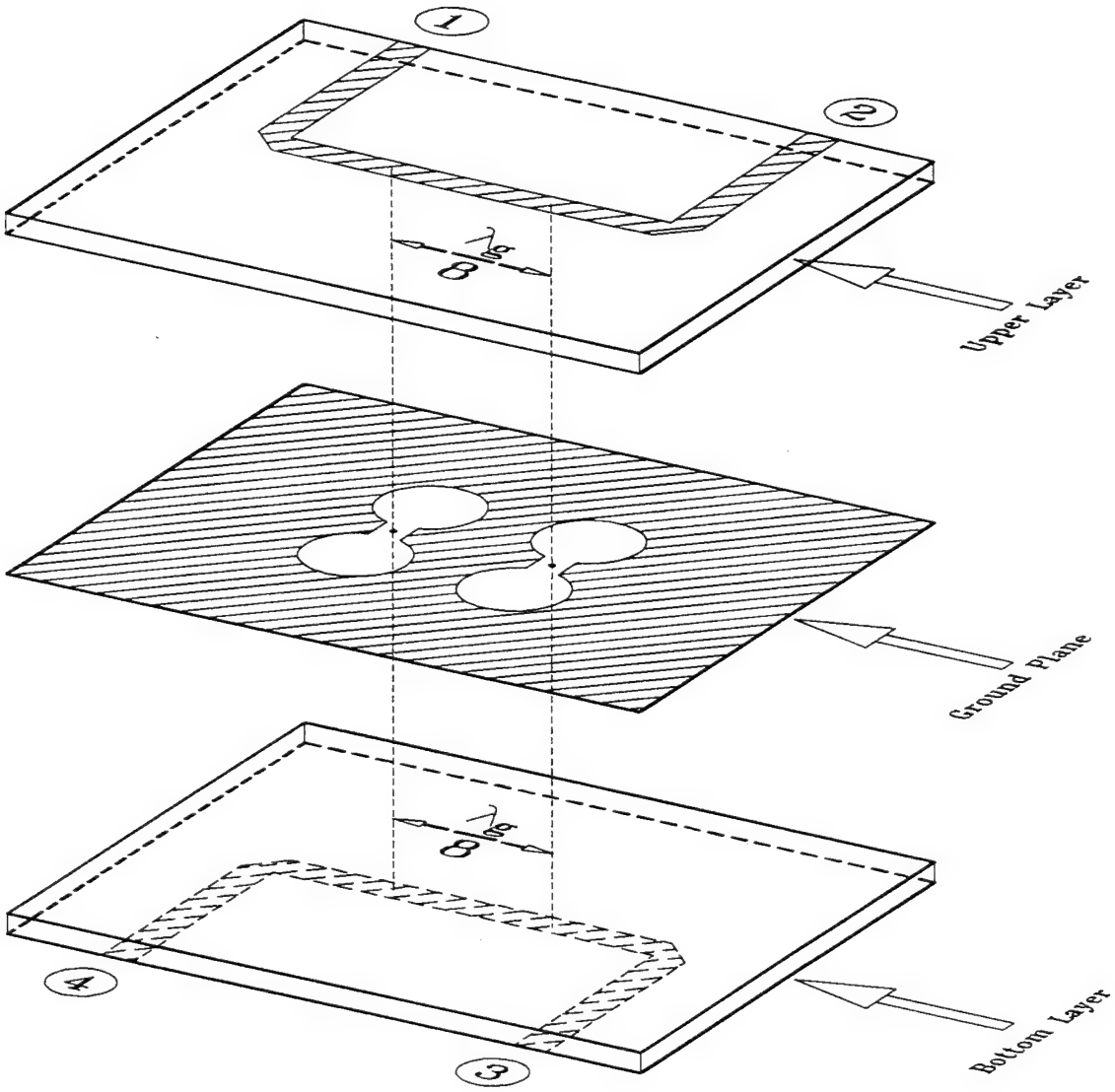

Figure 19. 3-D view of the vertical interconnect quadrature directional coupler.

7. Books and Book Chapters

As a result of this research project, two books have been written and one book chapter will be prepared. The objectives of these books are to summarize our research results, to review the technology, and to stimulate further research and applications.

7.1. Microwave Ring Circuits and Antennas

The manuscript of this book was complete. The book is in production and will be published by Wiley in February 1996. The book covers most ring resonators or cavities in various transmission lines such as microstrip, slotline, coplanar waveguide, and waveguide. It starts with a general discussion of analysis, theory, modeling, modes , coupling methods, and perturbation methods. After these general topics, the applications of ring circuits to measurements, filters, couplers, antennas, frequency selective surfaces, mixers, oscillators, and microwave optoelectronics are described. These applications are supported by real circuit demonstrations and actual circuit performance. The implementation of solid-state devices for tuning and switching the resonance is also discussed. The book should be a useful reference for engineers and scientists.

7.2. Integrated Active Antennas and Spatial Power Combining

The manuscript of this book has been completed and the book will be published by Wiley in June 1996. This book pieces together information from different areas which are necessary to understand integrated and active antennas. It emphasizes active antennas and power combining applications and consolidates the work from many researchers and investigators. Several early chapters lay the foundation for oscillator, antenna, array and power combining theory. Active antennas have been classified according to function to facilitate comparison. These include the active antennas and spatial power combiners built in patches, grids, notches, and other antennas. Various active and integrated antenna components are discussed including the integration with oscillators, amplifiers, mixers, detectors, rectennas, multipliers, phase-shifters, and switches. Overall, this book attempts to give the reader a complete review of the previous integrated and active integrated antenna work.

7.3. Active Microstrip Antennas

A book chapter entitled "Active Microstrip Antennas" will be included in a book "Advances in Microstrip and Printed Antennas" edited by K. F. Lee. The book will be published by Wiley in March 1997.

References

1. K. Chang and C. Sun, "Millimeter-wave Power Combining Techniques," *IEEE Trans. on Microwave Theory and Techniques,* Vol. MTT-31, No. 2, Feb. 1983, pp. 91-107.

2. J. W. Mink, "Quasi-Optical Power Combining of Solid-State Millimeter-Wave Sources," *IEEE Trans. on Microwave Theory and Techniques,* Vol. MTT-34, No. 2, Feb. 1986, pp. 273-279.

3. J. A. Navarro, L. Fan and K. Chang, "Active Inverted Stripline Circular Patch Antennas for Spatial Power Combining," *IEEE Trans. on Microwave Theory and Techniques,* Vol. MTT-41, No. 10, Oct. 1993, pp. 1856-1863.

4. J. A. Navarro, L. Fan and K. Chang, "Novel FET Integrated Inverted Stripline Patch," *Electronics Letters,* Vol. 30, No. 8, April 14, 1994, pp. 655-657.

5. X. Wu and K. Chang, "Dual FET Active Patch Elements for Spatial Power Combiners," *IEEE Trans. on Microwave Theory and Techniques,* Vol. MTT-43, No. 1, January 1995, pp. 26-30.

6. X. Wu and K. Chang, "Novel Active FET Circular Patch Antenna Arrays for Quasi-Optical Power Combining," *IEEE Trans. on Microwave Theory and Techniques,* Vol. MTT-42, No. 5, May 1994, pp. 766-771.

7. W. K. Leverich, X. Wu and K. Chang, "FET Active Slotline Notch Antennas for Quasi-Optical Power Combining," *IEEE Trans. on Microwave Theory and Techniques,* Vol. MTT-41, No. 9, September 1993, pp. 1515-1518.

8. W. K. Leverich, X. D. Wu and K. Chang, "A 3×3 Quasi-Optical Power Combining Array Using FET Active Notch Antennas," *Microwave and Optical Technology Letters,* Vol. 9, No. 4, July 1995, pp. 196-198.

9. C. H. Ho, L. Fan and K. Chang, "New FET Active Slotline Ring Antenna," *Electronics Letters,* Vol. 29, No. 6, March 18, 1993, pp. 521-522.

10. Z. Ding, L. Fan and K. Chang, "A New Type of Active Antenna for Coupled Gunn Oscillator Driven Spatial Power Combining Arrays," *IEEE Microwave and Guided Wave Letters,* Vol. 5, No. 8, August 1995, pp. 264-266.

11. X. Wu and K. Chang, "Compact Wideband Active Slot Antenna Amplifier," *Electronics Letters,* Vol. 29, No. 5, March 4, 1993, pp. 496-497.

12. X. D. Wu and K. Chang, "Integrated Active Slot Dipole Antenna Amplifier," *Microwave and Optical Technology Letters,* Vol. 6, No. 15, December 5, 1993, pp. 856-857.

13. J. A. Navarro and K. Chang, "Inverted Stripline Antennas Integrated with Passive and Active Solid-State Devices," *IEEE Trans. on Microwave Theory and Techniques,* Vol. MTT-43, No. 9, September 1995, pp. 2059-2065.

14. R. Flynt, L. Fan, J. A. Navarro and K. Chang, "Low Cost and Compact Active Integrated Antenna Transceiver for System Applications," *1995 IEEE MTT-S International Microwave Symposium Digest,* Vol. 2, pp. 953-956, Orlando, Florida, May 1995.

15. Z. Ding and K. Chang, "Modes and Their Stability of a Symmetric Two-Element Coupled Negative Conductance Oscillator Driven Spatial Power Combining Array," Submitted to *IEEE Trans. on Microwave Theory and Techniques.*

16. J. A. Navarro and K. Chang, "Electronic Beam-Steering of Active Antenna Array," *Electronics Letters,* Vol. 29, No. 3, February 4, 1993, pp. 302-304.

17. J. McCleary, M. Li and K. Chang, "Ka-Band Slot-Fed Higher-Order-Mode Low-Loss Fabry-Perot Filters," *IEEE Trans. on Microwave Theory and Techniques,* Vol. MTT-42, No. 7, July 1994, pp. 1423-1426.

18. J. O. McSpadden and K. Chang, "A Dual Polarized Circular Patch Rectifying Antenna at 2.45 GHz for Microwave Power Conversion and Detection," *1994 IEEE MTT-S International Microwave Symposium Digest,* Vol. 3, pp. 1749-1752, San Diego, CA, May 1994.

19. C. H. Ho, L. Fan and K. Chang, "Experimental Investigations of CPW-Slotline Transitions for Uniplanar Microwave Integrated Circuits," *1993 IEEE MTT-S International Microwave Symposium Digest,* Vol. 2, pp. 877-880, Atlanta, Georgia, June 1993.

20. C. H. Ho, L. Fan and K. Chang, "Broad-Band Uniplanar Hybrid-Ring and Branch-Line Couplers," *IEEE Trans. on Microwave Theory and Techniques,* Vol. MTT-41, No. 12, December 1993, pp. 2116-2125.

21. C. H. Ho, L. Fan and K. Chang, "Transmission Line Modeling of CPW-Slotline Transitions and CPW Butterfly Filters," *1994 IEEE MTT-S International Microwave Symposium Digest,* Vol. 3, pp. 1305-1308, San Diego, CA, May 1994.

22. C. H. Ho, L. Fan and K. Chang, "New Uniplanar Coplanar Waveguide Hybrid-Ring Couplers and Magic-Ts," *IEEE Trans. on Microwave Theory and Techniques,* Vol. MTT-42, No. 12, December 1994, pp. 2440-2448.

23. C. H. Ho, L. Fan and K. Chang, "Slotline Annual Ring Elements and Their Applications to Resonator, Filter and Coupler Design," *IEEE Trans. on Microwave Theory and Techniques,* Vol. MTT-41, No. 9, September 1993, pp. 1648-1650.

24. J. A. Navarro and K. Chang, "Varactor-Tunable Uniplanar Ring Resonators," *IEEE Trans. on Microwave Theory and Techniques,* Vol. MTT-41, No. 5, May 1993, pp. 760-766.

25. K. Tilley, X. D. Wu and K. Chang, "Coplanar Waveguide Fed Coplanar Strip Dipole Antenna," *Electronics Letters,* Vol. 30, No. 3, February 3, 1994, pp. 176-177.

26. K. Tilley, X. D. Wu and K. Chang, "Wideband Transition from Conductor-Backed Coplanar Waveguide to Modified Coplanar Stripline Using Multiple Substrates," *Electronics Letters,* Vol. 29, No. 23, November 11, 1993, pp. 2051-2052.

27. K. Tilley, X. D. Wu and K. Chang, "Dual Frequency Coplanar Strip Dipole Antenna," *1994 IEEE AP-S International Antennas and Propagation Symposium Digest,* Vol. 2, pp. 928-931, Seattle, Washington, June 1994.

28. M. A. Magerko and K. Chang, "Modeling of Gunn Domain Effects in the Output Conductance of the High-Frequency Small Signal GaAs MESFET Equivalent Circuit," *Microwave and Optical Technology Letters*, Vol. 5, No. 14, December 20, 1992, pp. 748-752.

29. G. Luong and K. Chang, "Interconnect of Microstrip Lines Through a Narrow Rectangular Slot in the Common Ground Plane," *Microwave and Optical Technology Letters*, Vol. 5, No. 8, July 1992, pp. 388-393.

30. C. H. Ho, L. Fan, G. Luong and K. Chang, "Directional Couplers Between Double-Sided Substrate Microstrip Lines Using Virtually-Terminated Coupling Slots," *IEEE Microwave and Guided Wave Letters,* Vol. 3, No. 3, March 1993, pp. 80-81.

31. M. Li, K. A. Hummer and K. Chang, "A Simple Divide-By De Embedding Measurement Method: Applications and Error Analysis," *Microwave Journal*, Vol. 36, No. 9, September 1993, pp. 118-127.

List of Personnel

1.	Principal Investigator:	Kai Chang	
2.	Research Associates:	L. Fan	X. D. Wu
3.	Research Assistants: /Students	Z. Ding	M. Magerko
		R. A. Flynt	J. C. McCleary
		B. R. Heimer	J. O. McSpadden
		C. Ho	C. M. Montiel
		K. A. Hummer	J. A. Navarro
		W. K. Leverich	K. A. Tilley
		G. Luong	T. Yoo
4.	Degree Awarded		
	Master of Science:	G. Luong	August 1992
		W. K. Leverich	August 1993
		J. O. McSpadden	December 1993
		K. A. Tilley	August 1994
		R. A. Flynt	December 1995
	Ph. D:	T. Yoo	December 1993
		C. Ho	May 1994
		K. A. Hummer	May 1994
		J. A. Navarro	December 1995

List of Publications Under ARO Support

I. Book Publications

B1. K. Chang, *Microwave Ring Circuits and Antennas*, Wiley Interscience, John Wiley, to be published in March 1996.

B2. J. A. Navarro and K. Chang, *Integrated Active Antennas and Spatial Power Combining*, Wiley Interscience, John Wiley, to be published in June 1996.

B3. J. A. Navarro and K. Chang, "Active Microstrip Antennas" Chapter in *Advances in Microstrip and Printed Antennas*, Edited by K. F. Lee, John Wiley, to be published in 1997.

II. Journal Publications

J1. X. D. Wu, K. Leverich and K. Chang, "Novel FET Active Patch Antenna," *Electronics Letters*, Vol. 28, No. 20, September 24, 1992, pp. 1853-1854.

J2. J. A. Navarro and K. Chang, "Broadband Electronically Tunable Integrated Circuit Active Radiating Elements and Power Combiners," (Invited Paper) *Microwave Journal*, Vol. 35, No. 10, October 1992, pp. 87-101.

J3. W. K. Leverich, X. Wu and K. Chang, "New FET Active Notch Antenna," *Electronics Letters*, Vol. 28, No. 24, November 19, 1992, pp. 2239-2240.

J4. M. A. Magerko and K. Chang, "Modeling of Gunn Domain Effects in the Output Conductance of the High-Frequency Small Signal GaAs MESFET Equivalent Circuit," *Microwave and Optical Technology Letters*, Vol. 5, No. 14, December 1992, pp. 748-752.

J5. J. O. McSpadden, T. Yoo and K. Chang, "Theoretical and Experimental Investigation of a Rectenna Element for Microwave Power Transmission," *IEEE Trans. on Microwave Theory and Techniques*, Vol. MTT-40, No. 12, December 1992, pp. 2359-2366.

J6. J. A. Navarro and K. Chang, "Electronic Beam-Steering of Active Antenna Array," *Electronics Letters*, Vol. 29, No. 3, February 4, 1993, pp. 302-304.

J7. X. Wu and K. Chang, "Compact Wideband Active Slot Antenna Amplifier," *Electronics Letters*, Vol. 29, No. 5, March 4, 1993, pp. 496-497.

J8. C. H. Ho, L. Fan and K. Chang, "New FET Active Slotline Ring Antenna," *Electronics Letters*, Vol. 29, No. 6, March 18, 1993, pp. 521-522.

J9. C. H. Ho, L. Fan, G. Luong and K. Chang, "Directional Couplers Between Double-Sided Substrate Microstrip Lines Using Virtually-Terminated Coupling Slots," *IEEE Microwave and Guided Wave Letters,* Vol. 3, No. 3, March 1993, pp. 80-81.

J10. C. H. Ho, L. Fan and K. Chang, "A Broad-Band Uniplanar Branch-Line Coupler Using a Coupled Rectangular Slotline Ring," *IEEE Microwave and Guided Wave Letters,* Vol. 3, No. 6, June 1993, pp. 175-176.

J11. J. A. Navarro and K. Chang, "Varactor-Tunable Uniplanar Ring Resonators," *IEEE Trans. on Microwave Theory and Techniques,* Vol. MTT-41, No. 5, May 1993, pp. 760-766.

J12. M. Li, K. A. Hummer and K. Chang, "A Simple Divide-By De-Embedding Measurement Method: Applications and Error Analysis," *Microwave Journal,* Vol. 36, No. 9, September 1993, pp. 118-127.

J13. W. K. Leverich, X. Wu and K. Chang, "FET Slotline Notch Antennas for Quasi-Optical Power Combining," *IEEE Trans. on Microwave Theory and Techniques,* Vol. MTT-41, No. 9, September 1993, pp. 1515-1518.

J14. J. A. Navarro, L. Fan and K. Chang, "Active Inverted Stripline Circular Patch Antennas for Spatial Power Combining," *IEEE Trans. on Microwave Theory and Techniques,* Vol. MTT-41, No. 10, Oct. 1993, pp. 1856-1863.

J15. J. McCleary, M. Li and K. Chang, "Slot-Fed Higher Order Mode Fabry-Perot Filters," *IEEE Trans. on Microwave Theory and Techniques,* Vol. MTT-41, No. 10, Oct. 1993, pp. 1703-1709.

J16. K. Tilley, X. D. Wu and K. Chang, "Wideband Transition from Conductor-Backed Coplanar Waveguide to Modified Coplanar Stripline Using Multiple Substrates," *Electronics Letters,* Vol. 29, No. 23, November 11, 1993, pp. 2051-2052.

J17. X. D. Wu and K. Chang, "Integrated Active Slot Dipole Antenna Amplifier," *Microwave and Optical Technology Letters,* Vol. 6, No. 15, December 5, 1993, pp. 856-857.

J18. C. H. Ho, L. Fan and K. Chang, "Broad-Band Uniplanar Hybrid-Ring and Branch-Line Couplers," *IEEE Trans. on Microwave Theory and Techniques,* Vol. MTT-41, No. 12, December 1993, pp. 2116-2125.

J19. K. Tilley, X. D. Wu and K. Chang, "Coplanar Waveguide Fed Coplanar Strip Dipole Antenna," *Electronics Letters,* Vol. 30, No. 3, February 3, 1994, pp. 176-177.

J20. J. A. Navarro, L. Fan and K. Chang, "Novel FET Integrated Inverted Stripline Patch," *Electronics Letters,* Vol. 30, No. 8, April 14, 1994, pp. 655-657.

J21. X. Wu and K. Chang, "Novel Active FET Circular Patch Antenna Arrays for Quasi-Optical Power Combining," *IEEE Trans. on Microwave Theory and Techniques,* Vol. MTT-42, No. 5, May 1994, pp. 766-771.

J22. J. McCleary, M. Li and K. Chang, "Ka-Band Slot-Fed Higher-Order-Mode Low-Loss Fabry-Perot Filters," *IEEE Trans. on Microwave Theory and Techniques,* Vol. MTT-42, No. 7, July 1994, pp. 1423-1426.

J23. C. H. Ho, L. Fan and K. Chang, "New Uniplanar Coplanar Waveguide Hybrid-Ring Couplers and Magic-Ts," *IEEE Trans. on Microwave Theory and Techniques,* Vol. MTT-42, No. 12, December 1994, pp. 2440-2448.

J24. X. Wu and K. Chang, "Dual FET Active Patch Elements for Spatial Power Combiners," *IEEE Trans. on Microwave Theory and Techniques,* Vol. MTT-43, No. 1, January 1995, pp. 26-30.

J25. W. K. Leverich, X. D. Wu and K. Chang, "A 3×3 Quasi-Optical Power Combining Array Using FET Active Notch Antennas," *Microwave and Optical Technology Letters,* Vol. 9, No. 4, July 1995, pp. 196-198.

J26. Z. Ding, L. Fan and K. Chang, "A New Type of Active Antenna for Coupled Gunn Oscillator Driven Spatial Power Combining Arrays," *IEEE Microwave and Guided Wave Letters,* Vol. 5, No. 8, August 1995, pp. 264-266.

J27. J. A. Navarro and K. Chang, "Inverted Stripline Antennas Integrated with Passive and Active Solid-State Devices," *IEEE Trans. on Microwave Theory and Techniques,* Vol. MTT-43, No. 9, September 1995, pp. 2059-2065.

J28. L. Fan, C. H. Ho, S. Kanamaluru and K. Chang, "Wide-Band Reduced-Size Uniplanar Magic-T, Hybrid-Ring, and De Ronde's CPW-Slot Couplers," *IEEE Trans. on Microwave Theory and Techniques,* Vol. MTT-43, No. 12, December 1995.

III. Conference Papers

C1. K. Chang, "Quasi-Optical Integrated Circuit Transmitters and Receivers," *Microwave Hybrid Circuits Conference*, Wickenburg, Arizona, October, 1992.

C2. K. Chang, "Recent Developments in Millimeter-Wave Power Transmission and Conversion," *17th International Conference on Infrared and Millimeter-Waves Digest*, pp. 272-273, Pasadena, California, December 1992.

C3. M. Li, K. A. Hummer and K. Chang, "A Simple Divide-by Measurement Method for Transmission Coefficient Measurements of Non-Coaxial Components," *17th*

International Conference on Infrared and Millimeter-Waves Digest, pp. 476-477, Pasadena, California, December 1992.

C4. G. Luong and K. Chang, "Analysis and Experiments of an Interconnect for Microstrip Lines," *17th International Conference on Infrared and Millimeter-Waves Digest*, pp. 482-483, Pasadena, California, December 1992.

C5. C. H. Ho, L. Fan and K. Chang, "Experimental Investigations of CPW-Slotline Transitions for Uniplanar Microwave Integrated Circuits," *1993 IEEE MTT-S International Microwave Symposium Digest*, Vol. 2, pp. 877-880, Atlanta, Georgia, June 1993.

C6. C. H. Ho, L. Fan and K. Chang, "A Broadband Uniplanar Slotline Hybrid Ring Coupler with Over One Octave Bandwidth," *1993 IEEE MTT-S International Microwave Symposium Digest*, Vol. 2, pp. 585-588, Atlanta, Georgia, June 1993.

C7. C. H. Ho, L. Fan and K. Chang, "Slot-Coupled Double-Sided Microstrip Interconnects and Couplers," *1993 IEEE MTT-S International Microwave Symposium Digest*, Vol. 3, pp. 1321-1324, Atlanta, Georgia, June 1993.

C8. X. Wu and K. Chang, "Coplanar Waveguide Feed Linear Tapered Slot Antenna," *1993 IEEE AP-S International Antennas and Propagation Symposium Digest*, Vol. 1, pp. 364-367, Ann Arbor, Michigan, June 1993.

C9. C. H. Ho, L. Fan and K. Chang, "On the Study of Passive and Active Slotline Ring Antennas," *1993 IEEE AP-S International Antennas and Propagation Symposium Digest*, Vol. 2, pp. 656-659, Ann Arbor, Michigan, June 1993.

C10. C. H. Ho, L. Fan and K. Chang, "New Uniplanar Coplanar Waveguide Couplers," *1994 IEEE MTT-S International Microwave Symposium Digest*, Vol. 1, pp. 285-288, San Diego, CA, May 1994.

C11. C. H. Ho, L. Fan and K. Chang, "Transmission Line Modeling of CPW-Slotline Transition and CPW Butterfly Filters," *1994 IEEE MTT-S International Microwave Symposium Digest*, Vol. 2, pp. 1305-1308, San Diego, CA, May 1994.

C12. J. O. McSpadden and K. Chang, "A Dual Polarized Circular Patch Rectifying Antenna at 2.45 GHz for Microwave Power Conversion and Detection," *1994 IEEE MTT-S International Microwave Symposium Digest*, Vol. 3, pp. 1749-1752, San Diego, CA, May 1994.

C13. J. A. Navarro and K. Chang, "Low-Cost Integrated Inverted Stripline Antennas with Solid-State Devices for Commercial Applications," *1994 IEEE MTT-S International Microwave Symposium Digest*, Vol. 3, pp. 1771-1774, San Diego, CA, May 1994.

C14. K. Tilley, X. D. Wu and K. Chang, "Dual Frequency Coplanar Strip Dipole Antenna," *1994 IEEE AP-S International Antennas and Propagation Symposium Digest,* Vol. 2, pp. 928-931, Seattle, Washington, June 1994.

C15. J. A. Navarro, J. O. McSpadden and K. Chang, "Experimental Study of Inverted Microstrip for Integrated Antenna Applications," *1994 IEEE AP-S International Antennas and Propagation Symposium Digest,* Vol. 2, pp. 920-923, Seattle, Washington, June 1994.

C16. K. Chang, "Recent Progress in Active Antennas and Spatial Power Combining," (Invited Paper) *3rd International Conference on Millimeter-Wave and Far-Infrared Technology,* pp. 57-60, Guangzhou, China, August 1994.

C17. L. Fan, S. Kanamaluru and K. Chang, "A New Wide-Band and Reduced-Size Uniplanar Magic-T," *1995 IEEE MTT-S International Microwave Symposium Digest,* Vol. 2, pp. 667-670, Orlando, Florida, May 1995.

C18. R. Flynt, L. Fan, J. A. Navarro and K. Chang, "Low Cost and Compact Active Integrated Antenna Transceiver for System Applications," *1995 IEEE MTT-S International Microwave Symposium Digest,* Vol. 2, pp. 953-956, Orlando, Florida, May 1995.

C19. C. H. Ho, L. Fan and K. Chang, "Uniplanar De Ronde's CPW-Slot Directional Couplers," *1995 IEEE MTT-S International Microwave Symposium Digest,* Vol. 3, pp. 1399-1402, Orlando, Florida, May 1995.

C20. R. Flynt, L. Fan, J. A. Navarro and K. Chang, "Low Cost and Compact Active Integrated Antenna Transceiver for System Applications," *1995 IEEE NTC Microwave System Conference Proceedings,* pp. 89-92, Orlando, Florida, May 1995.

C21. K. Chang, "Integrated Microstrip Active Antennas and Their Applications," (Invited Paper) *1995 International Symposium on Signal, System and Electronics Conference Digest,* pp. 13-16, San Francisco, CA, October 1995.

Appendices

Appendix 1

J. A. Navarro, L. Fan and K. Chang, "Active Inverted Stripline Circular Patch Antennas for Spatial Power Combining," *IEEE Trans. on Microwave Theory and Techniques,* Vol. MTT-41, No. 10, Oct. 1993, pp. 1856-1863.

Appendix 2

J. McCleary, M. Li and K. Chang, "Slot-Fed Higher Order Mode Fabry-Perot Filters," *IEEE Trans. on Microwave Theory and Techniques,* Vol. MTT-41, No. 10, Oct. 1993, pp. 1703-1709.

Appendix 3

X. Wu and K. Chang, "Novel Active FET Circular Patch Antenna Arrays for Quasi-Optical Power Combining," *IEEE Trans. on Microwave Theory and Techniques,* Vol. MTT-42, No. 5, May 1994, pp. 766-771.

Appendix 4

C. H. Ho, L. Fan and K. Chang, "New Uniplanar Coplanar Waveguide Hybrid-Ring Couplers and Magic-Ts," *IEEE Trans. on Microwave Theory and Techniques,* Vol. MTT-42, No. 12, December 1994, pp. 2440-2448.

Appendix 5

J. A. Navarro and K. Chang, "Inverted Stripline Antennas Integrated with Passive and Active Solid-State Devices," *IEEE Trans. on Microwave Theory and Techniques,* Vol. MTT-43, No. 9, September 1995, pp. 2059-2065.

Active Inverted Stripline Circular Patch Antennas for Spatial Power Combining

Julio A. Navarro, *Student Member, IEEE* Lu Fan, and Kai Chang, *Fellow, IEEE*

Abstract—**A new active antenna configuration is proposed for spatial power combining applications. The active patch antenna uses an inverted stripline topology to take advantage of several features. These features include avoiding drilling through the circuit substrate to insert the diode and the use of air within the resonant cavity for reducing loss. The inverted substrate can serves as a radome for hermetic sealing. The active antenna and housing can be fabricated in modular form for reduced cost and easy replaceability of devices. The active inverted stripline patch antenna exhibits a much cleaner spectrum and greater stability than previously reported active antennas. The fixture serves as a ground plane, heat sink, and support in an active planar array or as a mirror in a quasi-optical power combining resonator. A single active antenna operating at 9.23 GHz exhibited a 16 MHz locking bandwidth at 30 dB locking gain. Power combining efficiencies of over 89% have been demonstrated for a four element square array. The square array maintained injection-locking and power combining over a 60 MHz bias tuned bandwidth. Similarly, a four element diamond array showed over 86% combining efficiency and 50 MHz bias tuned bandwidth. Beam Steering was demonstrated by varying bias voltage to the individual antenna elements of the square array.**

I. Introduction

ACTIVE ANTENNAS with spatial power combining techniques have been devised to overcome low power levels and fabrication costs of mm and sub-mm wave systems. By designing the antenna and oscillator on a single substrate, one avoids transition/transmission line losses from power distribution networks and moves closer towards complete monolithic integration. At mm and sub-mm wavelengths, monolithic construction becomes necessary to overcome many fabrication difficulties. However, solid-state devices produce very small power levels at these frequencies while waveguide dimensions and tolerances become difficult and costly for circuit-level power combining. The use of active antennas and spatial or quasi-optical power combing techniques can overcome these limitations [1], [2]. General power combining techniques are reviewed in [1] while the current state of quasi-optical power combining technology is described in [3].

Active antennas are those radiators directly integrated with active devices to generate RF power. Active antennas have been realized using two terminal and three terminal devices. FETs and other three terminal solid-state devices have shown higher DC to RF conversion efficiencies over two terminal devices. However, diodes reach much higher operating frequencies. The active antenna provides a tank circuit, matching transformer or feed back mechanism to sustain oscillations. A group of active antennas can be injection-locked for phase-coherency and power combining.

The microstrip patch antenna has been integrated with diodes and transistors for active, planar, low-cost radiating elements [4]–[8]. The microstrip structure provides a resonant patch for oscillations and a ground plane for efficient heat sinking. However, the patch has exhibited narrow bias tuning ranges, high cross-polarization levels, and wide output power deviations. A tuning diode and bipolar transistor has recently been integrated within a *multi-layer* patch to obtain 4.4% tuning of the operating frequency [9]. As an alternative, the endfire notch has many desirable characteristics including broad impedance matching bandwidth, uniplanar nature and easy integration of other planar solid-state devices. Its scalability is attractive for use well into the sub-mm wave region. Active varactor tunable notch antennas have been reported [10]–[12]. However, an array of such endfire antennas would require a brick style approach for power combining arrays. Although the brick style approach offers large heat dissipation volume and circuit area with modular replaceability of components, it tends to be bulkier than an array using a tile style method. For tile type approaches in power combining, endfire elements may not be as suitable as broadside microstrip patches, bowties, grids and dipoles.

Power combining methods enable arrays of active antennas to operate as one coherent transmitter with predictable effective radiated power, beamwidth and tuning bandwidth. Power-combining techniques include chip-level, circuit-level and spatial combiners. Spatial and open resonator combiners involve a large number of transistors or diodes. The individual free-running oscillators must be injection-locked to produce a coherent higher power RF source. Injection locking may be obtained via mutual coupling, external feedback, or an external source. The result of using spatial or quasi-optical power combining techniques is to create a single, coherent and higher-power signal from many low-power radiating sources. Spatial or quasi-optical power combining is not as limited by size, ohmic or dielectric losses or moding problems and allows the combination of a greater number of active devices. The patch and grid have been used for most active antennas and in power combining [13]–[17].

This paper introduces the cavity-enclosed inverted stripline circular patch antenna. This antenna structure does not require drilling through the circuit substrate to accommodate diodes. Drilling on the housing is still required but is not as critical. A

Manuscript received August 18, 1992; revised March 19, 1993.

The authors are with Texas A&M University, Electrical Engineering Department, College Station, Texas 77843-3128.

IEEE Log Number 9211937.

housing has been designed so that the feed or diode position is easily optimized. The configuration's enclosure chokes out surface waves and introduces an increase in metal volume for heat dissipation. DC bias is provided to the diode from the ground plane side with a feed-through capacitor. This scheme does not require direct contact with the patch radiator and can improve the impedance match to the diode. The inverted stripline active patch antenna can also be integrated with other solid-state devices for increased power, frequency switching and/or tuning. The axial symmetry of the antenna can be used for circuit level power combining with more than one active device placed under the patch radiator [18]. Monolithic integration of such an antenna in a tile type planar array could be accomplished with monolithic chip inserts at each antenna location. Each insert would contain the patch and active devices.

The active inverted stripline patch exhibits a purer spectrum than previously reported active antennas with improved stability and external Q-factor. The antenna can be optimized for improved diode matching and increased diode power output as in waveguide cavities. Injection-locking experiments on a single active antenna show a locking bandwidth 16 MHz at a locking gain of 30 dB. E and H-plane power combining arrays show high combining efficiencies. A four element square array with 89% combining efficiency showed an injection-locked bias tuning bandwidth of 60 MHz. Similarly, a four element diamond array showed over 86% combining efficiency and 50 MHz bias tuned bandwidth.

II. Circuit Design and Description

The cavity-enclosed inverted stripline antenna dimension parameters are shown in Fig. 1(a). The inverted patch is enclosed by a cylindrical air-filled cavity. The antenna radiates through a short section of dielectric-filled circular waveguide to free space. References [19] and [20] describe design formulations which were applied to this inverted stripline structure design. This structure and a coaxial probe were used to create a passive antenna.

Since the probe-fed antenna is inverted and enclosed, soldering the coaxial probe to the patch is difficult and avoided. Instead a cap on the probe is used to capacitively couple to the antenna. The cap used is equal to the Gunn diode cap diameter in anticipation of the active antenna application. Some of the passive antenna design aspects worth noting include that: the inverted substrate serves as a radome, no drilling through the circuit or soldering to the patch is required, thick antenna dimensions are allowed without surface wave losses.

A test fixture was designed to allow experimental optimization of the passive and active design. The enclosure allows the use of dielectric inserts to test different patch antenna diameters on different substrate thicknesses or dielectric constants. Fig. 1(b) shows the passive probe-fed cavity-enclosed inverted stripline configuration. Several probe-fed antennas were tested using the following parameters:

- Cavity Diameter (C) = 12.700 mm.
- Substrate Thickness (a) = 1.524 mm and $\varepsilon_2 = 2.3$.
- Air Spacing (b) = 1.500 mm and $\varepsilon_1 = 1.0$.

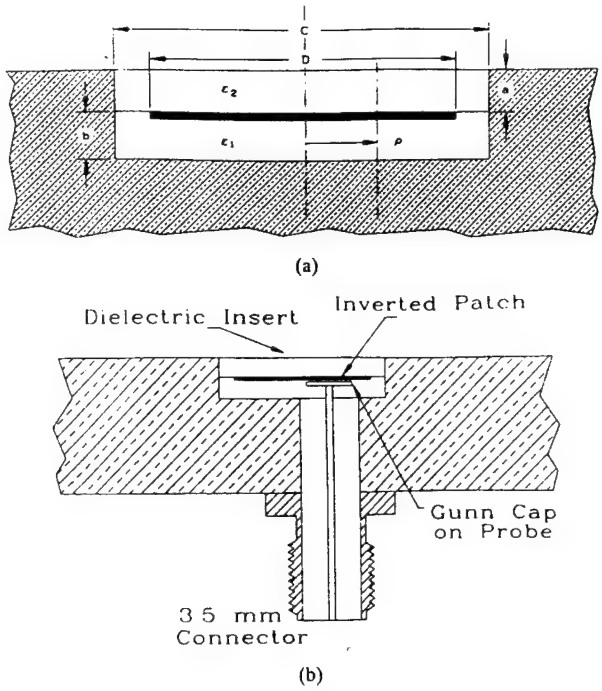

Fig. 1. The cavity-enclosed inverted stripline antenna: (a) Structure dimensions. (b) The passive probe-fed antenna configuration.

TABLE I
MEASURED AND CALCULATED OPERATING FREQUENCIES OF SEVERAL PATCH ANTENNAS

Patch Diameter (mm)	Calculated f_r (GHz)	Measured f_r (GHz)	% Error
8	13.300	13.30	0
9	12.285	12.35	−0.50
10	11.415	11.00	3.77
10.4	11.101	10.70	3.75
11	10.661	10.10	5.56

- Patch Diameters (D) = 8, 9, 10, 10.4 and 11 mm.
- 3.5 mm connector (Gunn diode cap on probe).
- Probe Position (ρ) = 2 mm.

Patch antennas with different diameters were etched on RT-Duroid 5870 with a 1.524 mm thickness and ε_r of 2.3. The antennas were concentrically cut-out in 12.7 mm diameter inserts for the cavity enclosure. Several dielectric inserts were tested for return loss on an HP-8510B Network Analyzer. Instead of soldering a probe feed to the antenna, a circular disk over the probe tip was used to simulate the Gunn diode cap of the active antenna application as shown in Fig. 2. This cap is also used as a proximity feed to tune out some of the probe's inductive effect. Table I lists computed and measured operating frequencies for several patch antennas of different diameters.

Table I shows a deviation of antenna resonance for larger patch diameters. As the patch diameter increases, the distance between the radiating edges and the enclosure decrease well within a ground plane spacing causing a lower resonance frequency. Our current formulation based on [19] and [20] does

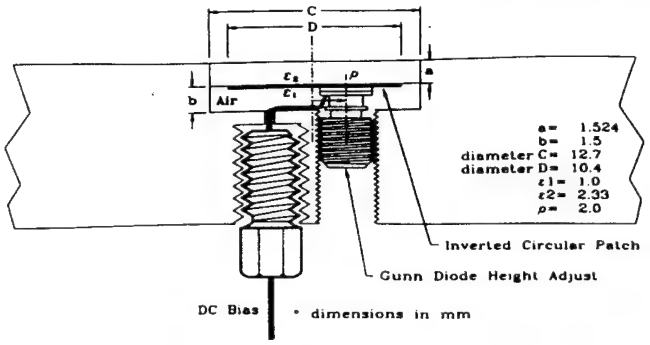

Fig. 2. The cavity-enclosed active inverted stripline antenna with Gunn diode and bias scheme.

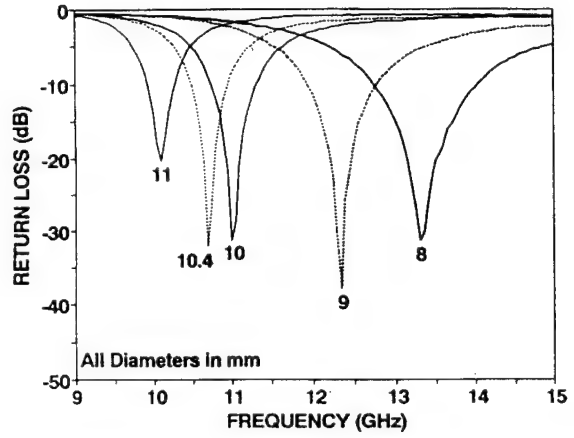

Fig. 3. The measured return loss for various patch diameters of the probe-fed passive antenna.

not account for the cavity enclosure effect on the resonance of the inverted patch antenna. Fig. 3 shows the measured return loss of several cavity-enclosed probe-fed inverted stripline antennas.

The probe-fed passive antenna radiation patterns were used to determine beamwidth, cross-polarization and gain level. The gain of the cavity-enclosed inverted stripline circular patch antenna is 6.65 dBi. This gain level is used later to approximate Gunn oscillator power in the active antenna. The E-plane 3 dB beamwidth is over 105 degrees. The H-plane 3 dB beamwidth is 80 degrees. Cross polarization levels remain at least 16 dB below the maximum on either H or E-plane patterns. Fig. 4 shows the radiation patterns for a 10.4 mm diameter probe-fed cavity-enclosed inverted stripline antenna. E-plane pattern modulation or ripple is caused by the edges of a relatively small fixture.

III. A Single Active Antenna Element

The active antenna design addresses heat dissipation and hermetic sealing concerns of active applications. Heat dissipation is specially important at higher frequencies where devices are less efficient and circuit dimensions are reduced. Fixtures or housings serve as structural support, electrical ground planes and heat sinks which dissipate heat away from active devices. This antenna includes a cavity enclosure [21] which chokes out surface waves and further increases the metal volume for heat

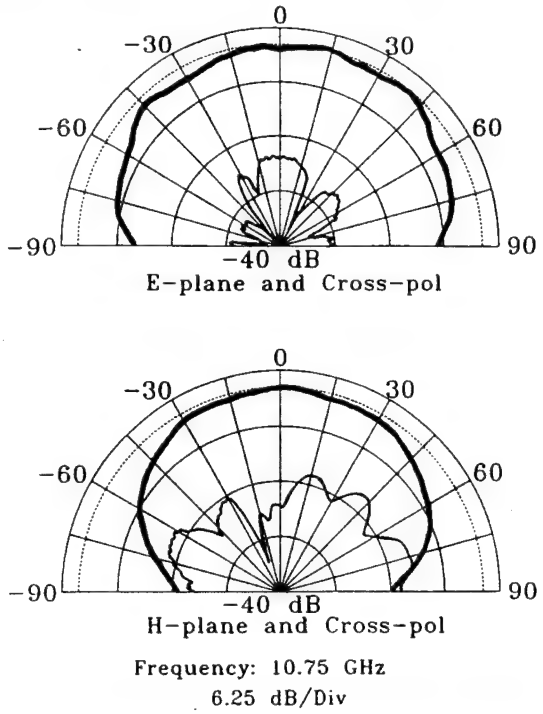

Fig. 4. The probe-fed passive antenna radiation patterns.

TABLE II
Measured Active Antenna Operating Frequency and Oscillator Power

Inverted Patch Diameter (mm)	Operating Frequency: F_0 (GHz)	Gunn Oscillator Power* (GHz)	EIRP (mW)
8	9.997	63.99	295.88
9	9.637	56.76	262.45
10	9.438	57.04	263.74
10.4	9.240	63.98	295.83
11	8.908	66.98	309.70

*Calculated using a passive antenna gain of 6.65 dBi.

dissipation. For hermetic sealing, the inverted stripline antenna insert can have matched thermal expansion coefficients with the alloy used to make the housing. The matched thermal expansion coefficients will reduce stresses and cracks in hostile environments to maintain hermeticity, increase durability and improve reliability of active devices [22].

The active cavity-enclosed inverted stripline antenna uses a screw-type diode fastened to a large base plate as shown in Fig. 2. The cavity enclosure is placed around the diode and fastened to the base plate. A circular patch antenna etched on a circular RT-Duroid dielectric insert is pressed into the cavity enclosure over the diode. The inverted patch serves as a resonant circuit for the Gunn diode. Biasing to the diode can be etched on the dielectric insert or applied through a filtering capacitor below the ground plane.

The input impedance of the antenna can be used with the equivalent circuit for the Gunn diode to determine the active antenna oscillation frequency. The Gunn diode, when biased above its threshold voltage, will oscillate if it sees a real impedance less than or equal to its own in a circuit. The

TABLE III
OPERATING FREQUENCIES AND OSCILLATOR POWER VS. GUNN BIAS VOLTAGE

Bias Voltage (Volts)	Operating Frequency F_0 (GHz)	Gunn Oscillator Power* (mW)	EIRP (mW)
8	9.003	28.31	130.90
9	9.036	38.02	175.80
10	9.067	52.64	243.40
11	9.096	60.20	278.35
12	9.119	62.93	290.98
13	9.134	67.99	314.37
14	9.143	70.56	326.26
15	9.143	75.42	348.73

*Calculated using a passive antenna gain of 6.65 dBi.

condition is depicted by the following equation:

$$|\mathrm{Re}[Z_g]| \geq \mathrm{Re}[Z_c] \tag{1}$$

where $\mathrm{Re}[Z_g]$ is equal to the real part of the Gunn diode negative resistance $(-R_g)$ and Z_c is the circuit impedance. The operating frequency occurs when the overall imaginary impedance components cancel out

$$\mathrm{Im}[Z_g] + \mathrm{Im}[Z_c] = 0 \tag{2}$$

A screw type Gunn diode form M/ACOM 49106-111 was used with typical output power levels of over 50 mW. Increasing patch antenna diameter causes an inversely proportional shift in the active antenna oscillation frequency. The Gunn oscillator power output of the active antenna was calculated from the received power using the Friis transmission formula as described in [11], [12], [14]. The measured gain of the passive probe-fed antenna was used to approximate active antenna element's gain. Table II lists active antenna operating frequencies and oscillator power with respect to patch size. The effective isotropic radiated power (EIRP) is also included for comparison with other power combiners.

One could supply DC bias to the patch conductor and then make contact with the diode. Our design biases the diode directly from under the ground plane using a filtering capacitor. This biasing scheme allows proximity coupling to the patch antenna to tune out some of the diode's series inductive component. One can use the method to experimentally tune over a small range of frequencies for a given mode. An electronic method of varying the frequency of operation involves the bias voltage. Varying the bias voltage of the Gunn diode causes a change in the diode junction reactance and a corresponding shift in operating frequency. Table III lists typical Gunn bias voltages vs. operating frequencies and oscillator power for the active antenna. The overall tuning range of the active antenna is 140 MHz. The 3 dB bias tuning range is 107 MHz at 9.09 GHz or 1.2%. The active antenna pattern remains well-behaved with a cross-polarization level of at least 10 dB below the maximum.

The active antenna spectrum is very pure, stable and comparable to waveguide oscillators. The high external quality factor is due to the small cylindrical enclosure surround the inverted stripline antenna. The cylindrical enclosure stabilizes the oscillating frequency and reduces surface mode losses. The

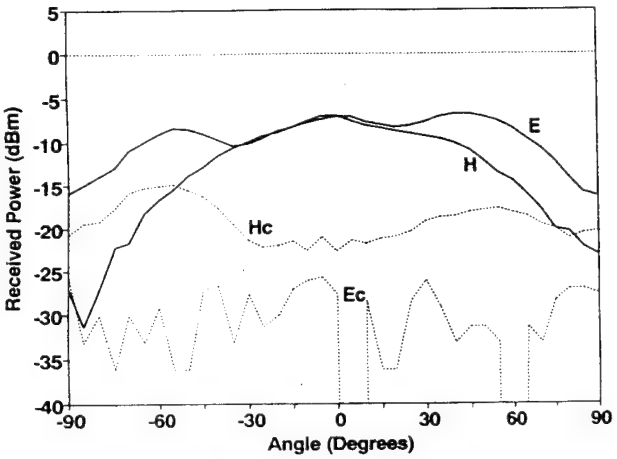

Fig. 5. the active antenna radiation patterns with the Gunn diode located 2 mm off-center. (E, H-co-polarization; E_c, H_c-cross-polarization.)

Gunn diode's vertical proximity to the patch was used to tune over a small frequency range. This mechanical adjustment was useful in ensuring that several antennas would operate at the same bias voltage and within the small locking bandwidth when power combining via mutual coupling.

The Gunn diode's position under the antenna changes the real and imaginary impedance presented to its terminals thereby altering the operating frequency. The Gunn diode oscillates at different radial distances including at the patch center. However, since the active antenna pattern is strongly dependent on diode position, centering diode causes a broadside null to appear with a well-behaved conical beam similar to a vertical monopole. When the diode is off center, the pattern is broadside. The cross polarization level is at least 10 dB below the maximum for a Gunn diode 2 mm off-center. Typical radiation patterns for the active antenna are shown in Fig. 5. The 3 dB beamwidth is 100 and 70 degrees for the E and H-plane, respectively. The cross-pol level is 10 dB below the maximum. This compares favorably with the passive antenna patterns of Fig. 4. Differences in beamwidth and cross-pol levels may be attributed to differences in antenna perturbation between the probe and Gunn diode package.

IV. INJECTION LOCKING

External injection-locking experiments with an HP-83622A synthesized sweeper were performed to determine the locking-

TABLE IV
OPERATING FREQUENCY, OSCILLATOR POWER AND EFFICIENCY OF EACH ANTENNA AND ARRAY

Antenna	1	2	3	4	Square Array*	5	6	7	8	Diamond Array**
Oscillator Frequency (GHz)	9.498	9.499	9.498	9.497	9.511	9.330	9.340	9.330	9.340	9.380
Oscillator Power (mW)	52.63	56.80	59.32	60.14	204	50.55	49.51	56.72	55.55	184
EIRP (mW)	243.4	262.6	274.3	278.1	3773	233.7	228.9	262.3	256.8	3403
[dBm]	[23.9]	[24.2]	[24.4]	[24.4]	[35.8]	[23.7]	[23.6]	[24.2]	[24.1]	[35.3]
Combining Efficiency (%)	—	—	—	—	89.03	—	—	—	—	86.57
DC to RF Efficiency (%)	1.75	1.89	1.98	2.00	1.63	1.69	1.65	1.89	1.85	1.47

*Antennas 1, 2, 3, and 4 are used in the Square Array with 17 mm Spacing.
**Antennas 5,6,7, and 8 are used in the Diamond Array with 17 mm Spacing along the diagonal.

gain and locking-bandwidth of the active antenna. The test measurement set-up is described in [11], [14]. The signal quality shows a noticeable improvement in noise level and spectral purity after injection-lock.

The locking gain ($G_L = P_{\text{output}}/P_{\text{injected}}$) determines the relative power required to externally injection lock the active antenna element. A 10.4 mm patch exhibited a locking gain of 30 dB, a locking bandwidth of 16 MHz at 9.23 GHz. As the injection lock signal power decreases, there is a corresponding decrease in obtainable locking bandwidth. The external Q-factor of the circuit is found using equation given in [23]. The external Q-factor of the active cavity-enclosed inverted stripline antenna was computed at 36. In comparison with previous active antennas of [12] and [14], this external Q-factor is nearly doubled.

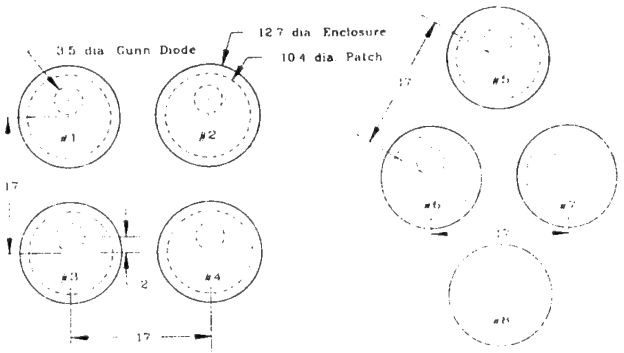

Fig. 6. Array configurations and spacing.

V. POWER COMBINING

The power combining concept uses many low power sources to provide a single coherent, higher power output. To demonstrate spatial power combining via mutual coupling, two four element arrays were constructed.

Eight active inverted stripline antennas were built and tested for the square and diamond array. Since mutual coupling is used for injection-locking, the locking gain level between two of these active antennas would be high with a corresponding narrow locking bandwidth. Mechanical tuning of the diodes ensured that several antennas would operate within the narrow locking bandwidth. This allows the use of a single power supply at a fixed bias voltage for all diodes and successful power combining. Antennas 1, 2, 3 and 4 were used in a four element square array while antennas 5, 6, 7 and 8 were used in a four element diamond array. Table IV lists the operating frequency, oscillator power and efficiency of each antenna and array as well as the EIRP. The square array uses 17 mm spacing between elements. The diamond array spacing between elements is 17 mm along the diagonal. Fig. 6 shows the array configurations, spacing and diode position.

The power combining efficiency (η) is defined by

$$\eta = \frac{P_{\text{combiner}}}{\sum_{N} P_n} \times 100\% \tag{3}$$

- P_n = Power of nth active antenna (Using G_o as the gain of a single passive antenna).
- P_{combiner} = Power of injection-locked, power-combined signal (Use the gain as NG_o for an N element array).
- All oscillator power calculations use the Friis transmission equation [11].

The square array was used to test two element injection-locking and power combining via mutual coupling for E and H-plane elements. The two element H-plane array shows a power combining efficiency of 86.4% while the E-plane array's efficiency was 99.8%. The four element square array exhibited power combining efficiency of 89%. The overall DC to RF efficiency of the four element array is 1.63%. The two element patterns for E and H-plane power combining show nearly 2 to 1 beamwidth sharpening of over a single element. The antenna patterns for the square power combiner

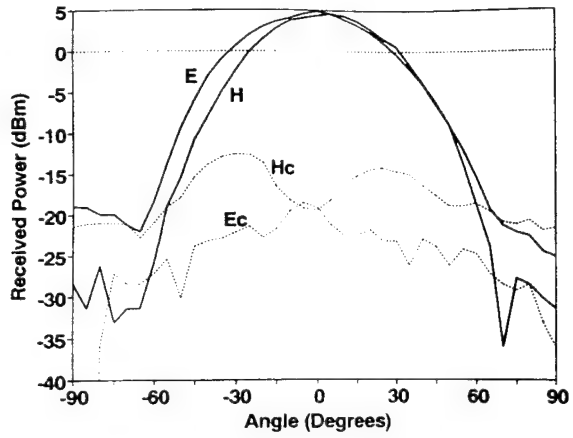

(a)

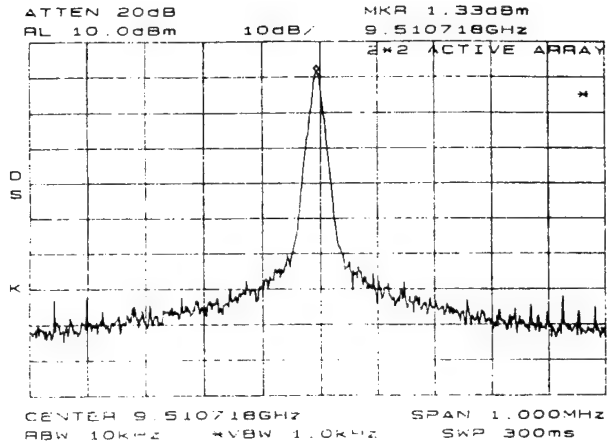

(b)

Fig. 7. The four element square array. (a) Power combiner patterns (E, H-Co-polarization; E_c, H_c-Cross-polarization. (b) Power combiner spectrum.

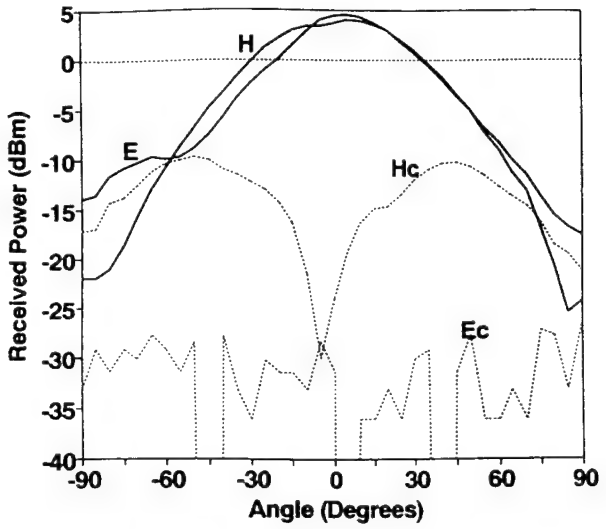

Fig. 8. The four element diamond array power combiner patterns. E, H-Co-polarization; E_c, H_c-Cross-polarization.)

array is shown in Fig. 7(a). The array can be bias tuned from 10.7 to 14 Volts without losing injection lock over a 60 MHz bandwidth from 9.467 to 9.527 GHz. The output power level varied less than 0.8 dB over the bias tuned range. The power combiner spectrum is shown in Fig. 7(b).

The four element diamond array was also tested for injection-locked power combining. The diamond array power combining efficiency is 86.57% with an overall DC to RF conversion efficiency of 1.47%. The array can be bias tuned from 9.5 to 12.2 V without losing injection lock over a 50 MHz bandwidth. The radiation patterns of the diamond array are shown in Fig. 8. The 3 dB beamwidth is similar to that of Fig. 7(a). The cross-polarization level of the square array is 3 dB lower than that of the diamond array.

VI. Beam Steering Without Conventional Phase-Shifters

Active antenna operating frequency depends on the circuit and applied bias voltage. Single-output DC power supplies are usually used to operate an entire array to reduce the overall cost. However, a variable voltage can be used to change individual active antenna operating frequencies. The difference between self-oscillating frequencies of active antennas produces a phase-shift in the injection-locked power combiner. The phase-shift can be used to electronically steer the beam of the active antenna power combiner [24].

Two identical active antennas with different bias voltages oscillate at different frequencies. When the difference between the self oscillating frequencies is within the locking-bandwidth for a given locking-gain, the antennas will injection-lock at a single oscillating frequency for power combining. A row of active antennas can be made to operate at various self-oscillating frequencies using a ramped DC voltage. The elements will injection lock and the power combiner antenna beam will steer off-broadside. The beam steering angle is directly proportional to the difference in self-oscillating frequencies which depends on the applied DC bias voltage.

The square 2×2 power combiner exhibited 15 degrees H-plane beam-steering. For H-plane beam steering, one bias voltage (V_1) is applied to antennas 1 and 3 (see Fig. 6), and another bias voltage (V_2) is applied to antennas 2 and 4. The self-oscillating frequencies of each antenna were adjusted to within 0.02% at 12 V bias. When $V_1 = V_2$ the resultant power combining beam is broadside at 9.511 GHz with 89% combining efficiency. The bias V_1 was then lowered to 10.5 V while maintaining V_2 at 12 V. Similarly, the bias V_2 was adjusted to 11 V while maintaining V_1 at 12 V. the two extremes give a 15 degree H-plane beam steering as shown in Fig. 9. All four elements remain injection-locked throughout the tuning range. As shown, the overall beam remains within 1.2 dB of the maximum at 0 degrees. The cross-polarization level increases slightly over the broadside combiner but remains at least 15 dB below the maximum. E-plane beam-steering can be accomplished by pairing elements 1 with 2 and 3 with 4.

VII. Conclusions

The probe-fed passive cavity enclosed inverted stripline antenna is conformal like other microstrip antennas. Furthermore, the antenna provides an inherent radome for protection and sealing. In an array environment, the enclosure provides

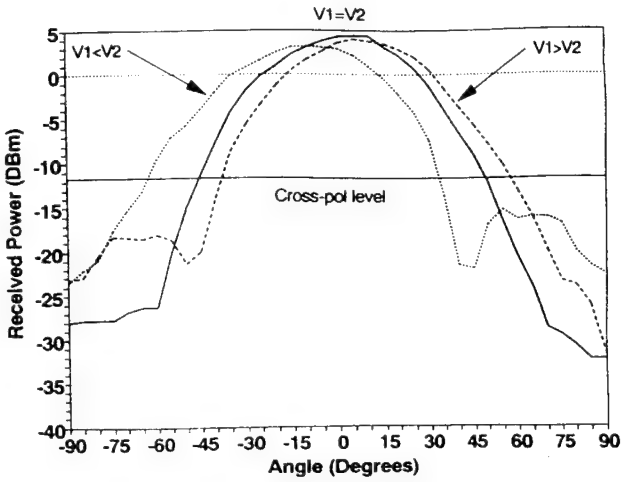

Fig. 9. Beam Steering of active antenna arrays without conventional phase-shifters.

improved isolation between elements. The overall gain is slightly higher than standard patch antennas. However, a large array of passive probe-fed elements may prove laborious without an improved corporate feeding scheme and a single probe input.

Similarly, the active antenna configuration does not require drilling through the circuit substrate or soldering to the patch antenna. The configuration allows easy optimization of frequency, power or antenna performance in a single test fixture. The operating frequency can be tuned mechanically and electronically. The antenna exhibits a purer spectrum and higher stability than current active antennas. Correct choice of the housing and dielectric insert material allows hermetic sealing of active devices below the antenna. The heat sink and enclosure provides enough metal volume for efficient dissipation of heat and improved reliability of active devices. For mm and sub-mm applications, monolithically fabricated inserts can be inserted to a machined metal housing. The design allows easy modular construction and active element replaceability.

The antenna provides a means of developing tile type arrays for reduced size and conformability. The array structure is suitable for open resonators in power combining. An array of active antennas has shown high power combining efficiencies via mutual coupling and the ability to maintain injection-locking with bias tuning for frequency modulated links or radar applications. The combiner arrays exhibit similar locking gain and bandwidth as the single element. External injection-locking provides another means of frequency tuning or modulating the operating frequency as well as improving spectral purity and frequency stability. Beam steering has also been demonstrated to further the capabilities of active antenna power combiners.

ACKNOWLEDGMENT

This investigation was funded partially by the U.S. Army Research Office and the Texas Higher Education Coordinating Board's Advanced Technology Program. The substrate material was provided by the Rogers Corporation. The authors thank Drs. Krys Michalski and Steve Wright for many helpful discussions and suggestions.

REFERENCES

[1] K. Chang and C. Sun, "Millimeter-wave power-combining techniques," *IEEE Trans. Microwave Theory Tech.*, vol. MTT-31, no. 2, pp. 91–107, Feb. 1983.

[2] J. W. Mink, "Quasi-optical power combining of solid-state millimeter-wave sources," *IEEE Trans. Microwave Theory Tech.*, vol. MTT-34, pp. 273–279, Feb. 1986.

[3] J. C. Wiltse and J. W. Mink, "Quasi-optical power combining of solid-state sources," *Microwave J.*, pp. 144–156, Feb. 1992.

[4] H. J. Thomas, D. L. Fudge and G. Morris, "Gunn source integrated with a microstrip patch," *Microwaves and RF*, pp. 87–89, Feb. 1985.

[5] T. O. Perkins, "Active microstrip circular patch antenna," *Microwave J.*, pp. 110–117, Mar. 1987.

[6] K. Chang, K. A. Hummer, and G. Gopalakrishnan, "Active radiating element using FET source integrated with microstrip patch antenna," *Electron. Lett.*, vol. 24, no. 21, pp. 1347–1348, Oct. 13, 1988.

[7] V. F. Fusco, "Series feedback integrated active microstrip antenna synthesis and characterization," *Electron. Lett.*, vol. 28, n0. 1, pp. 89–91, Jan. 2, 1992.

[8] R. A. York, R. M. Martinez, and R. C. Compton, "Hybrid transistor and patch antenna element for array applications," *Electron. Lett.*, vol. 26, pp. 494–495, Mar. 1990.

[9] P. M. Haskings, P. s. hall, and J. S. Dahele, "Active patch antenna element with diode tuning," *Electron. Lett.*, vol. 27, no. 20, pp. 1846–1847, Sept. 26, 1991.

[10] J. A. Navarro, Y. Shu, and K. Chang, "Active endfire antenna elements and power combiners using notch antennas," *IEEE MTT-S Int. Microwave Symp. Dig.*, 1990, Dallas, TX, pp. 793–796.

[11] J. A. Navarro, Y. Shu, and K. Chang, "Broadband electronically tunable planar active radiating elements and spatial power combiners using notch antennas," *IEEE Trans. Microwave Theory Tech.*, vol. MTT-40, no. 2, pp. 323–328, Feb. 1992.

[12] J. A. Navarro and K. Chang, "Broadband electronically tunable planar active radiating elements and spatial power combiners using notch antennas," (Invited Paper) *Microwave J.*, vol. 35, pp. 87–101, Oct. 1992.

[13] S. Young and K. D. Stephan, "Stabilization and power combining of planar microwave oscillators with an open resonator," *IEEE MTT-S Int. Microwave Symp. Dig.*, 1987, pp. 185–188.

[14] K. Chang, K. A. Hummer, and J. L. Klein, "Experiments on injection locking of active antenna elements for active phase arrays and spatial power combiners," *IEEE Trans. Microwave Theory Tech.*, vol. MTT-37, no. 7, pp. 1078–1084, July, 1989.

[15] J. Birkeland and T. Itoh, "Planar FET oscillators using periodic microstrip patch antennas," *IEEE Trans. Microwave Theory Tech.*, vol. MTT-37, no. 8, pp. 1232–1236, Aug. 1989.

[16] Z. B. Popovic, R. M. Weikle II, M. Kim, K. A. Potter, and D. B. Rutledge, "Bar-grid oscillators," *IEEE Trans. Microwave Theory Tech.*, vol. MTT-38, no. 3, pp. 225–230, mar. 1990.

[17] R. A. York and R. C. Compton, "Quasi-optical power combining using mutually synchronized oscillator arrays," *IEEE Trans. Microwave Theory Tech.*, vol. MTT-39, no. 6, pp. 1000–1009, June 1991.

[18] ——, "Dual-device active patch antenna with improved radiation characteristics," *Electron. Lett.*, vol. 28, no. 11, pp. 1019–1021, May 1992.

[19] F. Abboud, J. P. Damiano, and A. Papiernik, "A new model for calculating the input impedance of coax-fed circular microstrip antennas with and without air gaps," *IEEE Trans. Antennas Propagat.*, vol. 38, no. 11, pp. 1882–1885, Nov. 1990.

[20] P. Pramanick and P. Bhartia, "CAD models for millimeter-wave finlines and suspended-substrate microstrip lines,"*IEEE Trans. Microwave Theory Tech.*, vol. MTT-33, no. 12, pp. 1429–1435, Dec. 1985.

[21] J. A. Navarro, K. Chang, J. Tolleson, S. Sanzgiri, and R. Q. Lee, "A 29.3 GHz cavity enclosed aperture-coupled circular patch antenna for microwave circuit integration," *IEEE Microwave Guided Wave Lett.*, vol. 1, no. 7, pp. 170–171, July 1991.

[22] S. Sanzgiri and J. Tolleson, "*Ka* band sub-array technology demonstration program," *Texas Instruments Design Review*, Aug. 7, 1991.

[23] R. Alder, "A study of locking phenomena in oscillators," *Proc. IRE*, vol. 34, pp. 351–357, June 1946.

[24] J. A. Navarro and K. Chang, "Beam steering of active antenna arrays," *Electron. Lett.*, vol. 29, no. 3, pp. 302–304, February 4, 1993.

IEEE TRANSACTIONS ON MICROWAVE THEORY AND TECHNIQUES, VOL. 41, NO. 10, OCTOBER 1993

Slot-Fed Higher Order Mode Fabry–Perot Filters

James McCleary, *Student Member, IEEE,* Ming-yi Li, and Kai Chang, *Fellow, IEEE*

Abstract—**Low loss bandpass filters consisting of Fabry–Perot resonators excited by waveguide fed slots coupling to higher order resonator modes are demonstrated. For close reflector spacings, the waveguide couples efficiently through the slots to the TEM_{400} and TEM_{300} modes. The characteristics of both rectangular and circular waveguide feeds with various slot lengths and widths are presented. At X-band the filters have unloaded Q values which range from 1000 to 7000 with insertion losses less than 1 dB. The filters which have the rectangular waveguide feeds are mechanically tunable over a 20% bandwidth.**

I. Introduction

THIS PAPER presents results on efficient coupling to the higher order modes of a Fabry–Perot resonator through slots fed by waveguide. The problem of coupling to a mode of a Fabry–Perot resonator is essentially that of coupling to a propagating beam within the resonator. Most previous work in this area has been in coupling to a fundamental Gaussian beam. A good way to couple from waveguide to a Gaussian beam is through a horn, the most efficient being a corrugated horn [1]. Once launched from a horn, a Gaussian beam can be coupled into a resonator through metal grids or dielectric plates for such applications as diplexing and filtering [2]–[6].

A popular coupling method used in the characterization of dielectrics is from waveguide through small holes [7], [8]. This method of coupling to a fundamental mode is not very efficient, but the objective of this application is not to achieve good coupling, but rather a high Q [9]. A single element in general does not couple well to a Gaussian beam. Mink's analysis show that an array of elements is needed to efficiently couple to a fundamental mode of a Fabry–Perot resonator [10].

The literature on the applications of Fabry–Perot resonators to power combining and oscillator stabilization contains various examples of fundamental-mode coupling methods. A few include dielectric tapers, slots, patches, patch-illuminated slots, circular-apertures, and waveguide apertures [11]–[16].

Kuraev *et al.*, have conducted theoretical and experimental analyses of coupling transitions consisting of tapered waveguide sections [17], [18]. Cam *et. al.*, have applied the boundary element method to solve for the current distribution on a reflector of a resonator disturbed by a circular aperture [19].

In [20], the authors reported a low-loss filter consisting of a plano-concave resonator fed by rectangular waveguide through slots. Low loss occurred by coupling to a fundamental mode near the resonant frequency of the slots. In this paper, we report improved filter performance by slot-coupling to higher order modes in concave resonators. The results include mechanically tunable X-band filters with insertion losses less than 1 dB and unloaded Q values ranging from 1000 to 7000. Although our experiments were conducted at X-band, the filters should have many applications at millimeter-wave and submillimeter-wave frequencies where conventional filters have higher losses and lower values of Q.

The rest of the paper is organized as follows. First is a brief review of resonator mode theory. Then follows a description of experimental setups and the results of experiments using rectangular and circular waveguide feeds.

Manuscript received August 18, 1992. This work was supported in part by the Army Research Office and the Department of Defense through a National Defense Science and Engineering Graduate Fellowship.

The authors are with the Department of Electrical Engineering, Texas A&M University, College Station, Texas 77843-3128.

IEEE Log Number 9211928.

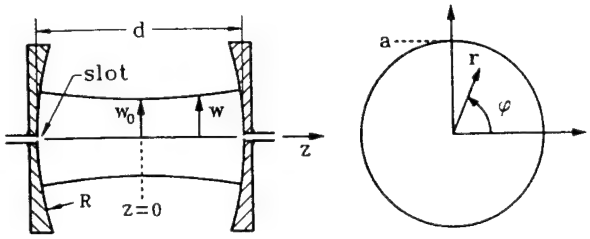

Fig. 1. Concave-concave resonator fed by waveguide through slots. Also shown is the coordinate system. The reflectors have radii of curvature R, have radii a, and are separated by an axial distance d.

II. Resonator Modes

The experiments described in this paper deal with Fabry–Perot resonators configured like the one shown in Fig. 1. This resonator consists of two circular concave reflectors separated by an axial distance d. The reflectors have equal radii of curvature R. Power couples into and out of the resonator through waveguide-fed slots at the center of each reflector.

The resonant frequencies of the resonator in cylindrical coordinates are given by the well known formula [21]

$$f_{plq} = \frac{c}{2d}\left[(q+1) + \frac{1}{\pi}(2p+l+1)\arccos(1-d/R)\right]. \tag{1}$$

The plq are mode numbers. The resonant fields are approximately TEM, and the modes are denoted by TEM_{plq}. Fundamental modes have $p = l = 0$ and have radially symmetric field distributions which are approximately Gaussian. The quantity $(q+1)$ is the number of half-wavelengths of the standing wave set up between the reflectors. The standing wave is formed by the Gaussian beam which propagates back and forth between the reflectors. Illustrated in Fig. 1 is the beam radius w which is the contour where the amplitude of the beam is $1/e$ of its value on the axis. At the center of the

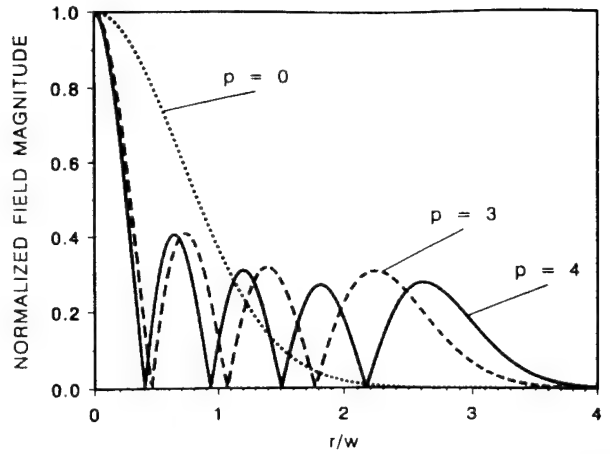

Fig. 2. Ideal transverse field distributions of the TEM_{00l} ($p = 0$), TEM_{30l} ($p = 3$), and TEM_{40l} ($p = 4$) modes.

resonator ($z = 0$ in Fig. 1), the beam has a minimum radius w_0 called the beam waist given by [21]

$$w_0^2 = \frac{\lambda}{2\pi}\sqrt{d(2R-d)}\,. \tag{2}$$

The beam radius at any other location in the resonator is expressed in terms of the waist as [21]

$$w^2(z) = w_0^2\left[1+\left(\frac{\lambda z}{\pi w_0^2}\right)^2\right]. \tag{3}$$

In particular, the beam incident on a reflector (at $z = \pm d/2$) has radius w_r given by

$$w_r^2 = \frac{\lambda R}{\pi}\sqrt{\frac{d}{2R-d}}\,. \tag{4}$$

The mode numbers p and l describe higher order modes which have nulls along contours of constant r and ϕ, respectively. The higher order modes for which $l \neq 0$ have a null along the resonator axis ($r = 0$). Since the slots in Fig. 1 are along the axis, coupling to these modes is weak [8].

The transverse fields of the modes for which $l = 0$ but $p \neq 0$ have radially symmetric distributions given approximately by the product of Gaussian and Laguerre functions. The magnitudes of these distributions are given by [21]

$$u(r) = \frac{w_0}{w}\exp\left(-\frac{r^2}{w^2}\right)\left|L_p\left(2\,\frac{r^2}{w^2}\right)\right|, \tag{5}$$

where L_p is a Laguerre polynomial. An expression for the Laguerre polynomials is [22]

$$L_p(x) = \sum_{m=0}^{p}(-1)^m\,\frac{p!}{(p-m)!\,m!\,m!}\,x^m\,. \tag{6}$$

Of particular interest in this paper are the TEM_{30l} and TEM_{40l} modes. Fig. 2 shows the transverse fields for these modes as well as the fundamental mode ($p = 0$). They are plotted as functions of the radial coordinate r normalized by the beam radius w.

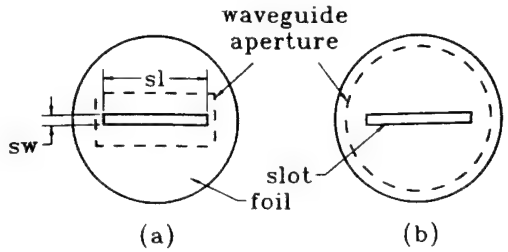

Fig. 3. Dimensions and positions of the slots for (a) the rectangular waveguide feed and (b) the circular waveguide feed. The slots have width sw and length sl.

III. Measurement Setups for Slot-Fed Filters

Measurements of the resonator included testing of both rectangular and circular waveguide feeds at X-band frequencies. Fig. 1 shows the general experimental setup for both feeds. The rectangular waveguide feed is standard 0.9" × 0.4" (22.9 mm × 10.2 mm) X-band waveguide. For the measurements with the circular waveguide feed, transitions from rectangular to circular waveguide were used. The diameter of the circular waveguide output of each transition is 27.79 mm. The transition contains mode filters which allow single dominant mode operation with good performance from 10.5 GHz to 11.7 GHz. Each feed is mounted flush to a reflector. The other end of each feed is connected by coax to an HP8510 network analyzer.

The reflectors are two aluminum discs which have 9" (22.9 cm) diameters and 40" (101.6 cm) radii of curvature. A plug of 3" (7.62 cm) diameter is removable from the center of each reflector. The plugs allow different feed structures to be tested without manufacturing entirely different reflectors. Cut through the center of each plug is a waveguide aperture which matches the dimensions of the waveguide feed. The reflectors are mounted on an optical rail which allows measurement of distance accurate to 0.1 mm.

Coupling from the waveguides to the resonator is through slots cut in copper or brass foil. Fig. 3 shows the general dimensions of the slots. The slots are sw wide and sl long. Their orientation is orthogonal to the direction of the dominant mode electric field in each guide. Tape fixes the slots over the waveguide apertures.

TRL calibrations were made to set the reference planes for S-parameter measurements at the ends of the waveguide feeds. This means that unloaded Q measurements were not of the resonator by itself, but of the resonator loaded by the slots.

IV. Rectangular Waveguide Slot-Fed Filters

The measurements of rectangular waveguide slot-fed filters include two slot sizes: 0.5 mm × 23 mm and 0.5 mm × 20 mm. The 23 mm long slot extends across the width of the waveguide. Other slots with larger widths were also tested, but only the 0.5 mm wide slots provided consistently good isolation (≥ 20 dB) between adjacent modes across the 8–12 GHz measurement band. We use isolation to refer loosely to the difference between the strength of a peak of a resonance and the floor between it and an adjacent resonance. For example, consider Fig. 4 which shows an S_{21} measurement

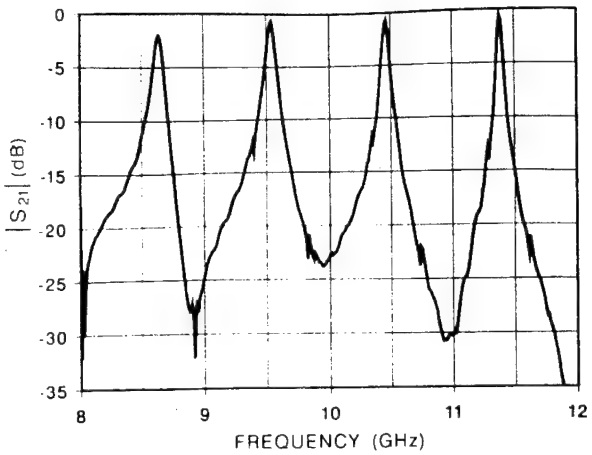

Fig. 4. S_{21} measurement of the rectangular waveguide slot-fed filter for a reflector spacing $d = 20.9$ mm. The modes from left to right are the TEM_{100}, TEM_{200}, TEM_{300}, and TEM_{400} modes.

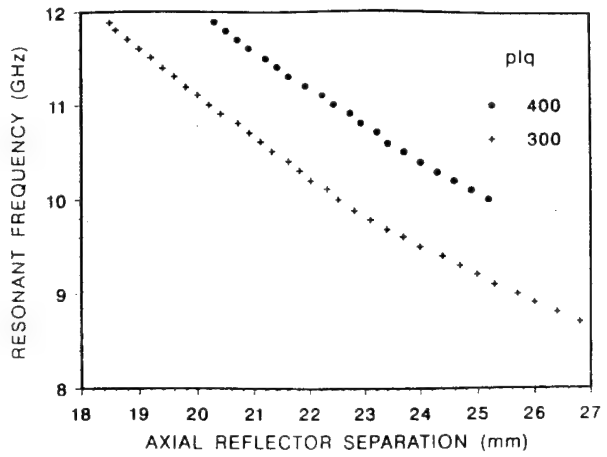

Fig. 5. Measured resonant frequencies versus reflector separation for the rectangular waveguide feed with the 0.5 mm × 23 mm slots.

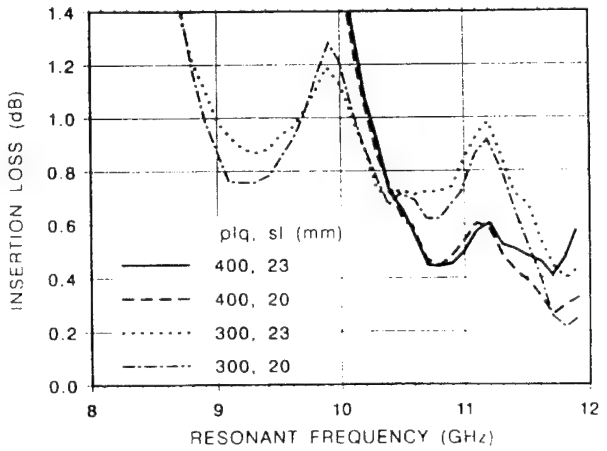

Fig. 6. Insertion loss versus resonant frequency for the rectangular waveguide slot-fed filters.

of the resonator with the 23 mm long slots for a reflector spacing of $d = 20.9$ mm. The modes from left to right are the TEM_{100}, TEM_{200}, TEM_{300}, and TEM_{400} modes. The isolation between the TEM_{300} and TEM_{400} modes is about 30 dB, but the isolation between the TEM_{200} and TEM_{300} modes is less than 25 dB.

All the modes in Fig. 4, including the TEM_{000} fundamental not shown in the figure, exhibited some very low loss behavior (< 1 dB) over the 8–12 GHz band. The TEM_{300} and TEM_{400} modes, however, more consistently had low loss, and they had better isolation from surrounding modes. The following results are for these two modes. Note that these results are only for the TEM_{300} and TEM_{400} modes and not the TEM_{30q} and TEM_{40q} modes in general. The diffraction losses of these modes for $q > 0$ were large.

Fig. 5 shows measured resonant frequencies as a function of reflector separation for the TEM_{300} and TEM_{400} modes with the 23 m long slots. The curves show the mechanical tunability of the filters. The case for the 20 mm long slots has a plot nearly identical to this one. For both cases, the measured frequencies are consistently 2.5–3.5% greater than the theoretical frequencies predicted by (1). One reason for this difference could be strong coupling from the waveguides to the resonator. Another possible explanation is the breakdown of Gaussian beam theory for reflector separations less than one wavelength.

Fig. 6 plots insertion loss against resonant frequency for the four combinations of modes and slot lengths: $p = 4$, $sl = 23$ mm; $p = 4$, $sl = 20$ mm; $p = 3$, $sl = 23$ mm; and $p = 3$, $sl = 20$ mm. Note that each point in the graph represents a different reflector separation, just as in Fig. 5. The TEM_{400} mode has less than 1 dB loss above 10.2 GHz. The TEM_{300} mode has less than 1 dB loss above 9 GHz except for a band between 9.6 and 10.1 GHz. The filters are mechanically tunable over a 20% bandwidth with less than 1 dB insertion loss. From these measurements, the loss does not seem to significantly depend on the slot length. The VSWR for these measurements never exceeded 1.3. The insertion loss is then due mostly to ohmic loses, diffraction, and radiation from the slots which does not couple to the resonator mode.

Fig. 2 can provide a qualitative sense of how diffraction loss affects the insertion loss of the filters. A point at $r/w = a/w_r$ (where a is the reflector radius, and w_r is the beam radius at a reflector given by (4)) represents the incident field at the edge of a reflector. Any field before this point is contained within the resonator; any field above this point is lost to diffraction. Table I shows four of these points which correspond to measurements with the 23 mm long slots. In each row of the table, the first column shows the mode of the measurement (TEM_{400} or TEM_{300}), and the second and third columns contain a measured frequency-reflector separation ($f - d$) data pair. The fourth column shows the reflector edge point, a/w_r, calculated from (4) using the measured f and d. The fifth column shows the measured insertion loss. The first and second rows of the table show the edge points for the two modes at about 11.9 GHz. Both of the fields which correspond to these points in Fig. 2 have almost converged to zero before these points; the diffraction loss can be expected to be small. The third and fourth rows are measurements of each mode at larger reflector separations where the insertion loss

TABLE I
REFLECTOR EDGE POINTS (a/w_r) FOR THE RECTANGULAR WAVEGUIDE SLOT-FED FILTERS ($sl = 23$ mm)

plq	f (GHz)	d (mm)	a/w_r	L (dB
400	11.8895	20.3	4.0	0.58
300	11.8845	18.5	4.1	0.43
400	10.1085	24.9	3.5	1.32
300	8.8025	26.4	3.2	1.22

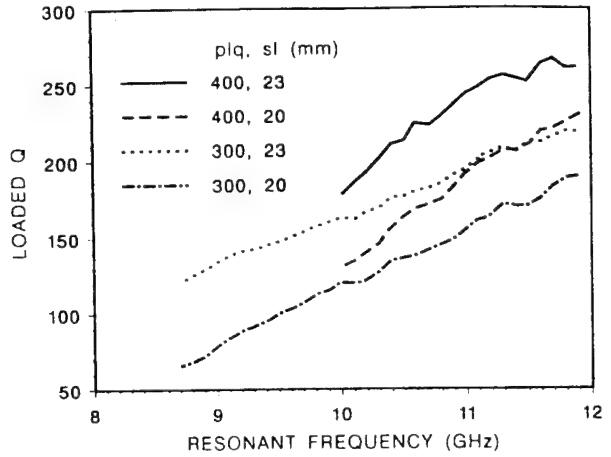

Fig. 7. Q_l versus resonant frequency for the rectangular waveguide slot-fed filters.

exceeds 1 dB. At greater separation (corresponding to lower frequencies) the insertion loss increases rapidly. The fields which correspond to these points in Fig. 2 are just beginning to extend beyond the edges of the reflectors.

This discussion of diffraction loss is very heuristic. The actual fields in the filters are probably not exactly like the ideal fields depicted in Fig. 2. The most that can be said is that diffraction loss limits the tuning bandwidths of the filters. At higher frequencies, the reflectors could easily be made larger in terms of wavelength to improve the performance of the filters.

Fig. 7 shows the loaded $Q(Q_l = f_o/\Delta f_{3\text{dB}})$ versus resonant frequency for the four mode and slot combinations. Although Fig. 6 shows no significant dependence of loss on slot length, Fig. 7 shows a definite dependence of Q_l on slot length. The longer slot has a higher loaded Q (narrower 3 dB bandwidth) than the shorter slot for the same mode and frequency. In addition, the TEM_{400} mode has a higher Q_l than the TEM_{300} mode for either slot or the measured frequencies.

The lower loaded Q of the modes for the 20 mm long slot cases means that the isolation between the modes is less for them also. The isolation between the TEM_{400} and the TEM_{300} modes is always greater than 25 dB for the longer slot but only greater than 20 dB for the shorter slot. Similarly, the isolation between the TEM_{300} and the TEM_{200} modes is greater than 20 dB for the longer slot (for the measured frequencies) but less than 20 dB for the shorter slot for frequencies below 9.3 GHz.

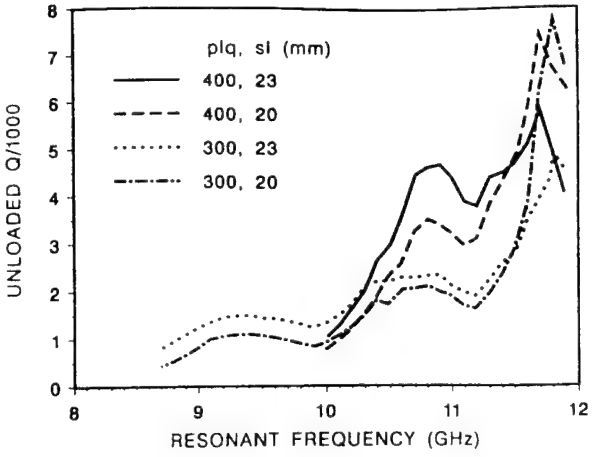

Fig. 8. Q_u versus resonant frequency for the rectangular waveguide slot-fed resonators loaded by the slots.

Fig. 8 shows the unloaded Q as a function of frequency for the four cases. The unloaded Q is given by [23]

$$Q_u = \frac{Q_l}{1 - 10^{-L/20}}, \tag{7}$$

where L is the insertion loss in dB. The relationships between the cases are similar to those for Q_l; however, Q_u does not show the fairly linear dependence on frequency that Q_l shows in Fig. 7. Q_u has a more erratic dependence due to the oscillating frequency response of the loss shown in Fig. 6. The unloaded Q values of the TEM_{300} and TEM_{400} modes for the 20 mm long slot exceed 7000 above 11.5 GHz. Note that Q_u is not for the resonator itself, but of the resonator loaded by the slots.

V. CIRCULAR WAVEGUIDE SLOT-FED FILTERS

The rectangular to circular waveguide transitions limited the circular waveguide slot-fed filter measurements from 10.5 to 11.7 GHz, a much narrower band compared to the rectangular waveguide feed case. These measurements also used slots with different widths, rather than lengths. Three slots were tested; all had lengths of 20 mm and widths of 1, 2, and 3 mm, respectively.

As with the rectangular waveguide slot-fed filters, the TEM_{300} and TEM_{400} modes showed better performance in terms of low loss than any other modes. S-parameter measurements for the six combinations of mode and slot width were made at increments of 100 MHz across the 10.5–11.7 GHz band. As with the rectangular waveguide feed, the measured frequencies were an average of about 3% higher than the theoretical frequencies given by (1).

Figs. 9 and 10 show measurements of insertion loss as functions of resonant frequency for the TEM_{400} and TEM_{300} modes, respectively. Each graph contains measurements for each of the three slot widths. From Fig. 9, the TEM_{400} modes are mechanically tunable with less than 0.8 dB loss from 10..6 to 11.6 GHz. Fig. 11 superimposes the S_{21} measurements of the TEM_{400} mode with the 1 mm wide slots for seven different reflector spacings. Similarly, Fig. 10 shows that the loss for the TEM_{300} mode is less than 1 dB except from about 11.1 to

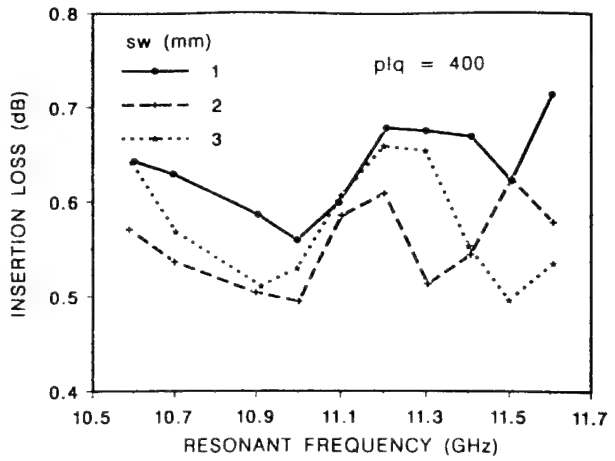

Fig. 9. Insertion loss versus resonant frequency for the circular waveguide slot-fed filters for the TEM_{400} mode.

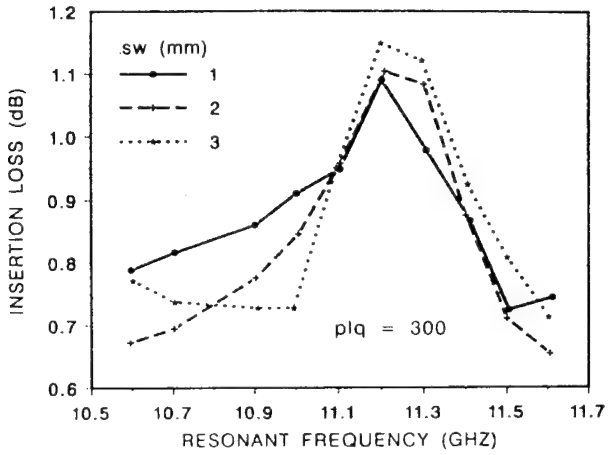

Fig. 10. Insertion loss versus resonant frequency for the circular waveguide slot-fed filters for the TEM_{300} mode.

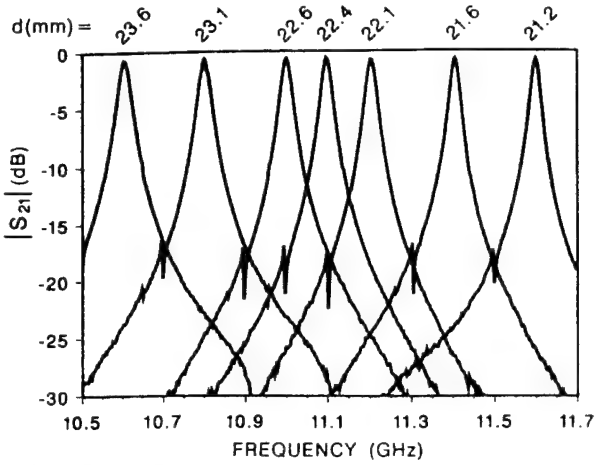

Fig. 11. S_{21} measurements of the circular waveguide slot-fed filter for the TEM_{400} mode with the 1 mm × 20 mm slots. The measurements are for 7 different reflector separations and are superimposed on each other.

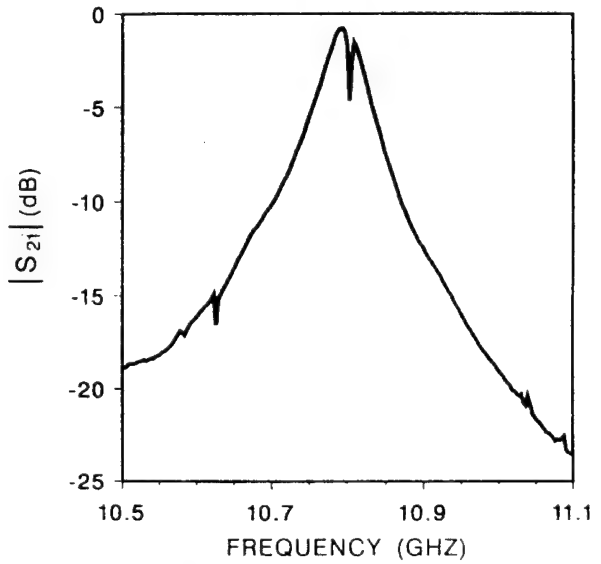

Fig. 12. S_{21} measurement of the circular waveguide slot-fed filter showing distortion for the TEM_{300} mode at 10.8 GHz. The measurement was taken with the 2 m × 20 mm slots and d = 20.8 mm.

11.4 GHz. The shapes of the loss curves in Figs. 9 and 10 are similar to the loss curves over the same frequencies in Fig. 6 for the rectangular waveguide case. Also as with the slot length of the rectangular waveguide feed, no direct correlation can be made about the effect of slot width on loss from the data in these figures. One obvious difference between the two different feeds, however, is that the insertion loss of the TEM_{300} mode around 11.2 GHz for the filters with the circular waveguide feed is greater than 1 dB but less than 1 dB for the filters with the rectangular waveguide feed.

The statement that the TEM_{400} mode is tunable with low loss from 10.6 to 11.6 GHz is not entirely true. From about 10.78 to 10.81 GHz, the modes distort, as shown in Fig. 12 for the TEM_{300} mode with the 2 m wide slots. This phenomenon occurred for both modes for all slot widths, but it did not occur for the rectangular waveguide feeds. All measurements in this section are missing a data point at 10.8 GHz due to this distortion.

The loaded Q values of the circular waveguide slot-fed filters have a linear behavior similar to the rectangular waveguide slot-fed filters. Table II shows Q_l for the circular waveguide case by listing the minimum Q_l at 10.6 GHz and the maximum Q_l at 11.6 GHz for each combination of mode and slot width. The loaded Q decreases with increasing slot width, and for a given slot size, the TEM_{400} mode has a higher Q_l than the TEM_{300} at the same frequency. Both the 1 mm and 2 mm slots for both modes have a higher Q_l than any of the measurements over the same frequency range for the rectangular waveguide case shown in Fig. 8. This means that the circular waveguide slot-fed filters generally have better isolation between adjacent modes than the rectangular waveguide ones. The isolation is typically at least 30 dB for the TEM_{400} mode and at least 25 dB for the TEM_{300} mode for all the slot widths. Figures 13 and 14 show the unloaded Q-factors for the resonator loaded by the slots. The 1 mm wide slot cases for both modes have higher Q_u values than the corresponding cases for the rectangular waveguide shown in Fig. 8.

For both the circular and rectangular waveguide feeds, the TEM_{400} and TEM_{300} modes have less loss than the

TABLE II
LOADED Q VALUES FOR THE CIRCULAR WAVEGUIDE SLOT-FED FILTERS

	$plq = 400$		$plq = 300$	
sw (mm)	Q_l (10.6 GHz)	Q_l (11.6 GHz)	Q_l (10.6 GHz)	Q_l (11.6 GHz)
1	335	452	272	398
2	209	307	183	250
3	152	220	135	194

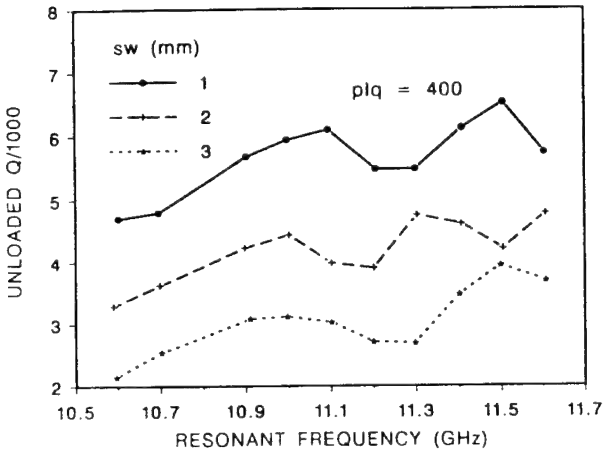

Fig. 13. Q_u versus resonant frequency for the circular waveguide slot-fed resonators loaded by the slots for the TEM_{400} mode.

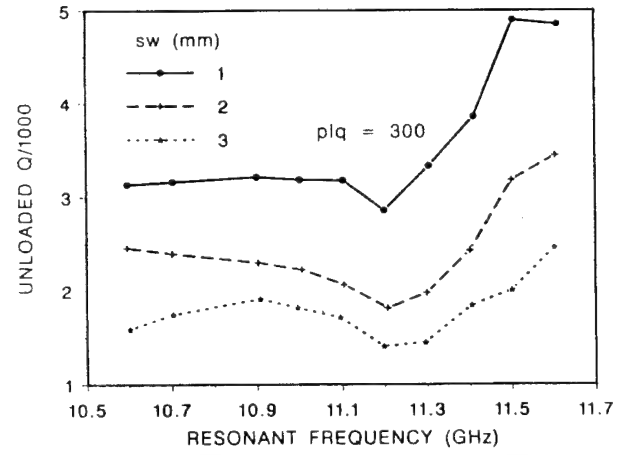

Fig. 14. Q_u versus resonant frequency for the circular waveguide slot-fed resonators loaded by the slots for the TEM_{300} mode.

fundamental TEM_{000} and TEM_{001} modes. The reason for this does not appear to be from diffraction losses because the fields of the fundamental modes are more concentrated around the resonator axis. The higher order resonator modes seem to couple better to the waveguide modes. Fig. 2 shows that the width of the main field distribution of the higher order modes is narrower than the distribution of the fundamental mode. The narrower lobe of a higher order mode may present a better "match" to the waveguide fields than the broader distribution of the fundamental.

VI. CONCLUSIONS

We have demonstrated X-band Fabry–Perot filters which use slots to efficiently couple dominant waveguide modes to the TEM_{400} and TEM_{300} of the resonators. Various slot sizes can be used with both rectangular and circular waveguide feeds to design filters that have unloaded Q values ranging from 1000 to 7000 and insertion losses less than 1 dB. Additional analysis is required to predict the resonant frequencies of the filters as the traditional analytical formula does not predict them accurately enough.

REFERENCES

[1] P. F. Goldsmith, T. Itoh, and K. D. Stephan, "Quasi-optical techniques," in *Handbook of Microwave and Optical Components*, K. Chang, Ed., vol. 1, New York: Wiley, 1981, pp. 344–363.
[2] J. J. Gustuncic, "A quasi-optical receiver design," in *IEEE MTT-S Int. Microwave Symp. Dig.*, pp. 9–101, 1977.
[3] J. A. Arnaud, A. A. M. Saleh, and J. T. Ruscio, "Walk-off effects in Fabry–Perot diplexers," *IEEE Trans. Microwave Theory Tech.*, vol. MTT-22, no. 5, pp. 486–493, May 1974.
[4] H. P. Pickett and A. E. T. Chiou, "Folded Fabry–Perot quasi-optical ring resonator diplexer: theory and experiment," *IEEE Trans. Microwave Theory Tech.*, vol. MTT-31, no. 5, pp. 373–380, May 1983.
[5] P. G. Wannier, J. A. Arnaud, F. A. Pelow, and A. A. M. Saleh, "Quasioptical band-refection filter at 100 GHz," *Rev. Sci. Instr.*, vol. 47, pp. 55–58, 1976.
[6] N. Nakajima and R. Watanbe, "A quasi-optical circuit technology for short-millimeter-wavelength multiplexers," *IEEE Trans. Microwave Theory Tech.*, vol. MTT-29, no. 9, pp. 897–905, Sept. 1981.
[7] A. L. Cullen, "Millimeter-wave open resonator techniques," *Infrared and Millimeter Waves*, Academic Press, vol. 10, ch. 4, pp. 233–281, 1983.
[8] R. G. Jones, "Precise dielectric measurements at 35 GHz using an open resonator," *Proc. Inst. Elec. Eng.*, vol. 123, no. 4, pp. 285–290, Apr. 1976.
[9] A. L. Cullen and P. K. Yu, "The accurate measurement of permittivity by means of an open resonator," *Proc. R. Soc. Lond.*, Series A, vol. 325, pp. 493–509, 1971.
[10] J. W. Mink, "Quasi-optical power-combining of solid-state millimeter-wave sources," *IEEE Trans. Microwave Theory Tech.*, vol. MTT-34, no. 2, pp. 273–279, Feb. 1986.
[11] L. Wandinger and V. Nalbandian, "Millimeter-wave power combining using quasi-optical techniques," *IEEE Trans. Microwave Theory Tech.*, vol. MTT-31, no. 2, pp. 189–193, Feb. 1983.
[12] J. E. Ge, S. F. Li, and Y. Y. Chen, "Millimetre wave quasioptical power combiner," *Electron. Lett.*, vol. 27, no. 10, pp. 880–882, May 1991.
[13] S. Young and K. D. Stephan, "Stabilization and power combining of planar microwave oscillators with an open resonator," in *IEEE MTT-S Int. Microwave Symp. Dig.*, pp. 185–188, 1987.
[14] P. G. Payne and J. Potter, "Efficient power transfer through small apertures," *Electron. Lett.*, vol. 26, no. 25, pp. 2070–2073, Dec. 1990.
[15] E. R. Brown, C. D. Parker, K. M. Molvar, and K. D. Stephan, "A quasioptically stabilized resonant-tunneling-diode oscillator for the millimeter- and submillimeter-wave regions," *IEEE Trans. Microwave Theory Tech.*, vol. MTT-40, no. 5, pp. 846–850, May 1992.
[16] M. Nakayama, M. Heide, T. Tanaka, and K. Mizuno, "Millimeter and submillimeter wave quasi-optical oscillator with multi-elements," in *IEEE MTT-S Int. Microwave Symp. Dig.*, pp. 1209–1212, 1990.
[17] A. A. Kuraev, M. P. Natarov, V. N. Rodionova, V. N. Skresanov, A. Y. Slepyan, and G. Y. Slepyan, "Wide-band matching of quasi-optical resonator with single-molded rectangular waveguide," *Proc. 20th European Microwave Conf.*, Budapest, 1990, supplement A4.5.
[18] V. N. Radionova, Y. A. Slepyan, and G. Y. Slepyan, "Oliner models for quasioptical resonator to rectangular waveguide coupling elements," *Electron. Lett.*, vol. 27, no. 16, pp. 1427–1428, Aug. 1991.
[19] H. Cam, S. Toutain, P. Gelin, and G. Landrac, "Study of a Fabry–Perot cavity in the microwave frequency range by the boundary element method," *IEEE Trans. Microwave Theory Tech.*, vol. 40, no. 2, pp. 298–304, Feb. 1992.
[20] J. C. McCleary and K. Chang, "Low-loss quasi-optical open resonator filters," in *IEEE MTT-S Int. Microwave Symp. Dig.*, pp. 313–316, 1991.
[21] H. Kogelnik and T. Li, "Laser beams and resonators," *Proc. IEEE*, vol. 3, no. 10, pp. 1312–1329, Oct. 1966.

Novel Active FET Circular Patch Antenna Arrays for Quasi-Optical Power Combining

Xiao-Dong Wu and Kai Chang, *Fellow, IEEE*

Abstract—**This paper discusses two-dimensional planar arrays of weakly coupled active circular patch antennas suitable for quasi-optical power combiners. A novel radiating element that has low cross-polarization is described. A two-dimensional array analysis was developed to address radiation pattern and phase problems. Equivalent isotropic radiated power levels of 1.5 W for a two by two FET array and 3.8 W for a two by four FET array have been obtained at *X*-band.**

I. Introduction

THE advent of solid-state devices made practical medium-power microwave oscillators that use power combining techniques [1]. Solid-state sources have smaller size and use less DC power than tube devices. In the millimeter-wave range, conventional power combining techniques have serious limitations due to size and moding problems. A quasi-optical spatial power combining method to solve this problem was suggested in [2]. This technique relies on arrays of weakly coupled injection locking radiating elements. Individual radiating elements can produce high output power because the power combining occurs in free space.

Active radiating elements have many different structures. Microstrip radiating elements using both Gunn diodes and FET devices have been reported [3]–[9]. The low efficiency of Gunn diodes would be a major disadvantage in many applications. FET devices have much higher efficiency and better noise properties, and the FET is better suitable for monolithic planar circuit integration. Several different FET active patch antennas have appeared in the literature. One circuit uses the patch as a feedback resonator and as a radiator [9]. Another circuit uses a gap between the gate and drain to establish feedback with the source leads grounded through the substrate [7]. The patch antenna and oscillator circuit can be separated into different planes [5], [8]. The patch antenna is simple to fabricate, can easily accommodate devices, has high antenna efficiency compared to a grid, and is a resonant stabilization element in the oscillator circuit. However, active patch antennas with the device integrated directly on the patch have high cross-polarization [7].

Dual-devices can improve the cross-polarization level of active patches. York and Compton reported with improved radiation characteristics using two Gunn diodes mounted inside a single patch [10]. The radiation characteristics improve because the actual current distribution on the dual-device patch is different from that on a single-device path. A single device patch that does not have a perfectly placed feed can generate higher order current modes that are mostly responsible for the high cross-polarization. The dual-device patch does not as easily excite the current that generates the cross-polarization field [11].

This paper reports the design and performance of a novel active antenna with a FET integrated directly on two circular patches to achieve low cross-polarization levels. The reason for the lower cross-polarization is that the misplacement of the feed for the rectangular patch can generate higher order modes that cause high cross-polarization. Misplacement of an edge feed for the circular patch still only excites the dominant TE_{11} mode. The circuit is easier to be injection locked than the dual-FET rectangular patch. The circuit forms an element for spatial or quasi-optical power combiners. These active antennas were successfully combined to form a two-element linear array, a four-element linear array, a two by two array, and a two by four array. Injection locking through mutual coupling was accomplished. The circuit is suitable for monolithic implementation because the new structure is completely planar and requires no holes through the substrate for biasing.

II. Analysis of a Weak Coupling Two-Dimensional Active Antenna Array

Making an active array to work properly requires injection locking. Injection locking refers to synchronizing a free running oscillator to a weak injection signal at a frequency close to the operating frequency of the oscillator. The basic phenomenon of injection locking has strong historical roots [12], [13]. Recently, analyses of injection locking active antenna arrays have been reported [7], [14], [15]. A modified form of Adler's equation that introducing a coupling coefficient for multiple devices was presented [7]. A simple chain of four similar oscillators was analyzed based on the theory. The results indicated that the elements should be placed in multiples of one wavelength for a stable, in-phase mode.

This paper extends the analysis to a two-dimensional array. For two-dimensional mutually synchronized arrays, let the coupling coefficient between elements mn and ij be written as $C_{mn,ij} = C_{mn,ij}\exp(-j\Phi_{mn,ij})$, where $C_{mn,ij} \ll 1$. A general form of the Adler's equation for the ij-th oscillator

Manuscript received December 14, 1992; revised July 13, 1993. This work was supported in part by the U.S. Army Research Office and in part by the State of Texas Higher Education Coordinating Board's Advanced Technology Program.

The authors are with the Department of Electrical Engineering, Texas A&M University, College Station, Texas 77843-3128.

IEEE Log Number 9216817.

can be obtained in a complex form as

$$S = S_{ij}\left[1 - \sum_{\substack{m=1\\ m\neq i}}^{M}\sum_{\substack{n=1\\ n\neq j}}^{N}\frac{1}{j4Q_{ij}A_{ij}^2}\right.$$

simultaneously

$$\left.(A_{mn}C_{ij,mn}A_{ij}^* - A_{mn}^*C_{ij,mn}^*A_{ij})\right]$$

$$i = 1, 2, \cdots, M;\ j = 1, 2, \cdots, N; \tag{1}$$

where $A_{ij} = A_{ij}\exp(-j\varphi_{ij})$; A_{ij} =free running amplitude of the ij-th oscillator; φ_{ij} =free running phase of the ij-th oscillator; Q_{ij} =external Q of the ij-th oscillator circuit; $S_{ij} = j\omega_{ij}$, free running complex frequency of the ij-th oscillator; $S = j\omega$, complex frequency of an injection locked array; * denotes complex conjugate.

Some simple results can be derived from (1). A modified form of (1) suitable for a one dimensional array is

$$S = S_i\left[1 - \sum_{\substack{m=1\\ m\neq i}}^{M}\frac{1}{j4Q_iA_i^2}(A_mC_{i,m}A_i^* - A_m^*C_{i,m}^*A_i)\right]$$

$$i = 1, 2, \ldots M. \tag{2}$$

For a two-element linear array $M = 2$, we get the coupled equations

$$S = S_1\left[1 - \frac{1}{j4Q_1A_1^2}(A_2C_{1,2}A_1^* - A_2^*C_{1,2}^*A_1)\right] \tag{3}$$

$$S = S_2\left[1 - \frac{1}{j4Q_2A_2^2}(A_1C_{2,1}A_2^* - A_1^*C_{2,1}^*A_2)\right]. \tag{4}$$

Assuming that the amplitudes of oscillators are approximately the same, we have $C_{1,2} = C_{2,1}$ by reciprocity.

Let $C = C_{1,2} = C_{2,1} = C\exp(-j\Phi)$ and $A_1 = A\exp(-j\varphi_1)$, $A_2 = A\exp(-j\varphi_2)$; $Q = Q_1 = Q_2$. Then (3) and (4) can be written as

$$S = S_1\left[1 - \frac{C}{2Q}\sin(\varphi_1 - \varphi_2 - \Phi)\right] \tag{5}$$

$$S = S_2\left[1 - \frac{C}{2Q}\sin(\varphi_2 - \varphi_1 - \Phi)\right]. \tag{6}$$

For two radiating elements operating at the same oscillation frequency ($S_1 = S_2$) in a two-element linear arrays (either E-plane or H-plane), from (5) and (6), it is required that

$$\sin(\varphi_1 - \varphi_2 - \Phi) = \sin(\varphi_2 - \varphi_1 - \Phi). \tag{7}$$

Therefore, $\varphi_1 - \varphi_2 - \Phi = \varphi_2 - \varphi_1 - \Phi + 2n\pi$, and thus $\varphi_1 - \varphi_2 = n\pi$. This result states that for coherent power combining the phase relation of the elements must satisfy the following equation

$$\varphi_1 - \varphi_2 = n\pi \tag{8}$$

where $n = 0, \pm1, \pm2, \cdots$. This result agrees with [14].

Consider a more complex case of a two by two element array, $M = 2$ and $N = 2$. From (1), the following coupled equations are derived:

$$S = S_{11}\left[1 - \frac{1}{j4Q_{11}A_{11}^2}(A_{12}C_{11,12}A_{11}^* + A_{21}C_{11,21}A_{11}^* + A_{22}C_{11,22}A_{11}^* - A_{12}^*C_{11,12}^*A_{11} - A_{21}^*C_{11,21}^*A_{11} - A_{22}^*C_{11,22}^*A_{11})\right] \tag{9}$$

$$S = S_{12}\left[1 - \frac{1}{j4Q_{12}A_{12}^2}(A_{11}C_{12,11}A_{12}^* + A_{21}C_{12,21}A_{12}^* + A_{22}C_{12,22}A_{12}^* - A_{11}^*C_{12,11}^*A_{12} - A_{21}^*C_{12,21}^*A_{12} - A_{22}^*C_{12,22}^*A_{12})\right] \tag{10}$$

$$S = S_{21}\left[1 - \frac{1}{j4Q_{21}A_{21}^2}(A_{11}C_{21,11}A_{21}^* + A_{12}C_{21,12}A_{21}^* + A_{22}C_{21,22}A_{21}^* - A_{11}^*C_{21,11}^*A_{21} - A_{12}^*C_{21,12}^*A_{21} - A_{22}^*C_{21,22}^*A_{21})\right] \tag{11}$$

$$S = S_{22}\left[1 - \frac{1}{j4Q_{22}A_{22}^2}(A_{11}C_{22,11}A_{22}^* + A_{12}C_{22,12}A_{22}^* + A_{21}C_{22,21}A_{22}^* - A_{11}^*C_{22,11}^*A_{22} - A_{12}^*C_{22,12}^*A_{22} - A_{21}^*C_{22,21}^*A_{22})\right]. \tag{12}$$

For the same reason as before and for phase coherent power combining, allowing the spaces between the elements to be the same, we have $C_{mn,ij} = C_{ij,mn}$ by reciprocity. Let

$$A_{11} = A\exp(-j\varphi_{11}), \quad A_{12} = A\exp(-j\varphi_{12}).$$
$$A_{21} = A\exp(-j\varphi_{21}), \quad A_{22} = A\exp(-j\varphi_{22}).$$

$$Q = Q_{11} = Q_{12} = Q_{21} = Q_{22}$$

and

$$C_a = C_{11,12} = C_{11,21} = C_a\exp(-j\Phi_a).$$
$$C_b = C_{11,22} = C_{22,11} = C_b\exp(-j\Phi_b).$$

One can obtain

$$S = S_{11}\left[1 - \frac{C_a}{2Q}\left(\sin(\Delta_1 - \Phi_a) + \sin(\Delta_2 - \Phi_a) + \frac{C_b}{C_a}\sin(\Delta_3 - \Phi_b)\right)\right] \tag{13}$$

$$S = S_{12}\left[1 - \frac{C_a}{2Q}\left(-\sin(\Delta_1 + \Phi_a) + \frac{C_b}{C_a}\sin(\Delta_2 - \Delta_1 - \Phi_b) + \sin(\Delta_3 - \Delta_1 - \Phi_a)\right)\right] \tag{14}$$

$$S = S_{21}\left[1 - \frac{C_a}{2Q}\left(-\sin(\Delta_2 + \Phi_a) + \frac{C_b}{C_a}\sin(\Delta_1 - \Delta_2 - \Phi_b) + \sin(\Delta_3 - \Delta_2 - \Phi_a)\right)\right] \tag{15}$$

$$S = S_{22}\left[1 - \frac{C_a}{2Q}\left(-\frac{C_b}{C_a}\sin(\Delta_3 + \Phi_b) + \sin(\Delta_1 - \Delta_3 - \Phi_a) + \sin(\Delta_2 - \Delta_3 - \Phi_a)\right)\right] \tag{16}$$

where $\Delta_1 = \varphi_{11} - \varphi_{12}$, $\Delta_2 = \varphi_{11} - \varphi_{21}$, $\Delta_3 = \varphi_{11} - \varphi_{22}$.

For these elements operating at the same frequency for coherent combining ($S_{11} = S_{12} = S_{21} = S_{22}$), from (13)–(16), it is required that $\Delta_1 = n\pi$, $\Delta_2 = m\pi$, $\Delta_3 = k\pi$, $n, m, k = 0, \pm 1, \pm 2, \cdots$. In other words, for a symmetrical 2×2 array, the phase difference of a phase-coherent mode must be multiples of π for any spacing between the elements. The theory is suitable for weakly coupled ($C_{mn,ij} \ll 1$) array and the spacing between elements has an effect on the radiation pattern of the array.

We can conclude that

1) For a weakly coherent power combining of a 2×2 symmetrical array, the phase relation must be $n\pi$ for any spacing between the elements.

2) Any coherent power combining array has an optimal element spacing that produces the lowest side lobes for that array.

III. Single Radiating Element

Every element in the preceding discussion about weakly coupled array was ideal. Fabrication tolerances or other perturbations can cause error in practice.

A rectangular patch typically has the feed along the middle of the H-plane dimension to excite the dominant TE_{10} mode. The principal plane cross-polarization results from the higher order TE_{20} and TE_{02} modes. When an active device is put slightly off the mid plane, the cross-polarization of TE_{01} mode is also excited.

Fig. 1 shows a novel FET active circular patch antenna with improved cross-polarization. The circuit was constructed on RT/Duroid 5870 ($\epsilon_r = 2.33$) with a thickness of 62 mils. The active devices used were Fujitsu FHX35LG general purpose FET's. The rated output power of this FET is 25 mW at 12 GHz. The gaps between the source and drain and between the source and the gate form a feedback circuit to make the device unstable. The patches serve both as a resonator in the feedback loop for the FET oscillator and as a radiating element. The main difference from the conventional patch antenna is that this patch antenna has no ground plane on the substrate. Instead, a reflecting mirror that has dimensions of 90 mm by 200 mm was placed behind the circuit. Compared with the rectangular patch that has two dominant modes TE_{01} and TE_{10}, one of which cause high cross-polarization, the circular patch only has one dominant TE_{11} mode. The performance of the antenna is not sensitive to the position where the FET is bonded because the FET is put at the edge of the circular patch. As the line width W is small, the circuit performance is not sensitive to the change of W.

Fig. 2 shows the experimental setup. The slab and the mirror form a Fabry–Perot resonator. The relative dielectric constant of the slab was 10.5 with a thickness of 25 mils. Fig. 3 shows the E and H-plane pattern of the antenna. High cross-polarization levels appear approximately at ± 80 degrees from the peak of the main lobe. Rectangular patch antennas usually have high cross-polarization at ± 45 degrees.

A standard gain horn antenna with a gain of G_1 was used to measure the power output from the active patch antenna

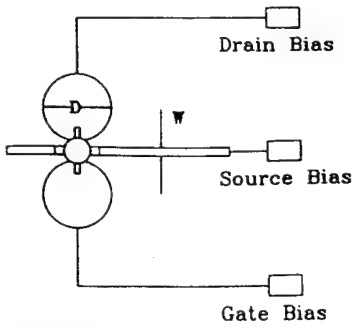

Fig. 1. Circuit configuration of a FET active circular patch antenna; W =0.5 mm, D =6.5 mm.

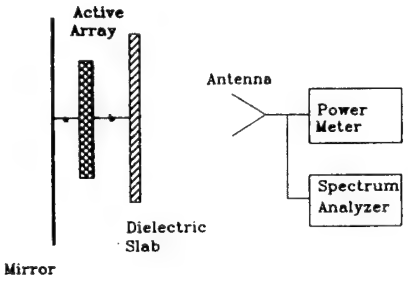

Fig. 2. Quasi-optical power combining measurement setup.

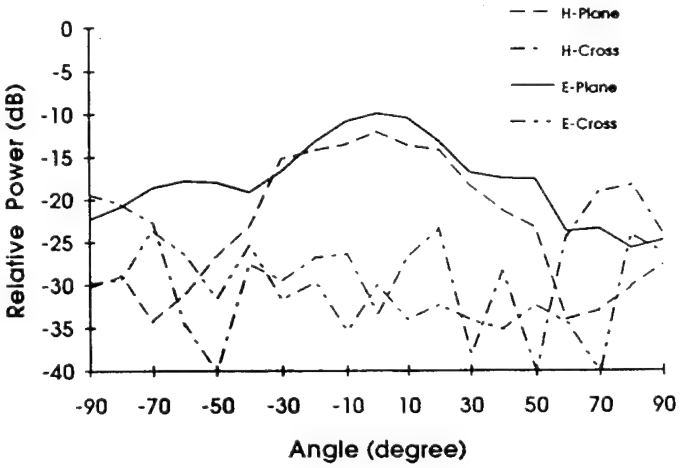

Fig. 3. E and H-plane patterns of the single element active antenna.

array. The horn antenna was placed a distance R from the active antenna. The received power P_r was measured using a power meter. The equivalent isotropic radiated power (EIRP) of the active antenna was calculated using the equation

$$\text{EIRP} = P_r \left(\frac{4\pi R}{\lambda_0} \right)^2 \frac{1}{G_1} \tag{17}$$

where λ_0 is the wavelength in free space.

An EIRP of 120 mW was achieved at 8.4 GHz for a single element. The cross-polarization was 6 dB down from the peak power in both the E and H-planes.

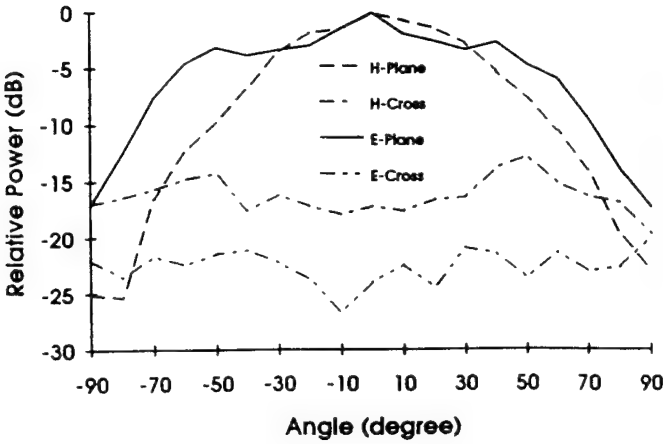

Fig. 4. E and H-plane patterns of a two element linear array.

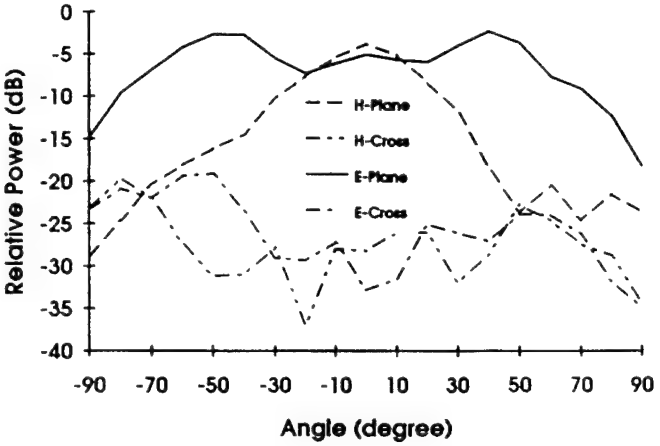

Fig. 6. E and H-plane patterns of the four-element linear array.

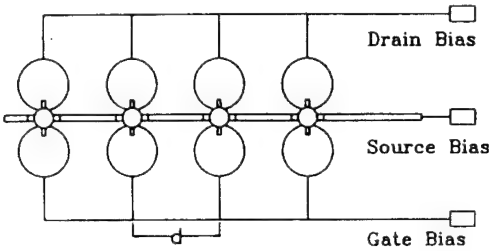

Fig. 5. Four element active antenna linear array.

IV. Two-Element and Four-Element Active FET Antenna Linear Array

According to the principle of antenna pattern multiplication, the cross-polarization should be improved by using this kind of antenna to form an array with an element spacing approximately $\lambda_0/2$. Our experiments have proved this conclusion. Fig. 4 shows the typical E and H-plane patterns of a two element linear array with cross-polarization 13 dB down in both the E and H-planes. An EIRP of 520 mW was achieved at 8.4 GHz. The power combining efficiency is 107%. The greater than 100% combining efficiency is due to the better matching of the devices in the 1 × 2 array. The power combining is calculated based on the assumption that the antenna gain of an N-element array is N times of that of a single element. Therefore, the EIRP of an array is $N^2\times$ single element EIRP for a 100% combining efficiency.

Mutual coupling between the oscillator elements will have an effect on the injection locking behavior of the array. The single element described in the previous section was used to form the 4-element linear array shown in Fig. 5. The spacing between the elements d is approximately $\lambda_0/2$. The active array was operated by connecting the bias lines from the elements to a single power supply.

Section II emphasized that the individual oscillators should have nearly identical oscillation frequencies. Identical oscillation frequencies can be obtained by using separate power supplies to adjust the bias voltage of each element. However, providing individual bias to each element in a large array containing several hundred devices is impractical.

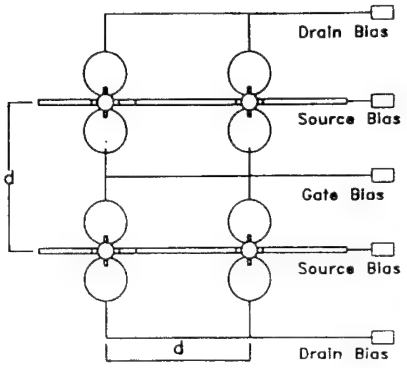

Fig. 7. Two by two active patch antenna array.

Due to variances of individual FET parameter, the resonant frequency of each oscillator could be slightly different for the same bias used. The reflecting mirror can give some tuning of the array and force the power radiated into one direction. The dielectric slab together with reflecting mirror increases the coupling between the elements and the gain of the array. The increased coupling help injection-locking the elements in the array to operate at the same frequency.

Fig. 6 shows the E and H-plane patterns of the four-element FET active patch antenna array. The cross-polarization is 16 dB down from the co-polarization radiation in both the E and H-planes. An EIRP of 1.3 W was achieved at 8.4 GHz. The power combining efficiency is 68%.

V. Two by Two Active FET Antenna Array

The two by two array shown in Fig. 7, was constructed and tested with element spacing of d approximately $\lambda_0/2$. The typical E and H-plane patterns of the arrays are shown in Fig. 8. In the experiments, stable and phase coherent power combining was achieved for several different element spacings. As discussed earlier, the element spacing has effects on the radiation pattern of the array. For a particular type of element and number of elements, there exists an optimum element spacing.

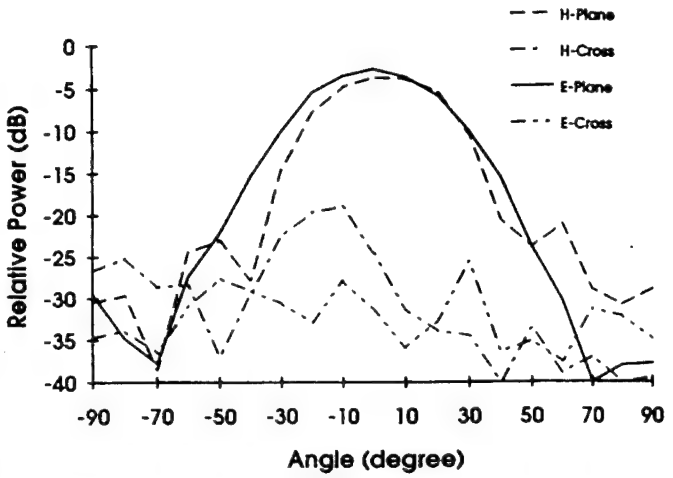

Fig. 8. E and H-plane patterns of the two by two active antenna array.

A 1.5 W equivalent isotropic radiated power was achieved at 8.4 GHz. The power combining efficiency is 78%. The cross-polarization was 16 dB from the peak power in both the E and H-planes.

VI. Results for Two by Four Active Patch Antenna Array

A two by four array was also built and tested. Fig. 9 shows the circuit arrangement and the photograph with element spacing d of approximately $\lambda_0/2$. Proper operation of array requires that all elements have nearly identical physical characteristics. This is difficult to achieve due to variances in individual FET parameters. Small frequency tuning could be achieved by adjusting the position of the dielectric slab and the position of the reflecting mirror. Choosing FET's with similar parameters is important in the design of a large active antenna array. Accurate placement of the device is also important. Monolithic fabrication of the active antenna array is preferred for a large array.

For the two by four array, an equivalent isotropic radiated power of 3.8 W was achieved at 8.99 GHz. The combining efficiency is about 50%. The reduction of combining efficient is due to the sidelobes which need to be improved in the future. The change of frequency is due to coupling among the elements. Fig. 10 shows the typical E and H-plane radiation patterns. The spectrum is similar to that of the two by two arrays.

VII. Conclusions

This paper has presented a novel FET active circular patch antenna element and arrays. The use of circular patch antenna has the advantage because it has only one dominant mode that causes lower cross-polarization level. Two, four, and eight of these elements were used successfully as power combiners. The optimum element spacing of the array depends on the element structure and the number of elements. By changing the positions of the dielectric slab and the reflecting mirror, a proper phase relation can be obtained and the output power of the active array can be optimized. This circuit should have many applications in low cost transmitters at microwave and millimeter-wave frequencies. The circuit is amenable to monolithic implementation.

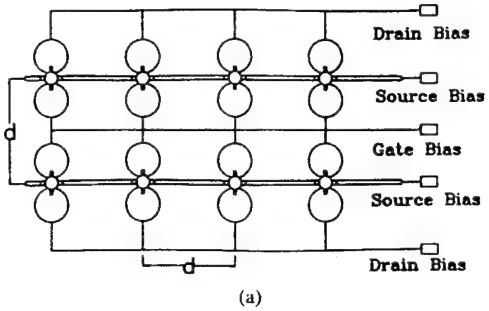

(a)

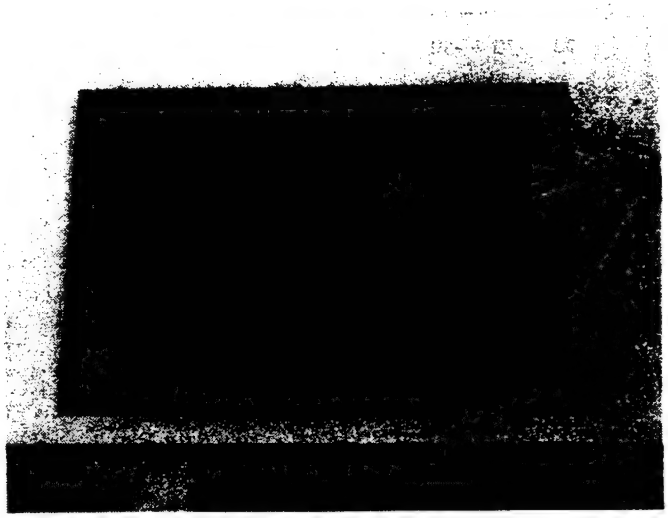

(b)

Fig. 9. Two by four active patch antenna array. (a) Circuit configuration; (b) A photograph.

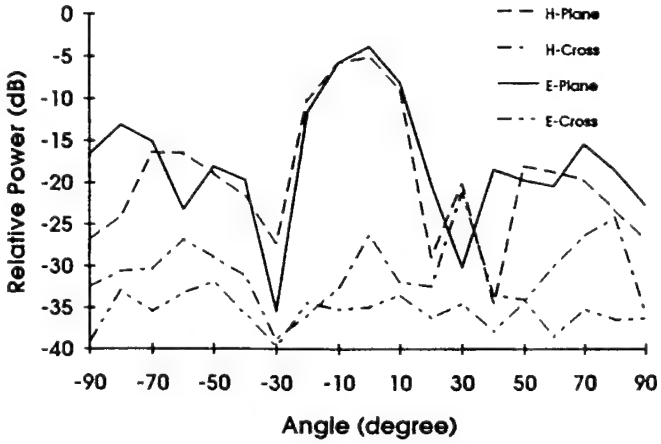

Fig. 10. E and H-plane patterns of the two by four active antenna array.

Acknowledgment

The authors would like to thank K. Leverich, B. Phung, L. Fan, and M. Li for their help in drawing the mask and fabricating the circuits. The authors would also like to thank J. McCleary and J. McSpadden for reviewing this paper.

REFERENCES

[1] K. Chang and C. Sun, "Millimeter-wave power combining techniques," *IEEE Trans. Microwave Theory Tech.*, vol. MTT-31, pp. 91–107, Feb. 1983.

[2] J. W. Mink, "Quasi-optical power combining of solid-state millimeter-wave sources," *IEEE Trans. Microwave Theory Tech.*, vol. MTT-34, pp. 273–279, Feb. 1986.

[3] Z. B. Popovic, R. M. Weikle II, M. Kim, and D. B. Rutledge, "A 100 MESFET planar grid oscillator," *IEEE Trans. Microwave Theory Tech.*, vol. 39, pp. 193–200, Feb. 1991.

[4] Z. B. Popovic, R. M. Weikle II, M. Kim, K. A. Potter, and D. B. Rutledge, "Bar-grid oscillators," *IEEE Trans. Microwave Theory Tech.*, vol. 38, pp. 225–230, Mar. 1990.

[5] J. Birkeland and T. Itoh, "A 16 element quasi-optical FET oscillator power combining array with external injection locking," *IEEE Trans. Microwave Theory Tech.*, vol. 40, pp. 475–481, Mar. 1992.

[6] A. Mortazawi, H. D. Foltz, and T. Itoh, "A periodic second harmonic spatial power combining oscillator," *IEEE Trans. Microwave Theory Tech.*, vol. 40, pp. 851–856, May 1992.

[7] R. A. York and R. C. Compton, "Quasi-optical power combining using mutually synchronized oscillator arrays," *IEEE Trans. Microwave Theory Tech.*, vol. 39, pp. 1000–1009, June 1991.

[8] K. Chang, K. A. Hummer, and J. L. Klein, "Experiments on injection locking of active antenna elements for active phased array and spatial power combiner," *IEEE Trans. Microwave Theory Tech.*, vol. 37, pp. 1078–1084, July 1989.

[9] K. Chang, K. A. Hummer, and G. K. Gopalakrishnan, "Active radiating element using FET source integrated with microstrip patch antenna," *Electron. Lett.*, vol. 24, pp. 1347–1348, Oct. 1988.

[10] R. A. York and R. C. Compton, "Dual-device active patch antenna with improved radiation characteristics," *Electron. Lett.*, vol. 28, pp. 1019–1021, May 1992.

[11] X. D. Wu, W. K. Leverich, and K. Chang, "Dual-FET active antenna," *Electron. Lett.*, vol. 28, pp. 1853–1854, Sept. 1992.

[12] R. Adler, "A study of locking phenomena in oscillators," *Proc. IEEE*, vol. 61, pp. 1380–1385, Oct. 1973.

[13] K. Kurokawa, "Injection-locking of solid-state microwave oscillators," *Proc. IEEE*, vol. 61, pp. 1386–1410, Oct. 1973.

[14] K. D. Stephan and S. L. Young, "Mode stability of radiation-coupled interinjection-locked oscillators for integrated phased arrays," *IEEE Trans. Microwave Theory Tech.*, vol. MTT-36, pp. 921–924, May 1988.

[15] K. D. Stephan, "Inter-injection-locked oscillators for power combining and phased arrays," *IEEE Trans. Microwave Theory Tech.*, vol. MTT-34, pp. 1017–1025, Oct. 1986.

New Uniplanar Coplanar Waveguide Hybrid-Ring Couplers and Magic-T's

Chien-Hsun Ho, Lu Fan, and Kai Chang, *Fellow, IEEE*

Abstract— **The uniplanar coplanar waveguide (CPW) and slotline on a dielectric substrate have many applications to MIC and MMIC designs. A new reverse-phase CPW hybrid-ring coupler and a uniplanar CPW magic-T were developed. Experimental results showed that the hybrid-ring coupler has a 60% bandwidth centered at 3 GHz and the magic-T has a bandwidth of one octave from 2 to 4 GHz with 0.4 dB amplitude imbalance and 3.5° phase imbalance. Also, this paper presents theoretical analyses of CPW–slotline transitions using the transmission line models. Accurate modeling of nonuniform CPW and slotline radial stubs was developed using tandem connected uniform lines. Measured results of various CPW–slotline transitions agree very well with calculation. Design curves of the transitions are given for practical applications. To fully use the advantages of uniplanar structures, a 180° reverse-phase CPW–slotline back-to-back balun and a tee junction are described. Both circuits provide good amplitude and phase characteristic over a broad bandwidth due to the phase change of the circuits being independent of frequency.**

I. Introduction

ALTHOUGH microstrip is the most widely used planar transmission line, other forms of uniplanar transmission lines are available for circuit design. These uniplanar transmission lines include coplanar waveguide (CPW), slotline, and coplanar strip (CPS). Some drawbacks of using microstrip include sensitivity to substrate thickness, difficulty of inserting shunt solid-state devices, and the requirement of high-impedance lines for dc biasing. Uniplanar transmission lines have small dispersion, simple realization of short-circuited ends, the possibility of simple integration of lumped elements or active components, and circumventing the need for via holes. These characteristics make CPW, slotline, and CPS important in microwave and millimeter-wave integrated circuit design. Many attractive components using uniplanar structures have been published [1]–[6]. This paper presents uniplanar hybrid coupler components that have characteristics similar to those of the microstrip circuits, but with the advantages of uniplanar structure and better performance.

Manuscript received March 23, 1994; revised June 7, 1994. This work was supported in part by the U.S. Army Research Office, the NASA Center for Space Power, and the State of Texas Higher Education Coordinating Board's Advanced Technology Program.

C.-H. Ho was with the Department of Electrical Engineering, Texas A&M University, College Station, TX 77843 USA. He is now with Garmin Communication & Navigation, Lenexa, KS 66215 USA.

L. Fan and K. Chang are with Department of Electrical Engineering, Texas A&M University, College Station, TX 77843 USA.

IEEE Log Number 9405416.

To fully use the advantages of uniplanar structures, broad-band transitions of CPW–slotline are necessary. The theoretical analyses of CPW–slotline transitions using the transmission line models are presented in Section II. Simulations of various transitions agree very well with measurement results. Section III describes the fundamental characteristics of a 180° reverse-phase CPW–slotline balun and a tee junction. Both circuits use a 180° reverse-phase CPW–slotline back-to-back transition to achieve a 180° reversal. The phase shift of the circuits is frequency independent. In Sections IV and V, the designs and applications of a new reverse-phase CPW hybrid-ring coupler and a uniplanar CPW magic-T are illustrated. The circuit analyses for the CPW hybrids are based on simple transmission line circuit models. The measured results agree with the theoretical predictions very well.

II. Transmission Line Modeling of CPW–Slotline Transitions

Broad-band transitions from CPW to slotline [7]–[10] have been reported by many researchers. The transitions presented in [7], [8] use the CPW–slot double junction. The transitions in [9], [10] use the uniform slotline square stub and nonuniform slotline circular stub, respectively. In 1993, based on experimental investigations, the authors of this paper gave a systematic approach to this problem [11]. Various transitions were developed, and the best combination of using CPW short circuits and slotline radial stubs was proposed for broad-band matching between CPW and slotline. Based on the previous experimental investigations, this section presents an analysis of CPW–slotline transitions using simple equivalent circuit transmission line models on Touchstone. There is a fairly good agreement between measured and calculated results.

A. Uniform CPW–Slotline Transitions

The CPW–slotline transitions discussed here were fabricated on a 1.27-mm-thick RT/Duroid 6010 ($\epsilon_r = 10.8$) substrate. The CPW and slotline feed lines were both chosen as 50 Ω. Fig. 1 shows the circuit configuration and equivalent transmission line model of the uniform CPW–slotline cross-junction, which was defined as the type-a transition in [11]. The CPW and slotline in Fig. 1(a) cross each other at a right angle. The CPW extends one quarter-wavelength beyond the slotlines and terminates with an open circuit, while the slotline extends one quarter-wavelength beyond the CPW and terminates with a short circuit. The extensions of CPW and slotline act as a tuning stub to match each other. Fig. 2(a) shows the measured

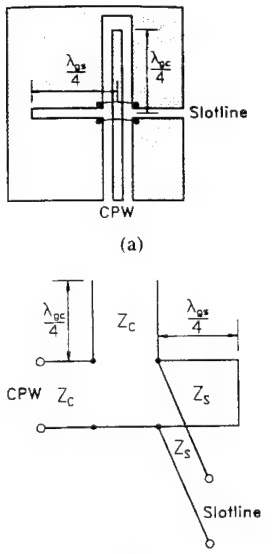

Fig. 1. (a) Physical configuration and (b) equivalent transmission line model for the type-a CPW–slotline transition.

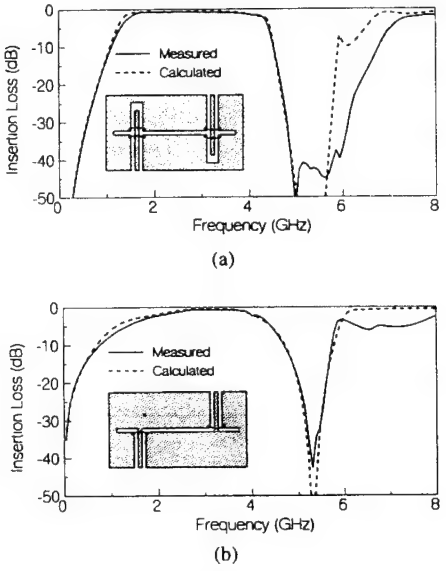

Fig. 2. Measured and calculated insertion loss of one pair of (a) type-a and (b) type-b CPW–slotline transitions. CPW gap size $G_C = 0.25$ mm, CPW center and conductor width $S_C = 0.5$ mm, slotline line width $W_S = 0.1$ mm, $\lambda_{gc} = 41.64$ mm, $\lambda_{gs} = 46.98$ mm.

and calculated frequency responses of insertion loss for the type-a back-to-back transition. The calculated results agree very well with the experimental data with less than 0.5 dB difference in the passband region. The bandwidth for insertion loss of less than 1 dB for the type-a back-to-back transition is from 1.6 to 3.6 GHz. The transition using a CPW short with a slotline $\lambda_{gs}/4$ shorted stub, i.e., type-b transition, is a special case of the uniform CPW–slotline cross junction. Fig. 2(b) shows the measured and calculated frequency responses of insertion loss for the type-b back-to-back transition. The type-b CPW–slotline transition has a narrow bandwidth because it depends only on a slotline $\lambda_{gs}/4$ shorted stub which is strongly frequency dependent.

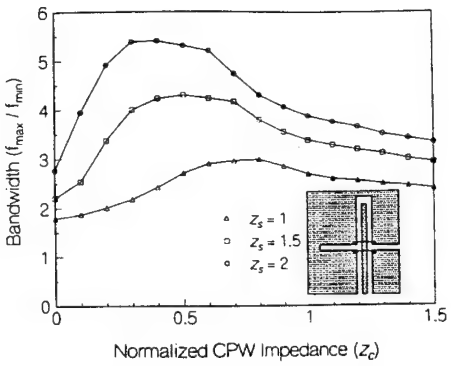

Fig. 3. Calculated 1 dB bandwidth of the type-a back-to-back transition against the normalized CPW characteristic impedance.

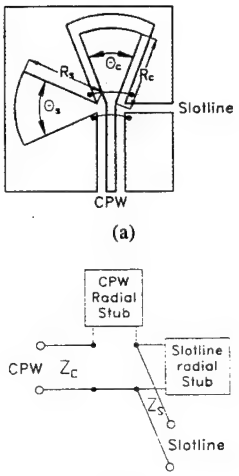

Fig. 4. (a) Physical configuration and (b) equivalent transmission line model for the type-h CPW–slotline transition.

For practical applications, it is useful to know the optimal combination of the CPW and slotline characteristic impedances. Fig. 3 shows the calculated 1 dB bandwidth of the uniform CPW–slotline back-to-back transition with given normalized slotline characteristic impedances $z_s = 1$, 1.5, and 2, against the normalized CPW characteristic impedance z_c. As shown in Fig. 3, it is noticeable that the optimum z_c for the maximum bandwidth decreases with the larger z_s. For $z_s = 1$, 1.5, and 2, the optimum normalized CPW characteristic impedances are $z_c = 1$, 0.5, and 0.3, respectively. In Fig. 3, given a z_c, the 1 dB bandwidth increases with a larger z_s. This implies that the slotline matching stubs are the dominant factors in designing the type-a transitions. Although the slotline characteristic impedance can be chosen as high as possible to increase the bandwidth, the required optimum CPW characteristic impedance might be too low to be implemented.

B. Nonuniform CPW–Slotline Transitions

Fig. 4 shows the circuit configuration and equivalent transmission line model of the nonuniform CPW–slotline cross junction, which was defined as the type-h transition in [11].

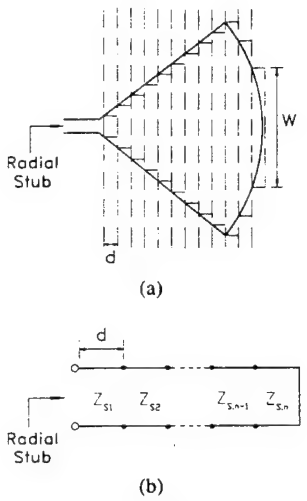

Fig. 5. (a) Radial stub modeled by tandem connected segments of piecewise uniform lines. (b) Equivalent transmission line model.

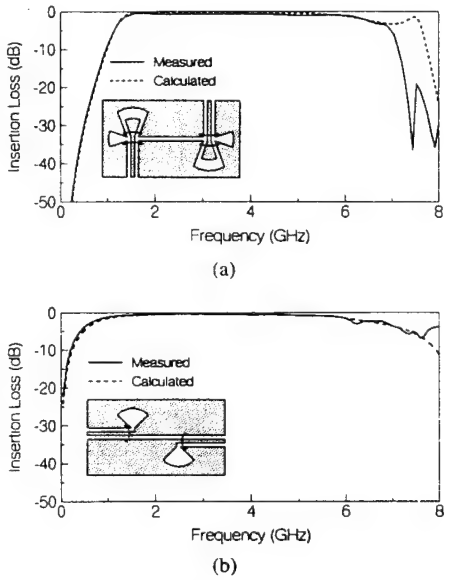

Fig. 6. Measured and calculated insertion loss of one pair of (a) type-h and (b) type-g CPW–slotline transitions. CPW feed line gap size $G_C = 0.25$ mm, center conductor width $S_C = 0.5$ mm, slotline feed line width $W_S = 0.1$ mm, $R_C = 6$ mm, $\theta_C = 60°$, $R_S = 6$ mm, and $\theta_S = 60°$.

The CPW and slotline radial stubs are used for broad-band impedance matching. They are modeled by tandem-connected segments of piecewise uniform lines, as shown in Fig. 5. Fig. 6(a) shows the measured and calculated frequency responses of insertion loss for the type-h back-to-back transition. The calculated results were obtained from the equivalent transmission line model of Fig. 4(b) with the radial stub simulated by a cascade of ten line segments of equal length but different characteristic impedance and dispersion characteristics. The theoretical results agree very well with the experimental data. The 1 dB bandwidth of the type-h transition is from 1.5 to 6.0 GHz. Similar modeling was carried out for a type-g CPW–slotline transition, and the results are given in Fig. 6(b). Type-g can be considered as the special case of

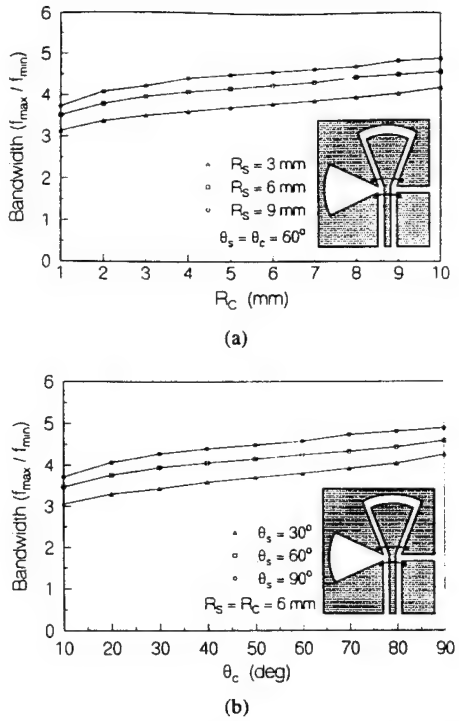

Fig. 7. Calculated 1 dB bandwidth of the type-h back-to-back transition against (a) the radius and (b) the angle of the CPW radial stub.

the nonuniform CPW–slotline cross junction. The CPW radial stubs are replaced by CPW shorts.

Fig. 7(a) shows the calculated 1 dB bandwidth with given radii of the slotline radial stub $R_S = 3$, 6, and 9 mm, against the radius of the CPW radius stub R_C. As shown in Fig. 7(a), the 1 dB bandwidth increases with a larger CPW radius because the larger CPW radial stub provides a better shorted circuit. Fig. 7(b) shows the calculated 1 dB bandwidth with given radial angles of the slotline radial stub $\theta_S = 30°$, 60°, and 90°, against the angle of the CPW radius stub θ_C. Again, the 1 dB bandwidth increases with a larger CPW radial stub.

As shown in Fig. 6, the type-g CPW–slotline transition has a broader bandwidth than the type-h CPW–slotline transition because the CPW short is an ideal short circuit and the slotline radial stub is a broad-band open. The bandwidth of the nonuniform transition with a CPW radial stub is always lower than that of the nonuniform transition with a CPW short.

III. 180° Reverse-Phase CPW–Slotline Baluns and Tee Junction

A. 180° Reverse-Phase CPW–Slotline Baluns

It is well known that a 180° phase change in excess of the signal path occurs when two microstrip-to-parallel-plate-line tapered baluns are connected back to back [12]. This phase change can be used in wide-band circuits. Hede [13] also presented a broad-band pulse inverter based on the same principle in 1977. The bandwidth measurement indicates that the pulse inverter works up to 1 GHz. Fig. 8(a) shows the 180° reverse-phase microstrip back-to-back tapered

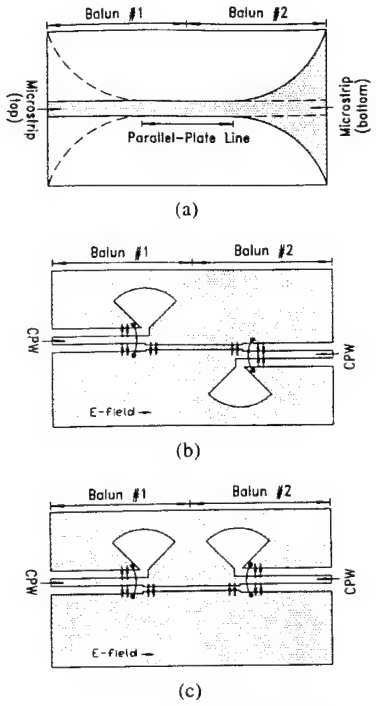

Fig. 8. Circuit configurations and schematic diagrams of E-field distribution for (a) the 180° reverse-phase microstrip back-to-back baluns, (b) the 180° reverse-phase CPW–slotline back-to-back baluns, and (c) the in-phase CPW–slotline back-to-back baluns.

baluns which are commonly used in the balanced mixers and antenna feeds. Although the 180° reverse-phase microstrip back-to-back tapered baluns have a very wide bandwidth, the use of double-sided ground planes results in a complicated fabrication and packaging process. To overcome this problem, a new uniplanar 180° reverse-phase back-to-back balun using two broad-band CPW–slotline transitions is described in the following.

Fig. 8(b) shows the circuit configuration and schematic diagram of E-field distribution for the 180° reverse-phase CPW–slotline back-to-back baluns. The two CPW–slotline transitions use CPW shorts and slotline radial stubs. The slotline radial stubs are placed on the opposite side of the internal slotline (i.e., a pair of type-g CPW–slotline transitions in [11]). Each side of the internal slotline connects the center conductor (or ground plane) of the CPW in balun 1 and the ground plane (or center conductor) of the CPW in balun 2. Referring to Fig. 8(b), a 180° phase change of the E field is introduced into the output signal at balun 2 when the input signal is excited from balun 1. The phase change of the E-field direction is caused by the inserted slotline section which connects the opposite sides of the CPW gaps at baluns 1 and 2. In Fig. 8(c), the in-phase CPW–slotline back-to-back baluns have two slotline radial stubs which are placed on the same side of the internal slotline section. The E-field directions of the CPW's are in phase at baluns 1 and 2.

To demonstrate the 180° phase reversal of the twisted CPW–slotline back-to-back baluns, a 180° reverse-phase and an in-phase CPW–slotline back-to-back balun were built. The test circuits were fabricated on a 1.27-mm-thick RT/Duroid 6010.8 ($\epsilon_r = 10.8$) substrate with the parameters: characteristic impedance of the CPW and slotline $Z_{C0} = 50\ \Omega$, $Z_S = 50\ \Omega$. The measurements were made using standard SMA connectors and an HP-8510 network analyzer. The measured insertion loss includes two coaxial–CPW transitions and two CPW–slotline transitions.

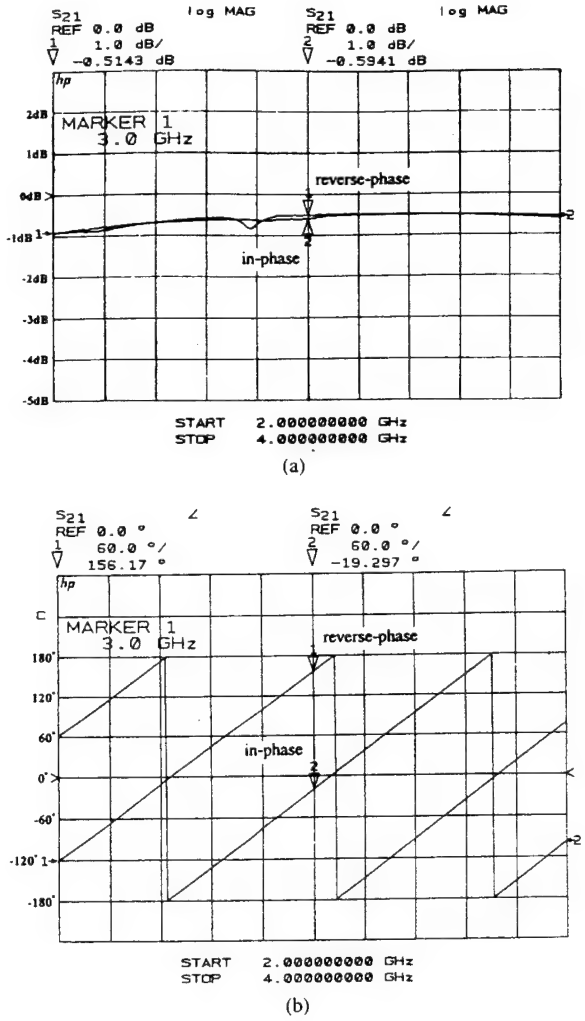

Fig. 9. Measured frequency responses of (a) insertion loss and (b) phase angle for the in-phase and 180° reverse-phase CPW–slotline back-to-back baluns.

Fig. 9(a) and (b) show the measured frequency responses of insertion loss and phase angle for the 180° reverse-phase and in-phase CPW back-to-back baluns, respectively. The amplitude difference between the 180° reverse-phase and in-phase CPW back-to-back baluns is within 0.3 dB from 2 to 4 GHz. Over the same range, maximum phase difference is maintained within 5°. The 5° phase error is due to the mechanical tolerances, misalignments, connectors, and discontinuities.

B. 180° Reverse-Phase CPW–Slotline Tee Junction

Fig. 10 shows the circuit configuration and schematic diagram of the E-field distribution for a 180° reverse-phase CPW–slotline tee junction. The circuit consists of one CPW–slotline tee junction and two CPW–slotline transitions. The arrows shown in Fig. 10 indicate the schematic expression of the electric field in the CPW's and slotlines. The E field in the input CPW (near the CPW–slotline tee junction) is

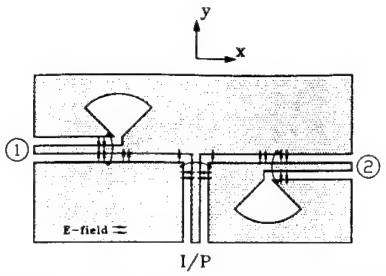

Fig. 10. Circuit configuration and schematic diagram of E-field distribution for the 180° reverse-phase CPW–slotline tee junction.

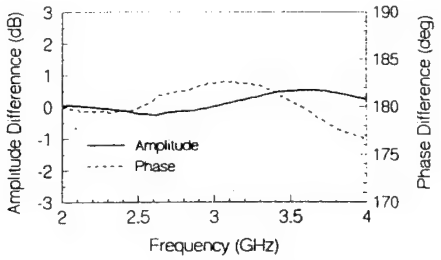

Fig. 11. Measured frequency responses of amplitude and phase differences for the uniplanar 180° reverse-phase CPW–slotline tee junction.

directed to the CPW center conductor. This produces two slotline waves with the E field in the $+y$ direction. At the transition of port 1, the $+y$-directed slotline E field will cause the E field in the output CPW to direct toward the CPW center conductor. However, the E field of the output CPW at port 2 will direct toward the CPW ground plane due to the $+y$-directed slotline E field.

According to the above principle, a truly 180° reverse-phase CPW–slotline tee junction was built on a 1.27-mm-thick RT/Duroid 6010.8 ($\epsilon_r = 10.8$) substrate with the parameters: characteristic impedance of the CPW feed lines $Z_{C0} = 50\ \Omega$, characteristic impedance of the slotline $Z_S = 70.7\ \Omega$. Fig. 11 shows the frequency responses of the amplitude and phase difference. The maximum amplitude difference is 0.6 dB from 2 to 4 GHz. Over the same frequency range, the maximum phase difference is 3.5°.

IV. 180° Reverse-Phase Hybrid-Ring Couplers

Hybrid couplers are indispensable components used in various MIC applications such as balanced mixers, balanced amplifiers, frequency discriminators, phase shifters, and feeding networks in antenna arrays. The rat-race hybrid-ring coupler [14] is the well-known and commonly used 180° hybrid. The 20–26% bandwidth of the rat-race coupler limits its applications to narrow-band circuits. Several design techniques have been developed to extend the bandwidth. One technique in [15], [16] used a $\lambda_g/4$ coupled-line section to replace the $3\lambda_g/4$ section of the conventional $3\lambda_g/2$ microstrip rat-race hybrid-ring coupler. Although the bandwidth of the reverse-phase hybrid-ring coupler has been improved up to more than one octave, the difficulty of constructing the shorted coupled-line section limits its use at low frequencies. In 1971, Chua [17] proposed a modified microstrip reverse-phase hybrid-ring coupler. The coupler substitutes a $\lambda_g/4$ slotline for the $3\lambda_g/4$ phase delay section of the conventional microstrip rat-race hybrid-ring coupler. Although the modified version gives good performance, the double-sided implementation of a curved $3\lambda_g/4$ microstrip line with an inserted $\lambda_g/4$ slotline is not easy for the photolithography process. Also, the ground pins are needed for the microstrip shorts.

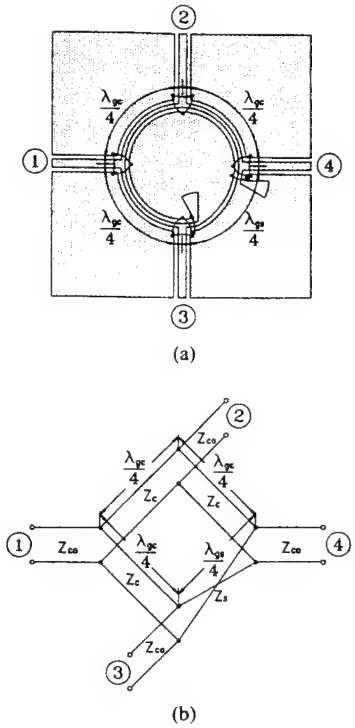

Fig. 12. (a) Circuit configuration and (b) equivalent transmission line model of the uniplanar reverse-phase hybrid-ring coupler.

To overcome these problems, this section reports a uniplanar reverse-phase CPW hybrid-ring coupler using a 180° reverse-phase CPW–slotline back-to-back balun. Since this 180° phase change of the CPW–slotline balun is frequency independent, the resulting uniplanar reverse-phase hybrid-ring coupler provides good amplitude and phase characteristics over a broad bandwidth. The experimental results agree very well with the theoretical design.

Fig. 12(a) shows the circuit layout of the uniplanar reverse-phase CPW hybrid-ring coupler. The circuit consists of four CPW–slotline tee junctions, three quarter-wavelength CPW sections, and one 180° reverse-phase CPW back-to-back balun. As shown in Fig. 12(a), the reverse-phase hybrid-ring coupler substitutes a 180° CPW–slotline phase shifter for the phase delay section used in the conventional rat-race hybrid-ring coupler. The resulting hybrid-ring coupler has a broad bandwidth because the phase change of the 180° reverse-phase CPW back-to-back balun is frequency independent. Fig. 12(b) shows the equivalent transmission line model. The twisted transmission line represents the 180° phase reversal of the CPW–slotline back-to-back baluns.

To test the circuit, a truly uniplanar reverse-phase hybrid-ring coupler was built on an RT/Duroid 6010.8 ($\epsilon_r = 10.8$) substrate with the following dimensions: substrate thickness $h = 1.524$ mm, characteristic impedance of the CPW feed lines $Z_{C0} = 50\ \Omega$, CPW feed lines center conductor width

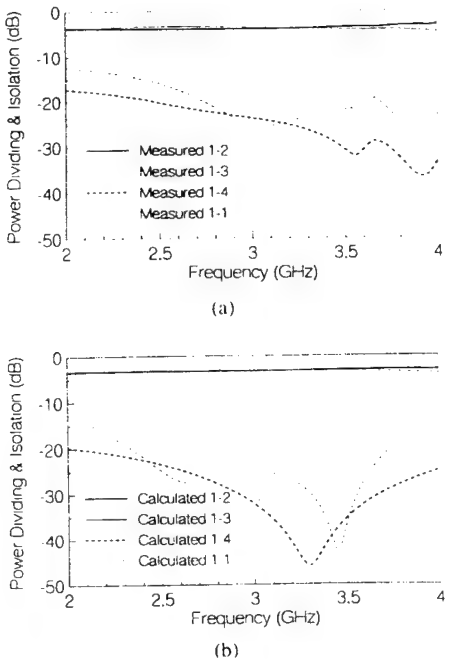

Fig. 13. (a) Measured and (b) calculated frequency responses of power dividing, return loss, and isolation for the uniplanar reverse-phase hybrid-ring coupler.

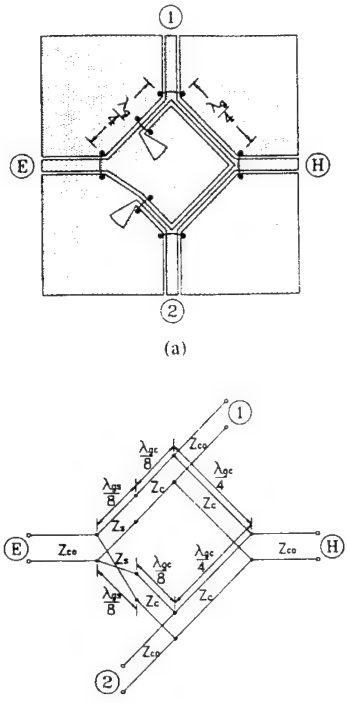

Fig. 14. The uniplanar magic-T (a) circuit configuration and (b) equivalent transmission line model.

$S_{C0} = 0.54$ mm, CPW feed lines gap size $G_{C0} = 0.3$ mm, characteristic impedance of the CPW ring $Z_C = 70.7\ \Omega$, CPW ring center conductor width $S_C = 0.27$ mm, CPW ring gap size $G_C = 0.5$ mm, characteristic impedance of the reverse-phase slotline section $Z_S = 70.7\ \Omega$, slotline line width $W_S = 0.47$ mm, radius of the slotline radial stub $r = 5$ mm, angle of the slotline radial stubs $\theta = 30°$, and CPW ring mean radius $r = 6.70$ mm. The measurements were made using standard SMA connectors and an HP-8510 network analyzer. A computer program based on the equivalent transmission mode of Fig. 12(b) was developed and used to analyze the circuit.

Fig. 13(a) and (b) show the measured and calculated frequency responses of power dividing, return loss, and isolation, respectively. The measured results show that the coupling of the power from port 1 to ports 2 and 3 is 3.4 and 3.7 dB at 3 GHz, respectively. The isolation is 23 dB at 3 GHz. A maximum amplitude imbalance of 0.9 dB has been achieved over a bandwidth from 2 to 3.6 GHz. The isolation between ports 1 and 4 is more than 17 dB over the bandwidth of 2–4 GHz. The calculated results agree very well with the experimental results. As expected, the power-dividing characteristics of the reverse-phase CPW hybrid-ring coupler is less frequency dependent. The insertion loss is mainly from the CPW–slotline transitions.

V. Uniplanar CPW Magic-T's

Magic-T's are fundamental components for many microwave circuits such as power combiners or dividers, balanced mixers, and frequency discriminators. The matched waveguide double-tee is a well-known and commonly used waveguide magic-T [18]. In 1964, [19] first proposed a planar magic-T. The circuit uses an asymmetric coupled transmission line directional coupler and Shiffman's phase-shift network. In 1965, [20] proposed a tapered-line magic-T. The circuit is based on a tapered asymmetrical transformer consisting of two coupled tapered lines. The complete analysis of tapered-line magic-T was discussed in [21]. Reference [22] proposed a planar magic-T using a microstrip balun in 1976. In 1980, [23] proposed a planar magic-T which is constructed with microstrip–slotline tee junctions and coupled slotlines. The planar magic-T uses a double-sided structure and has a bandwidth from 2 to 10 GHz. The two balanced arms of the planar magic-T are on the same side and they do not need the crossover connection.

In recent years, uniplanar transmission lines have emerged as alternatives to microstrip in planar microwave integrated circuits. The uniplanar microwave integrated circuits do not use the back side of the substrate, and allow easy series and shunt connections of passive and active solid-state devices. The use of the uniplanar structures circumvents the need for via holes and reduces processing complexity. In 1987, [24] proposed a uniplanar magic-T which uses three CPW–slotline tee junctions and a slotline tee junction. The in-phase CPW excitation is via an air bridge and the slotline tee junction is used as a phase inverter. The uniplanar magic-T has a narrow bandwidth. In 1993, a broad-band uniplanar magic-T was developed using crossover slotline ring structure [25], [26]. A broad-band microstrip coupled slotline ring coupler was also developed [27]. This section presents a novel uniplanar magic-T circuit using a 180° reverse-phase CPW–slotline junction and three CPW tee junctions. The circuit has the advantages of broad bandwidth and good performance.

Fig. 14(a) shows the circuit configuration of the new uniplanar CPW magic-T. The uniplanar magic-T consists of a 180°

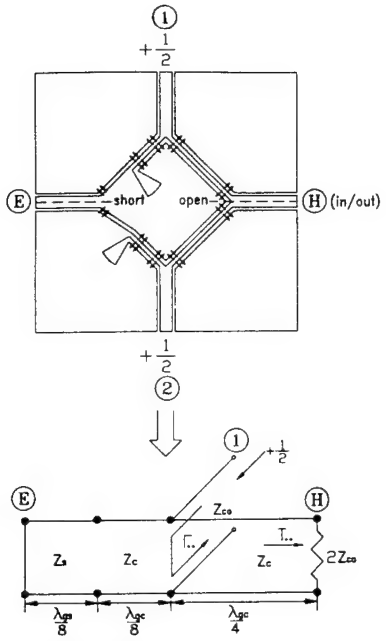

Fig. 15. Schematic expression of the electric field distribution and equivalent circuit for the in-phase coupling mode.

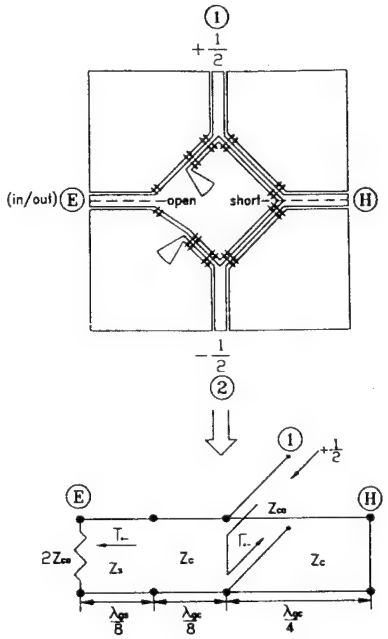

Fig. 16. Schematic expression of the electric field distribution and equivalent circuit for the 180° out-of-phase coupling mode.

reverse-phase CPW–slotline tee junction and three CPW tee junctions. The 180° reverse-phase CPW–slotline tee junction is used as a phase inverter. In Fig. 14(a), ports E and H correspond to the E and H arm of the conventional waveguide magic-T, respectively. Ports 1 and 2 are the power dividing balanced arms. Fig. 14(b) shows the equivalent transmission line model of the uniplanar CPW magic-T. The twisted transmission line in Fig. 14(b) represents the phase reversal of the CPW–slotline tee junction.

Figs. 15 and 16 show the schematic diagram of the E-field distribution and equivalent circuit for the in-phase and 180° out-of-phase couplings, respectively. The arrows shown in Figs. 15 and 16 indicate the schematic expression of the electric field in the CPW's and slotlines. In Fig. 15, the signal is fed to port H, and then divides into two components, which both arrive in phase at ports 1 and 2. The two component waves arrive at port E 180° out of phase and cancel each other. In this case, the symmetry plane at port H corresponds to an open circuit (magnetic wall), while the symmetry plane at port E corresponds to a short circuit (electric wall). In Fig. 16, the signal is fed to port E, and then divides into two components, which arrive at ports 1 and 2 with a 180° phase difference. The 180° phase difference between the divided signals at ports 1 and 2 is due to the 180° reverse-phase CPW–slotline tee junction. The two component waves arrive at port H 180° out of phase and cancel each other. The symmetry plane at port E corresponds to an open circuit (magnetic wall), whereas the symmetry plane at port H corresponds to a short circuit (electric wall). The isolation between ports E and H is perfect as long as the mode conversion in the reverse-phase CPW–slotline tee junction is ideal.

A two-port circuit calculation is used to analyze the isolation and impedance matching instead of the symmetric four-port networks because the circuit is symmetric with respect to ports E and H. The return loss at ports 1 and 2 is given by

$$|S_{11}|,\ |S_{22}| = \tfrac{1}{2}|\Gamma_{++} + \Gamma_{+-}| \tag{1}$$

where Γ_{++} and Γ_{+-} are the voltage reflection coefficients at port 1 for the in-phase mode coupling and 180° out of phase mode coupling, respectively. The isolation between ports 1 and 2 is given by

$$|S_{12}| = \tfrac{1}{2}|\Gamma_{++} - \Gamma_{+-}|. \tag{2}$$

To achieve the impedance matching at ports 1 and 2, i.e., $|S_{11}| = |S_{22}| = 0$, the characteristic impedance of CPW Z_C and slotline Z_S in terms of CPW feed line characteristic impedance Z_{C0} is given by

$$Z_S = Z_C = \sqrt{2}Z_{C0}. \tag{3}$$

According to (1)–(3), a truly uniplanar magic-T was built on a 1.524-mm-thick RT/Duroid 6010.8 ($\epsilon_r = 10.8$) substrate with the following dimensions: characteristic impedance of CPW feed lines $Z_{C0} = 50\ \Omega$, CPW feed lines center conductor width $S_{C0} = 0.54$ mm, CPW feed lines gap size $G_{C0} = 0.3$ mm, characteristic impedance of CPW in the magic-T $Z_C = 70.7\ \Omega$, magic-T's CPW center conductor width $S_C = 0.27$ mm, magic-T CPW gap size $G_C = 0.5$ mm, characteristic impedance of the slotline in the magic-T $Z_S = 70.7\ \Omega$, magic-T's slotline line width $W_S = 0.47$ mm, slotline radial stub angle $\theta = 30°$, and slotline radial stub radius $r = 5$ mm. The measurements were made using standard SMA connectors and an HP-8510 network analyzer. A computer program based on the equivalent transmission model of Fig. 14(b) was developed and used to analyze the circuit.

Fig. 17(a) shows the measured and calculated frequency responses of insertion loss for the H arm's power dividing (i.e., in-phase mode coupling). The extra insertion loss is less than 0.7 dB at the center frequency of 3 GHz. Similarly, Fig. 17(b)

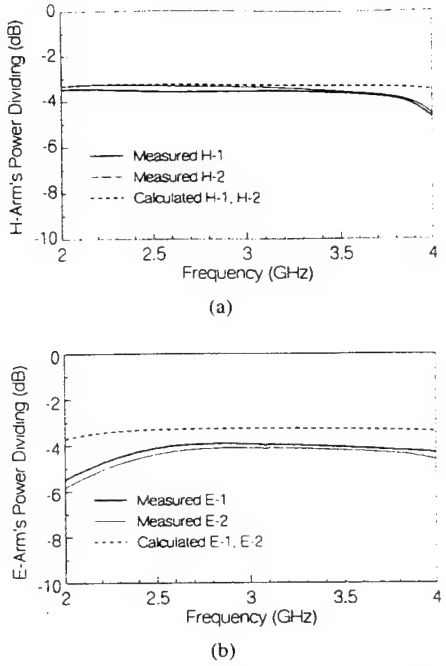

Fig. 17. Measured and calculated frequency responses of the magic-T (a) H arm's power dividing and (b) E arm's power dividing.

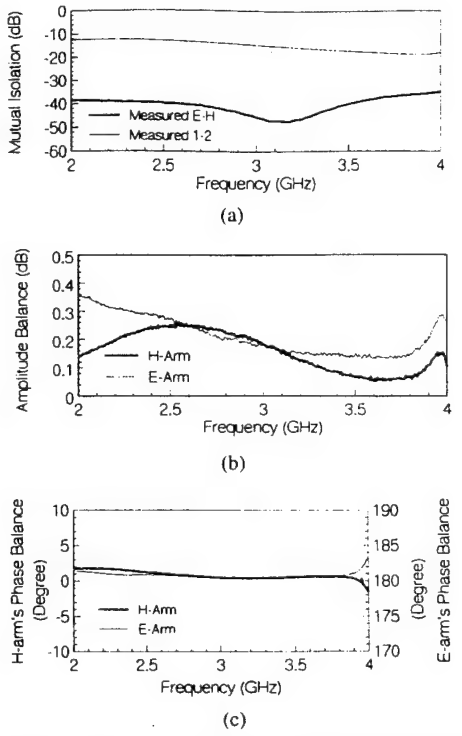

Fig. 18. Measured performance of the magic-T (a) isolation, (b) amplitude balance, and (c) phase balance.

shows the measured and calculated frequency responses of insertion loss for the E arm's power dividing (i.e., out-of-phase mode coupling). The insertion loss is less than 1.1 dB at the center frequency of 3 GHz. As shown in Fig. 17(a) and (b), the calculated results agree well with the measured results except the insertion loss. The additional insertion loss of the CPW magic-T in the measurement is mainly due to the CPW–slotline transition in the reverse-phase tee junction. As shown in Fig. 18, the isolation between the E and H arm is greater than 30 dB from 2 to 4 GHz. The mutual isolation between the two balanced arms is greater than 12 dB in the same frequency range. The H and E arm's maximum amplitude imbalances are 0.3 and 0.4 dB in the frequency range of 2–4 GHz, respectively. The H and E arm's maximum phase imbalance are 2° and 3.5° over the frequency range of 2–4 GHz, respectively.

VI. Conclusion

Simulations of CPW–slotline transitions using transmission line models were presented for the design applications of uniplanar structure. A simple and accurate modeling method for nonuniform CPW and slotline radial stubs using tandem-connected uniform lines have resulted in a very good agreement between simulation and measurement. A uniplanar 180° reverse-phase CPW–slotline balun and tee junction were demonstrated. The phase reversal of both circuits is frequency independent and can be applied to balanced circuits such as magic-T's and balanced mixers. A uniplanar magic-T and a reverse-phase hybrid-ring coupler were developed. The new uniplanar circuits use the combination of CPW's and slotlines on one side of the substrate. The uniplanar magic-T based on the principle of the 180° reverse-phase CPW–slotline tee junction demonstrated a bandwidth of one octave. The hybrid-ring coupler uses CPW–slotline back-to-back baluns to provide a 180° phase change which is independent of frequency. The reverse-phase CPW hybrid-ring coupler shows a fairly good performance over a 60% bandwidth. With the advantages of broad-band operation, simple design procedure, uniplanar structure, and ease of integrating with solid-state devices, these new uniplanar components should have many applications in microwave and millimeter-wave hybrid and monolithic integrated circuits.

References

[1] H. Ogawa and A. Minagawa, "Uniplanar MIC balanced multiplier—a proposed new structure for MIC's," *IEEE Trans. Microwave Theory Tech.*, vol. MTT-35, pp. 1363–1368, Dec. 1987.

[2] M. Abdo Tuko and I. Wolff, "Novel 36 GHz GaAsfrequency doublers using (M)MIC coplanar technology," in *IEEE MTT-S Int. Microwave Symp. Dig.*, June 1992, pp. 1167–1170.

[3] Y. H. Shu, J. A. Navarro, and K. Chang, "Electronically switchable and tunable coplanar waveguide-slotline band-pass filters," *IEEE Trans. Microwave Theory Tech.*, vol. 39, pp. 548–554, Mar. 1991.

[4] C. H. Ho, L. Fan, and K. Chang, "Broad-band uniplanar hybrid-ring coupler," *Electron. Lett.*, vol. 29, pp. 44–45, Jan. 1993.

[5] D. Cahana, "A new coplanar waveguide/slotline double-balanced mixer," in *IEEE MTT-S Int. Microwave Symp. Dig.*, 1989, pp. 967–968.

[6] T. Hirota and H. Ogawa, "Unipolar monolithic frequency doublers," *IEEE Trans. Microwave Theory Tech.*, vol. 37, pp. 1249–1254, Aug. 1989.

[7] W. Grammar and K. Yngvesson, "Coplanar waveguide transitions to slotline: Design and microprobe characterization," *IEEE Trans. Microwave Theory Tech.*, vol. 41, pp. 1653–1658, Sept. 1993.

[8] V. Trifunovic and B. Jokanovic, "New uniplanar balun," *Electron. Lett.*, vol. 27, pp. 813–815, May 1991.

[9] H. Fouad and L. Ramboz, "Broadband planar coplanar waveguide-slotline transition," in *1982 European Microwave Conf. Dig.*, pp. 628–631.

[10] T. Q. Ho and S. M. Hart, "A novel broad band coplanar waveguide to slotline transition," *IEEE Microwave Guided Wave Lett.*, vol. 2, pp. 415–416, Oct. 1992.

[11] C. H. Ho, L. Fan, and K. Chang, "Experimental investigations of CPW-slotline transitions for uniplanar microwave integrated circuits," in *IEEE MTT-S Int. Symp. Dig.*, June 1993, pp. 877–880.
[12] J. W. Duncan and V. P. Minerva, "100:1 bandwidth balun transformer," *Proc. IRE*, vol. 48, pp. 156–164, Jan. 1960.
[13] C. Hede, "High speed logic, Part 3," Tech. Rep. IR 127, Electromagnetics Inst., Technical Univ. Denmark, 1977.
[14] C. Y. Pon, "Hybrid-ring directional couplers for arbitrary power division," *IRE Trans. Microwave Theory Tech.*, vol. MTT-9, pp. 529–535, Nov. 1961.
[15] S. J. Robinson, "Broad-band hybrid junctions," *IRE Trans. Microwave Theory Tech.*, vol. MTT-8, pp. 671–672, Nov. 1960.
[16] S. March, "A wide band stripline hybrid ring," *IEEE Trans. Microwave Theory Tech.*, vol. MTT-16, p. 361, June 1968.
[17] L. W. Chua, "New broad-band matched hybrids for microwave integrated circuits," in *1971 Proc. European Microwave Conf.*, pp. C4/5:1–C4/5:4.
[18] K. Chang, *Handbook of Microwave and Optical Components, Vol. 1*. New York: Wiley, 1990, pp. 153–154.
[19] D. I. Kraker, "Asymmetric coupled-transmission-line magic-T," *IEEE Trans. Microwave Theory Tech.*, vol. MTT-12, pp. 595–597, Nov. 1964.
[20] R. H. DuHamel and M. E. Armstrong, "The tapered-line magic-T," in *Proc. 15th Annu. Symp. Dig. USAF Antenna Res. Program*, Monticello, IL, Oct. 1965, pp. 387–388.
[21] C. P. Tresselt, "Design and computed theoretical performance of three classes of equal-ripple non-uniform line couplers," *IEEE Trans. Microwave Theory Tech.*, vol. MTT-17, pp. 218–230, Apr. 1969.
[22] G. J. Laughlin, "A new impedance-matched wideband balun and magic-T," *IEEE Trans. Microwave Theory Tech.*, vol. MTT-24, pp. 135–141, Mar. 1976.
[23] M. Aikawa and H. Ogawa, "A new MIC magic-T using coupled slot lines," *IEEE Trans. Microwave Theory Tech.*, vol. MTT-28, pp. 523–528, June 1980.
[24] T. Hirota, Y. Tarusawa, and H. Ogawa, "Uniplanar MMIC hybrids—A proposed new MMIC structure," *IEEE Trans. Microwave Theory Tech.*, vol. MTT-35, pp. 576–581, June 1987.
[25] C. H. Ho, L. Fan, and K. Chang, "A broad-band uniplanar slotline hybrid ring coupler with over one octave bandwidth," in *IEEE MTT-S Int. Microwave Symp. Dig.*, June 1993, pp. 585–588.
[26] ——, "Broad-band uniplanar hybrid-ring and branch-line couplers," *IEEE Trans. Microwave Theory Tech.*, vol. 41, pp. 2116–2125, Dec. 1993.
[27] ——, "Slotline annual ring element and their applications to resonator, filter, and coupler design," *IEEE Trans. Microwave Theory Tech.*, vol. 41, pp. 1648–1650, Sept. 1993.

Chien-Hsun Ho, for a photograph and biography, see page 51 of the January issue of this TRANSACTIONS.

Lu Fan, for a photograph and biography, see page 51 of the January issue of this TRANSACTIONS.

Kai Chang (S'75–M'76–SM'85–F'91), for a photograph and biography, see page 51 of the January issue of this TRANSACTIONS.

IEEE TRANSACTIONS ON MICROWAVE THEORY AND TECHNIQUES, VOL. 43, NO. 9, SEPTEMBER 1995

Inverted Stripline Antennas Integrated with Passive and Active Solid-State Devices

Julio A. Navarro, *Member, IEEE*, and Kai Chang, *Fellow, IEEE*

Abstract—**Integrated antennas can reduce the size, weight, and cost of many microwave systems by incorporating component functions directly at the antenna terminals. Their use in many commercial system applications can produce compact, low-cost products. Currently, active integrated antennas are used for distributed oscillators in spatial and quasi-optical power combining. The inverted stripline antenna configuration was developed to easily integrate with solid-state diodes or transistor devices for switching, tuning, modulation, amplification, and oscillating functions. This antenna configuration offers good performance, beam sharpening flexibility, and nondestructive optimization. Good switching, tuning, and oscillating performances have been demonstrated.**

I. Introduction

OVER THE last few years, integrated antennas have received a great deal of attention because they can reduce the size, weight and cost of many transmit and receive systems [1]. Passive and active solid-state devices can be used to combine several component functions at the terminals of the antenna. For example, active devices can be used to design active integrated antenna oscillators, amplifiers and multipliers. These active integrated antennas are ideal for current investigations in spatial and quasi-optical power combining. Integrated antennas pose an interesting problem involving several different areas of microwave engineering such as solid-state devices, circuits, components and antennas. Knowledge of solid-state device characteristics and circuit integration are critical as well as component specifications and antenna performance.

Combining guided-wave circuits with radiating structures often leads to several trade-offs in performance. Material properties which enhance circuit performance often degrade antenna radiation. DC biasing circuits and device packages also disturb antenna characteristics. Similarly, an antenna's radiation may degrade a component's performance. These difficulties need to be overcome so that integrated antennas are able to meet system requirements in military and commercial applications.

Solid-state devices such as two-terminal diodes and three-terminal transistors are small, light-weight and easy to reproduce. These devices are used to develop switching [2], tuning [3]–[5], detecting [6], mixing [7], amplifying [8] and oscillating components. The choice of device depends on the type of microwave component, operating frequency, power output and other considerations. Although transistors offer higher dc-to-RF conversion efficiencies, diodes reach higher operating frequencies and power levels. Diodes normally need higher dc input levels but transistors require more complicated biasing schemes. The choice of solid-state device for an integrated antenna also involves its effect on the radiation characteristics. Although integrated antennas can reduce the size, weight and cost of many microwave systems, active integrated antennas have shown a deterioration of both the antenna and component performance. If an integrated antenna can maintain component specifications with little degradation in the radiation characteristics, the approach would be very attractive for many commercial and military systems.

For the past decade, integrated antennas have mainly focused on active microstrip patches [9]–[16] for radiators in power combining applications. The patch serves as the resonator which compensates for the active device's reactance at the oscillation frequency. The diode position along the antenna determines operating frequency, output power and radiation performance. Analytical models and commercial software packages can calculate resonant frequencies and input impedance along the length of the patch which can be used to find an optimum position for a solid-state device. These models, however, seldom account for device packages, biasing lines and integration discontinuities which disrupt the fields and currents of the antenna. These disturbances often cause changes in operating frequencies, lower conversion efficiencies and higher cross-polarization levels (CPL). Variations in circuit dimensions, dielectric characteristics and diode parameters also introduce errors in the final design. These errors are typically tuned out after assembly in order to consistently meet frequency and power specifications.

The ability to integrate shunt devices easily is of particular importance for active applications. Shunt connections in microstrip requires drilling in MIC's and via hole processing in monolithic MIC's. Some alternative uniplanar geometries have been demonstrated for active and integrated antennas [17]–[22]. Uniplanar transmission lines such as coplanar waveguide, slotline and coplanar strips do not require drilling for shunt connections alleviating the hybrid integration discontinuities encountered in microstrip.

Although not a true uniplanar line, inverted microstrip does not require drilling for shunt connections. This allows nondestructive experimental testing as well as position optimization of diodes and coaxial probe inputs. This trait makes inverted microstrip attractive for hybrid applications. When used for integrated antennas, inverted microstrip provides a

Manuscript received September 12, 1994; revised May 25, 1995. This work was supported in part by NASA-Lewis Research Center in Cleveland, OH, the U. S. Army Research Office, and the Texas Higher Education Coordinating Board's Advanced Technology Program.

The authors are with the Department of Electrical Engineering, Texas A&M University, College Station, TX 77843-3128 USA.

IEEE Log Number 9413420.

built-in radome for protection. By carefully matching the thermal expansion and conductivity coefficients of substrate materials and housing alloys, the integrated antenna can also be hermetically sealed for improved system durability and reliability [23], [24]. DC biasing of devices can be achieved on the substrate or through the ground plane underneath. For increased metal volume and isolation, the antenna is enclosed by a metallic enclosure which can then be classified as trapped inverted microstrip. However, this is a special case of general stripline-type configurations [25].

Gunn-integrated active inverted stripline antennas have been demonstrated in [26], [27] for beam steering and spatial power combiners. These active antennas exhibit good radiation patterns, low cross-polarization levels, easy device integration and good heat sinking capacity. Furthermore, this configuration is useful in passive probe-fed applications as well as integration with FET's and other devices.

In this paper, a cavity model is used to calculate the resonant frequencies of the inverted configuration and compared to measured results. A novel test fixture was devised to nondestructively determine input impedance as a function of probe position. The fixture also allows testing of different antenna dimensions, cavity diameters and substrate dielectric constants and thicknesses. Switchable and tunable probe-fed antennas were demonstrated using PIN's and varactor diodes, respectively. An FET integrated inverted stripline antenna was also developed with excellent oscillation and radiation performance.

II. Design and Test of Passive Antennas

The inverted microstrip configuration removes the ground plane from the substrate backside and inverts the conductor over a ground plane support. The electromagnetic fields are primarily concentrated in the air between the patch and the ground plane providing a lower effective dielectric constant (ε_{eff}), a longer guided wavelength and higher characteristic impedance over a comparable line width in microstrip. Although series or shunt devices are easy to integrate, the inverted configuration is prone to exciting surface wave modes. Surface waves cause considerable cross-talk in densely packed circuits, reduce radiation efficiency and distort antenna patterns. Shorting pins or metallic walls to either side of the conductor can eliminate these unwanted modes. The patch antenna in this configuration can be etched with an arbitrary shape while a circular enclosure is more easily manufactured. In this investigation, circular patch antennas were used to maintain circular symmetry. This structure can be classified as a trapped inverted microstrip which is a subset of the more general stripline-type transmission lines.

Fig. 1 shows the top and side view of the inverted stripline antenna (ISA) configuration. The important dimensions are shown as well as the novel test fixture. These dimensions are used to determine an effective diameter for the patch antenna

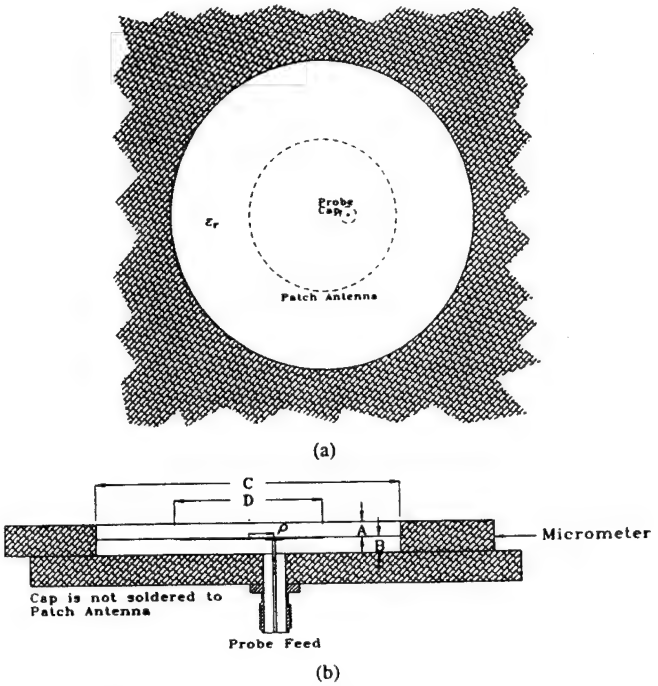

Fig. 1. Configuration of the inverted stripline antenna (ISA) and test fixture (a) top view, (b) side view.

and the corresponding resonant frequency (F_o). Using a conventional cavity model the resonant frequency is calculated using [28]

$$F_o = \frac{\alpha_{mn} c}{\pi D_{\text{eff}} \sqrt{\varepsilon_{\text{eff}}}} \tag{1}$$

where c is the speed of light, α_{mn} is 1.84118 for the dominant mode and D_{eff} is the effective patch diameter due to fringing fields over the radiating edges given by [29] as shown in (2) at the bottom of the page, where D is the physical patch diameter and the height (B) is the patch-to-ground separation. The substrate used is RT-Duroid 5870 with an $\varepsilon_r \approx 2.3$. In this configuration, the majority of the fields are concentrated within the region defined by the patch and the ground plane. Since air fills the region below the patch, the effective dielectric constant (ε_{eff}) is very nearly one. An empirically determined value of 1.1 gives resonant frequency values within 3% of the measured results which range from 3–12 GHz.

As shown in Fig. 1, the dielectric substrates are cut in 62 mm circular inserts. The inserts are press-fitted on a 3 mm deep, ~62 mm cavity enclosure. The inserts are suspended approximately 1.5 mm above the ground plane housing. The ground plane housing has a coaxial probe-feed topped by a 3.5 mm diameter cap which ensures good contact with the antenna and avoids soldering. The probe input was connected to an HP-8510B Network Analyzer and calibrated up to the antenna ground plane. The analyzer tests input impedance match, operating frequency and impedance bandwidth.

This configuration and test fixture allows the enclosure and substrate insert to slide over the probe feed for position

$$D_{\text{eff}} = \frac{D}{2}\sqrt{1 + \left(\frac{4B}{\pi \cdot D \cdot \varepsilon_{\text{eff}}}\right)\left(\ln\left(\frac{D}{4B}\right) + 1.77 + 1.41\varepsilon_{\text{eff}} + \frac{2B}{D}(0.268\varepsilon_{\text{eff}} + 1.65)\right)} \tag{2}$$

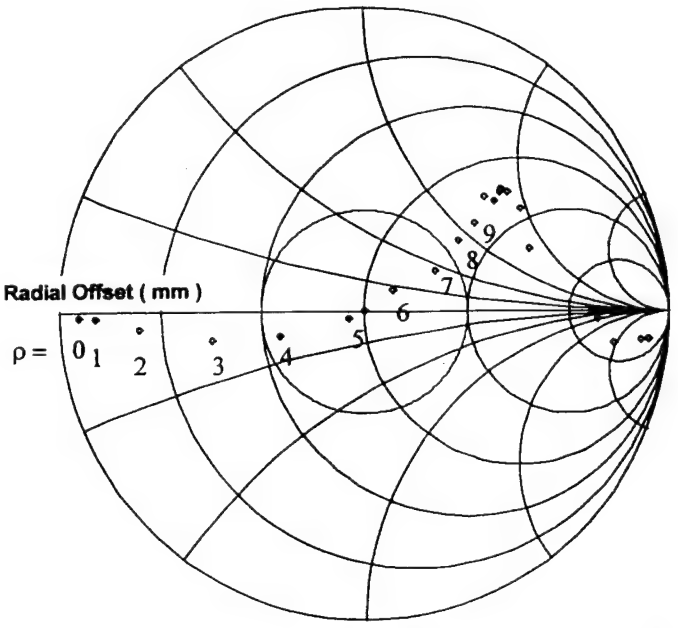

Fig. 2. Input impedance versus radial offset ρ for patch diameters $D = 30$ mm; other parameters are $C = 62$ mm, $A = 1.5$ mm, and $B = 1.5$ mm. The dotted line denotes the 2:1 VSWR circle.

optimization. Accurate probe position is measured with a micrometer. Fig. 2 shows the ISA input impedance of the fundamental mode versus probe position from the center for a 30 mm diameter patch. The best 50 Ω input match for this antenna occurs at 5.21 mm where the VSWR is 1.0003 and the 2:1 bandwidth is 3.77%. As shown, the probe can be positioned over a fairly wide range and it still maintains a 2:1 VSWR. The dominant mode appears as a short circuit at the center of the patch and increases in impedance at the edge of the antenna. Similar results were obtained for other patch diameters.

Different substrate inserts with patch antenna diameters which varied from 10–60 mm were optimized for best 50 Ω match at the operating frequency. Fig. 3 shows measured versus calculated operating frequencies of the ISA structure as a function of patch diameter. The calculations are accurate to within a few percent of the measured results. For the structure dimensions of this investigation, the operating frequencies are primarily determined by the patch size and patch-to-ground separation. These operating frequencies are typically some distance away from the nearest cavity mode which should not pose any problems. Similar results have been reported in [30]. Errors may be due to variations in patch-to-ground separation, probe discontinuities and metallic wall effects on the antenna radiating edges. Also shown in Fig. 3 is the VSWR for each antenna diameter. As the probe moves along the patch, the reflection coefficient (S_{11}) can be optimized for best 50 Ω match. S_{11} levels less than −25 dB were obtained for each antenna. Fig. 4 shows 2:1 impedance bandwidths versus patch diameters. As shown, the 2:1 impedance bandwidth is dependent on the patch to cavity diameter ratio. Large bandwidths are possible using a simple probe-feed without complex matching circuits. The bandwidth increase for smaller patch dimensions is expected since the separation (B) is larger with respect to the wavelength of operation.

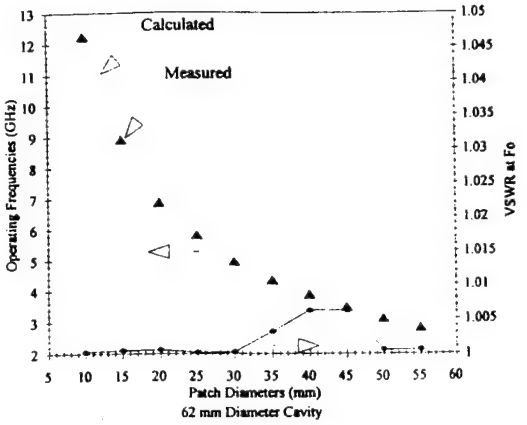

Fig. 3. Operating frequency versus patch diameters.

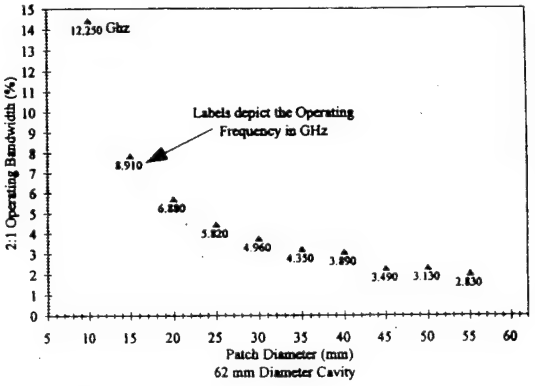

Fig. 4. 2:1 input impedance bandwidth versus patch diameters.

The radiation patterns were tested using an HP automated antenna test system. The radiation patterns for the 30 mm diameter antenna are shown in Fig. 5. The E- and H-plane half-power beamwidths (HPBWs) are 57.5 and 61.5°, respectively. The cross-polarization level is 19.3 dB below the measured gain of 10.5 dBi. Radiation patterns for other patch diameters show that the HPBW varies with the patch-to-cavity diameter ratio. Fig. 6 shows the HPBWs of the E- and H-plane patterns of several antennas, tested in the 62 mm diameter cavity. The inverted substrate and enclosure combination increase the antenna directivity. Noticeable beam sharpening occurs near patch-to-cavity diameter ratios of ≈ 0.5.

As shown in this section, the inverted configuration offers good circuit and antenna performance and it has flexibility in operating bandwidth and radiating beamwidth. Just as the coaxial probe was moved under the antenna, solid-state device positions can also be optimized for best impedance match. The following sections describe integrations with PIN, varactor, Gunn diodes and FET's for hybrid MIC applications.

III. Integrated Antennas with PIN's and Varactors

Two-terminal device integration for this structure is straightforward. Diodes can be connected across the patch to ground. Fig. 7(a) shows integration with two PIN or varactor diodes. From Fig. 7(a), varying the diode position under the patch changes the impedance seen by the diode. Alternatively, the diode position determines the diode's effect on the antenna. Since the electric field is a maximum at the radiating edges

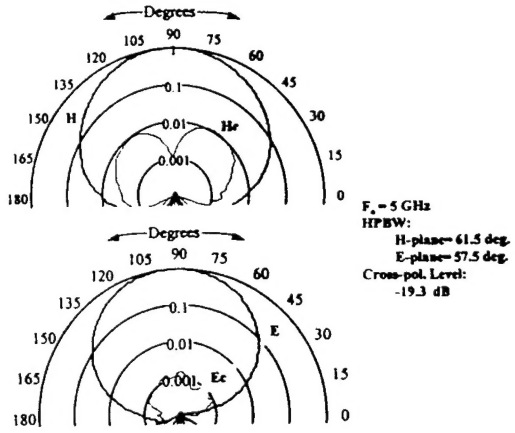

Fig. 5. E- and H-plane radiation patterns for $D = 30$ mm.

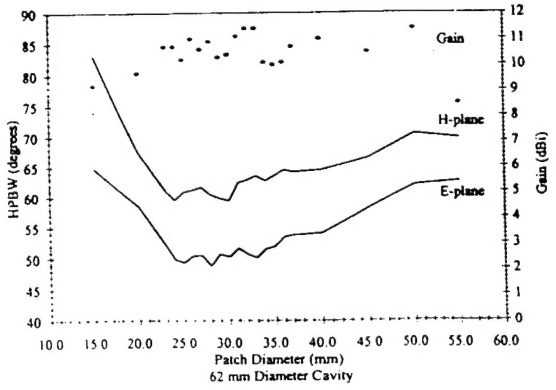

Fig. 6. Measured gain and E- and H-plane HPBW's versus patch diameters.

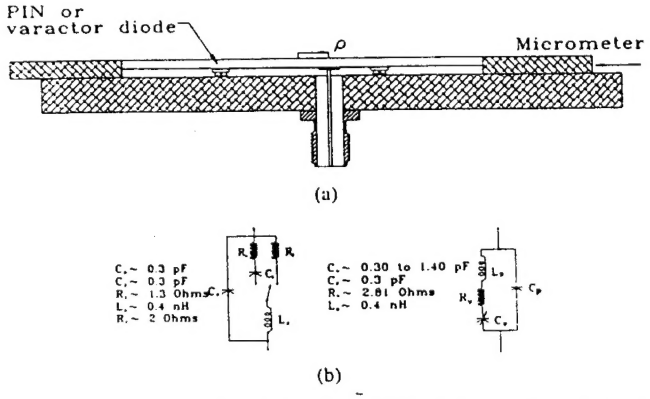

Fig. 7. (a) ISA integrated with PIN or varactor diodes. (b) Equivalent circuit of PIN and varactor diodes.

of the antenna, PIN and varactor diodes will have the most effect at these positions. Equivalent circuits for PIN and varactor diodes are shown in Fig. 7(b). The packaged diodes are soldered to the patch at the radiating edges and the antenna detuning is compensated by slightly adjusting the probe position.

PIN diodes switch electronically between two states which can be used to turn the antenna fundamental mode on and off. At zero bias, the PIN behaves as a load which lowers the antenna operating frequency from 4.96–4.12. Smaller diode packages and positions away from the radiating edges reduce this effect. As the bias is increased from 0–1 Volt, the PIN diodes short circuit the radiating edges of the patch effectively

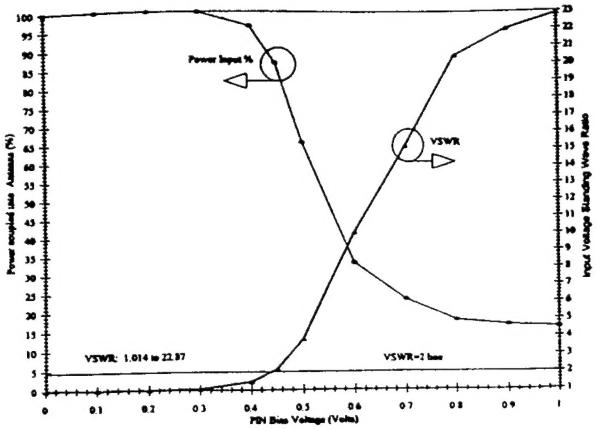

Fig. 8. PIN switching on ISA input VSWR versus bias for $D = 30$ mm.

switching the antenna off. By varying the bias voltage, the antenna reflection coefficient at the operating frequency varies from a VSWR of 1.014–22.87 as shown in Fig. 8. When the diodes are not biased, the VSWR is 1.014. At 1 V (100 mA), the VSWR is 22.87. This effect can be used for switching and amplitude modulation. The power coupling into the antenna is also shown in Fig. 8. The diodes used in this investigation are M/ACOM's general purpose PIN diodes housed in case style #32. The performance would be improved with better diode characteristics and smaller case styles.

If varactors are used instead of PIN diodes, the operating frequency is shifted or tuned with respect to the varactor bias voltage. The M/ACOM varactors used are abrupt junction diodes also housed in case style #32. The varactor capacitance varies as a function of bias voltage (V) according to

$$C(V) = \frac{C(0)}{\left(1 + \frac{V}{V_{bi}}\right)^{\gamma}} \tag{3}$$

where $C(0)$ is the capacitance at 0 Volts, V_{bi} is the built-in potential (GaAs = 1.3 V) and γ is 0.5 for abrupt junctions.

Varactor diodes will have maximum effect on the antenna if they are placed at electric field maxima. At the radiating edges, the varactors couple very strongly with the radiating electric field loading the antenna and lowering the operating frequency. When biased, the varactors can quickly tune over a range of frequencies. Varactor integrated antennas have exhibited a 2:1 VSWR tuning range of over 31% centered at 3.4 GHz. As shown in Fig. 9, at 30 V the operating frequency is at 3.88 GHz with a VSWR of 1.0105. At 0 V the operating frequency is at 2.84 GHz with a VSWR of 1.0053. Fig. 10 shows the ISA 2:1 impedance bandwidth and VSWR versus operating frequency. As shown, the VSWR remains below 1.02 while the impedance bandwidth varies from 1.8–2.5%. This integrated antenna can be used to rapidly scan over its tuning bandwidth for wideband receiver or transmitter applications. The small instantaneous bandwidth (~2%) reduces noise figure in a wideband antenna receiver system.

As in all integrated antennas, there is a degradation in radiation performance due to antenna modifications and device perturbation of the antenna fields. For example, the cross-polarization for the varactor integrated patch is −10 dB compared to −19 dB for the nonintegrated patch. Smaller

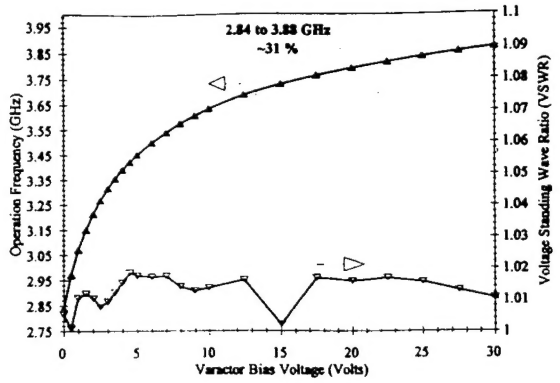

Fig. 9. Varactor tuning on ISA operating frequency versus bias for D = 30 mm.

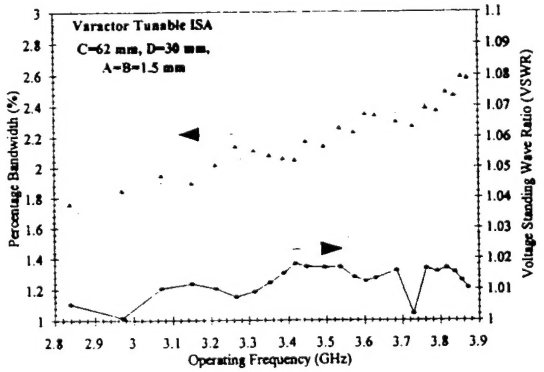

Fig. 10. Varactor tuning on ISA impedance bandwidth and VSWR versus operating frequency.

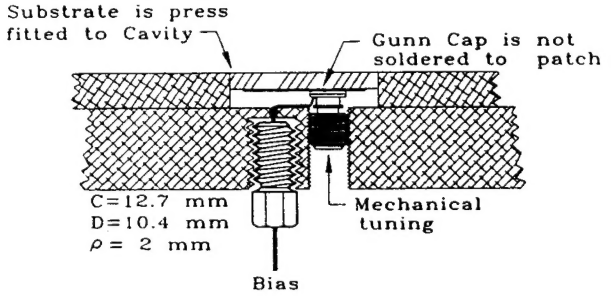

Fig. 11. Gunn integrated ISA in adjustable test fixture.

devices, improved biasing schemes and optimized diode positions will reduce the effect on the radiation pattern.

IV. Active Antennas Using Gunn Devices

Unlike PIN- and varactor-integrated antennas, Gunn integrated antennas generate RF power output. The antenna serves as the resonator as well as the radiator for the oscillator. Oscillations occur at the frequency where the diode and the antenna reactances cancel out. Oscillation startup occurs if the placement of the diode is such that the magnitude of the diode negative resistance is greater than the circuit resistance presented to its terminals. Fig. 11 shows the Gunn integrated ISA in the adjustable test fixture. The package connection to the heat sink and the added metal volume of the metallic walls provide efficient heat sinking for the active device.

M/ACOM 49106-111 diodes were integrated with antennas ranging from 8–11 mm in diameter. The smaller antenna

TABLE I
Gunn Integrated ISA Operating Frequencies, Power Versus Diameter

Patch Diameter (mm)	Measured Fo (GHz)	Oscillator Power* (mW)
8	9.997	63.99
9	9.637	56.76
10	9.438	57.04
10.4	9.240	63.98
11	8.908	66.98

* Calculated using a passive antenna gain of 6.65 dBi. Cavity diameter is 12.7 mm.

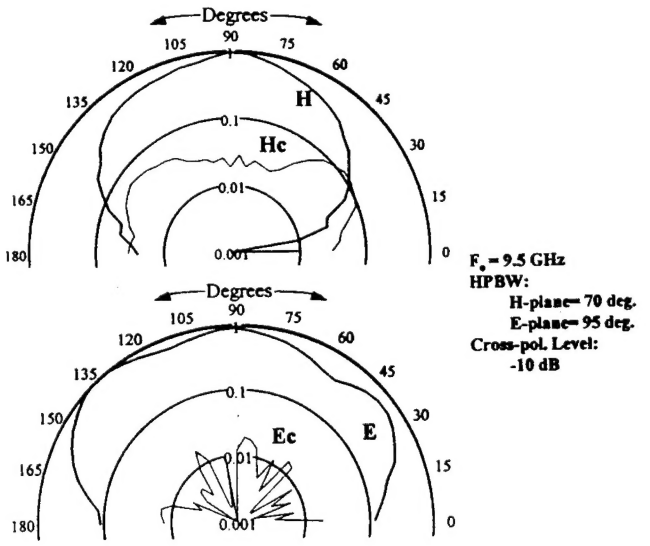

Fig. 12. Gunn integrated ISA radiation patterns.

diameters are used for X-band operation. Since active antennas are mainly intended for use in spatial and quasi-optical power combining, packing density is important. To increase packing density, the metallic walls of the enclosure are very near the edges of the antenna. The diode package as shown in Fig. 11 presents a significant perturbation on the X-band antenna volume which adversely affect the radiation characteristics and disturb the oscillating frequency. The Gunn oscillator frequency and de-embedded power outputs are listed in Table I. The power output is calculated using the Friis transmission equation [12].

Radiation patterns for the Gunn integrated ISA are shown in Fig. 12 [27]. The cross polarization level is at least −10 dB for a Gunn diode 2 mm off-center. The HPBWs are 100 degrees in the E-plane and 70 degrees in the H-plane. A similar antenna using a probe feed exhibited HPBWs of 105 and 80 degrees in the E- and H-plane, respectively with a cross-polarization level of −16 dB. The differences in radiating performance are attributed to the active antennas' diode package and bias lines. Improved performance can be achieved by reducing the size of the device packages. The HPBW's of the X-band ISA's and those of Section II differ because of device and probe perturbation effects and differences in cavity depth and ground plane size with respect to wavelength.

V. Active Antennas with FET's

The use of the FET transistor improves conversion efficiency and noise characteristics while it reduces thermal requirements. However, the antenna must be modified to acco-

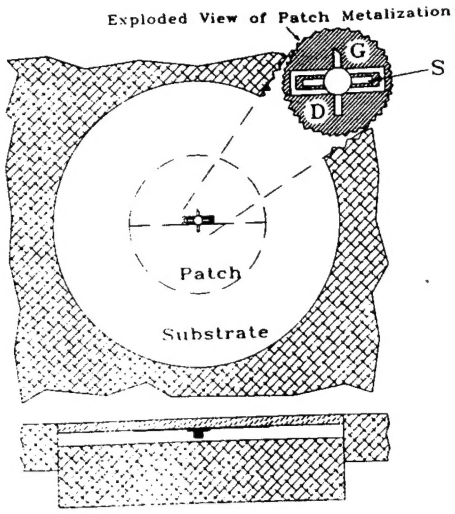

Fig. 13. FET integrated ISA configuration.

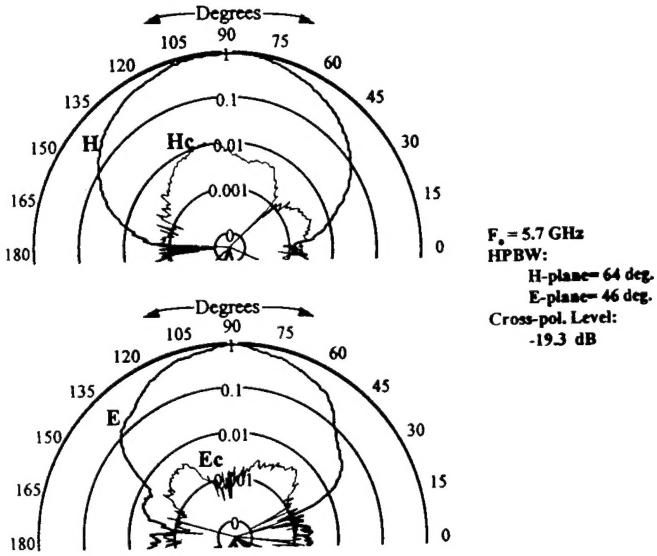

Fig. 14. FET integrated ISA antenna radiation patterns.

modate the FET as shown in Fig. 13. FET integration requires three dc blocks for the drain, gate and source terminals. DC biasing can be achieved from behind the ground plane or etched to the nonradiating edges of the antenna. A chip resistor connected across the source to gate simplifies biasing to the device. The operating frequency is determined by the loads at each transistor port. The transistor can be induced to oscillate at lower frequencies to reduce effects from the device package and bias lines. Lower frequencies of operation can be accomplished with larger patch diameters.

A 30 mm patch was modified to insert the FET (NEC model 76184A). At the center of the patch, 0.4 mm gaps isolate the source from the gate and drain terminals. A 0.1 mm gap is etched from the center to the nonradiating edges of the patch to provide dc isolation between the gate and drain terminals. The FET drain lead is soldered at the center of the patch and the gate lead is approximately 2 mm off-center. Three dc lines bias the source, gate and drain of the transistor. Alternatively, the source bias line can be replaced by a resistor. The frequency of oscillation depends on the impedance loads at the FET ports. The loads are a function of the position along the inverted patch antenna. Heat generated is dissipated by the patch. The lack of a low-impedance path from the device to the metal heat sink may cause thermal problems in higher power devices. This could be alleviated with a shorting pin at the center of the patch to provide a low impedance path to the housing.

Since the antenna was modified and the device terminal are soldered, it is not possible to experimentally optimize the FET position. However, a ground plane sliding short is used to change the antenna cavity depth and alter the oscillation frequency. The cavity depth is used to improve spectral and radiation characteristics of this active antenna.

The FET provides 57 mW at 5.69 GHz when biased at 3.8 V and 26 mA. The 3 dB bias tuning range is approximately 1% for a 1 V change in v_{ds}. The sliding ground plane allows a mechanical tuning range of nearly 6%. At a cavity depth of 4.15 mm, the measured oscillation frequency remains stable at 5.695±0.002 GHz over the antenna test sweep. The HPBW in the E- and H-plane patterns are 46 and 64°, respectively. The cross-polarization level is −19.3 dB below the maximum. Fig. 14 shows principal plane and cross-polarization patterns of the active antenna. The smooth radiation patterns and low cross-polarization level compares favorably with previously reported active antennas [9]–[13], [15]. Probe-fed passive antennas with cavity depths of 3 mm exhibited HPBWs of 51 and 61° in the E- and H-plane patterns, respectively. The cross-polarization level of the passive antenna is also −19.3 dB with a gain of 10.2 dBi. Biasing modifications and cavity depth differences in the active antenna may account for the changes. The effective isotropic radiated power of the active antenna is 594 mW. Approximating the active antenna gain with the passive antenna gain of 10.2 dB results in an oscillator power of 57 mW and a dc-to-RF conversion efficiency of 57%.

VI. Conclusion

A useful passive inverted stripline antenna configuration has been demonstrated. Integration has been demonstrated with PIN and varactor diodes with some degradation of the antenna performance. The integration creates switchable and tunable radiating MIC components. Gunn diodes have also been integrated for active antenna radiators with good output power and a clean spectrum. An FET has shown very good oscillator characteristics as well as exceptional radiation performance. It operates at low voltage and current levels with high conversion efficiency. These active antennas can be used for doppler sensing [31], disposable decoys, wireless communications, phased-arrays [26], [32] and power combining applications. Overall, these integrated and active integrated antennas perform well as compared to current state-of-the-art passive radiators. Further improvement can move these components closer to commercial applications. Combinations of several devices will allow the ability to integrate various component functions.

Acknowledgment

The authors would like to thank the Rogers Corporation for the substrate material which they provided, as well as L. Fan and J. McSpadden for their technical support.

REFERENCES

[1] D. B. Rutledge, D. P. Neikirk, and D. P. Kasilingam, "Integrated circuit antennas," in *Infrared and Millimeter-Waves*, K. J. Button, ed., chap. 1, vol. 10. New York: Academic, 1983, p. 25.

[2] R. B. Waterhouse and N. V. Shuley, "Dual frequency microstrip rectangular patches," *Electron. Lett.*, vol. 28, no. 7, pp. 606–607, Mar. 26, 1992.

[3] P. Bhartia and I. J. Bahl, "Frequency agile microstrip antennas," *Microwave J.*, vol. 25, pp. 67–70, Oct. 1982.

[4] P. M. Haskins, P. S. Hall, and J. S. Dahele, "Active patch antenna element with diode tuning," *Electron. Lett.*, vol. 27, no. 20, pp. 1846–1847, Sept. 26, 1991.

[5] M. P. Purchine, J. T. Aberle, and C. R. Birtcher, "Tunable *L*-band circular microstrip patch antenna," *Microwave J.*, pp. 80–88, Oct. 1993.

[6] S. S. Gearhart, C. C. Ling, and G. M. Rebeiz, "Integrated millimeter-wave corner-cube antennas," *IEEE Trans. Antennas Propagat.*, vol. AP-39, no. 7, pp. 1000–1006, July 1991.

[7] C. M. Jackson, "Patch antenna quasi-optical mixers," *Microwave Opt. Technol. Lett.*, vol. 1, no. 1, pp. 1–4, Mar. 1988.

[8] B. Robert, T. Razban, and A. Papiernik, "Compact amplifier integration in square patch antenna," *Electron. Lett.*, vol. 28, no. 14, pp. 1808–1810, Sept. 10, 1992.

[9] H. J. Thomas, D. L. Fudge, and G. Morris, "Gunn source integrated with a microstrip patch," *Microwaves and RF*, pp. 87–89, Feb. 1985.

[10] T. O. Perkins, "Active microstrip circular patch antenna," *Microwave J.*, pp. 109–117, Mar. 1987.

[11] K. Chang, K. A. Hummer, and G. Gopalakrishnan, "Active radiating element using FET source integrated with microstrip patch antenna," *Electron. Lett.*, vol. 24, no. 21, pp. 1347–1348, Oct. 13, 1988.

[12] K. Chang, K. A. Hummer, and J. Klein, "Experiments on injection locking of active antenna elements for active phased arrays and spatial power combiners," *IEEE Trans. Microwave Theory Tech.*, vol. 37, no. 7, pp. 1078–1084, July 1989.

[13] J. Birkeland and T. Itoh, "FET-based planar circuits for quasi-optical sources and transceivers," *IEEE Trans. Microwave Theory Tech.*, vol. 37, no. 9, pp. 1452–1459, Sept. 1989.

[14] K. D. Stephan and S. Young, "Mode stability of radiation-coupled interinjection-locked oscillators for integrated phased arrays," *IEEE Trans. Microwave Theory Tech.*, vol. 36, no. 5, pp. 921–924, May 1988.

[15] R. A. York and R. C. Compton, "Quasi-optical power combining using mutual synchronized oscillator arrays," *IEEE Trans. Microwave Theory Tech.*, vol. 39, no. 6, pp. 1000–1009, June 1991.

[16] X. D. Wu, K. Leverich, and K. Chang, "Novel FET active patch antenna," *Electron. Lett.*, vol. 28, no. 14, pp. 1853–1854, Sept. 24, 1992.

[17] U. Guttich, "Planar integrated 20 GHz receiver in slotline and coplanar waveguide technique," *Microwave Opt. Technol. Lett.*, vol. 2, no. 11, pp. 404–406, Nov. 1989.

[18] Z. B. Popovic, R. M. Weikle II, M. Kim, K. A. Potter, and D. B. Rutledge, "Bar-grid oscillators," *IEEE Trans. Microwave Theory Tech.*, vol. 38, no. 3, pp. 225–230, Mar. 1990.

[19] J. A. Navarro, Y. Shu, and K. Chang, "Broadband electronically tunable planar active radiating elements and spatial power combiners using notch antennas," *IEEE Trans. Microwave Theory Tech.*, vol. 40, no. 2, pp. 323–328, Feb. 1992.

[20] W. K. Leverich, X. D. Wu, and K. Chang, "New FET active notch antenna," *Electron. Lett.*, vol. 28, no. 24, pp. 2239–2240, Nov. 19, 1992.

[21] X. D. Wu and K. Chang, "Compact wideband integrated active slot antenna amplifier," *Electron. Lett.*, vol. 29, no. 5, pp. 496–497, Mar. 4, 1993.

[22] H. P. Moyer and R. A. York, "Active cavity-backed slot antenna using MESFET's," *IEEE Microwave and Guided Wave Lett*, vol. 3, no. 4, pp. 95–97, Apr. 1993.

[23] S. Sanzgiri and J. Tolleson, "Ka band sub-array technology demonstration program," *Texas Instruments Design Review*, Aug. 7, 1991.

[24] J. A. Navarro, K. Chang, J. Tolleson, S. Sanzgiri, and R. Q. Lee, "A 29.3 GHz cavity enclosed aperture-coupled circular patch antenna for microwave circuit integration," *IEEE Microwave and Guided Wave Lett.*, vol. 1, no. 7, pp. 170–171, July 1991.

[25] M. V. Schneider, B. Glance, and W. F. Bodtmann, "Microwave and millimeter wave hybrid integrated circuits for radio systems," *Bell System Tech. J.*, pp. 1703–1726, July-Aug. 1969.

[26] J. A. Navarro and K. Chang, "Electronic beam steering of active antenna arrays," *Electron. Lett.*, vol. 29, no. 3, Feb. 4, 1993.

[27] J. A. Navarro, L. Fan, and K. Chang, "Active inverted stripline circular patch antennas for spatial power combining," *IEEE Trans. Microwave Theory Tech.*, vol. 41, no. 10, pp. 1856–1863, Oct. 1993.

[28] I. J. Bahl and P. Bhartia, *Microstrip Antennas*. Norwood, MA: Artech House, 1980.

[29] W. C. Chew and J. A. Kong, "Effect of fringing fields on the capacitance of a circular microstrip disk," *IEEE Trans. Microwave Theory Tech.*, vol. MTT-28, no. 2, pp. 98–104, Feb. 1980.

[30] M. Li, K. A. Hummer, and K. Chang, "Theoretical and experimental study of the input impedance of a cylindrical cavity-backed rectangular slot antenna," *IEEE Trans. Antennas Propagat.*, vol. 39, no. 8, pp. 1158–1166, Aug. 1991.

[31] V. F. Fusco, "Self-detection performance of active microstrip antennas," *Electron. Lett.*, vol. 28, no. 14, pp. 1362–1363, July 1992.

[32] R. A. York, "A new phase-shifterless beam-scanning technique using arrays of coupled oscillators," *IEEE Trans. Microwave Theory Tech.*, vol. 41, no. 10, pp. 1810–1815, Oct. 1993.